

MICROCOPY RESOLUTION TEST CHART

AD-A166 101

12

DNA-TR-85-199

IMPROVED MODEL OF ROCK MASS DILATATION

Emmanuel Detournay
Christopher St. John
Agbabian Associates
250 N. Nash Street
El Segundo, CA 90245-4593

29 May 1985

Technical Report

CONTRACT No. DNA 001-84-C-0145

Approved for public release;
distribution is unlimited.

DTIC
ELECTE
APR 10 1985

THIS WORK WAS SPONSORED BY THE DEFENSE NUCLEAR AGENCY
UNDER RDT&E RMSS CODE B344084466 Y99QMXSH00010 H2590D.

Prepared for
Director
DEFENSE NUCLEAR AGENCY
Washington, DC 20305-1000

DTIC FILE COPY

86 3 26 008

Destroy this report when it is no longer needed. Do not return to sender.

PLEASE NOTIFY THE DEFENSE NUCLEAR AGENCY, ATTN: STTI, WASHINGTON, DC 20305-1000, IF YOUR ADDRESS IS INCORRECT, IF YOU WISH IT DELETED FROM THE DISTRIBUTION LIST, OR IF THE ADDRESSEE IS NO LONGER EMPLOYED BY YOUR ORGANIZATION.



UNCLASSIFIED

SECURITY CLASSIFICATION OF THIS PAGE

AD-ALC 6101

Form Approved
OMB No. 0704-0188
Exp. Date: Jun 30, 1986

REPORT DOCUMENTATION PAGE

1a. REPORT SECURITY CLASSIFICATION UNCLASSIFIED		1b. RESTRICTIVE MARKINGS	
2a. SECURITY CLASSIFICATION AUTHORITY N/A since Unclassified		3. DISTRIBUTION / AVAILABILITY OF REPORT Approved for public release; distribution is unlimited.	
2b. DECLASSIFICATION / DOWNGRADING SCHEDULE N/A since Unclassified			
4. PERFORMING ORGANIZATION REPORT NUMBER(S) R-8426-5882		5. MONITORING ORGANIZATION REPORT NUMBER(S) DNA-TR-85-199	
6a. NAME OF PERFORMING ORGANIZATION Agbaban Associates	6b. OFFICE SYMBOL (if applicable)	7a. NAME OF MONITORING ORGANIZATION Director Defense Nuclear Agency	
6c. ADDRESS (City, State, and ZIP Code) 250 N. Nash Street El Segundo, CA 90245-4593		7b. ADDRESS (City, State, and ZIP Code) Washington, DC 20305-1000	
8a. NAME OF FUNDING / SPONSORING ORGANIZATION	8b. OFFICE SYMBOL (if applicable)	9. PROCUREMENT INSTRUMENT IDENTIFICATION NUMBER DNA 001-84-C-0145	
8c. ADDRESS (City, State, and ZIP Code)		10. SOURCE OF FUNDING NUMBERS	
		PROGRAM ELEMENT NO 62715H	PROJECT NO Y99QMXS
		TASK NO H	WORK UNIT ACCESSION NO DH008268
11. TITLE (Include Security Classification) IMPROVED MODEL OF ROCK MASS DILATATION			
12. PERSONAL AUTHOR(S) Detournay, Emmanuel and St. John, Christopher			
13a. TYPE OF REPORT Technical	13b. TIME COVERED FROM 840201 TO 850529	14. DATE OF REPORT (Year, Month, Day) 850529	15. PAGE COUNT 116
16. SUPPLEMENTARY NOTATION This work was sponsored by the Defense Nuclear Agency under RDT&E RMSS Code B344084466 Y99QMXSH00010 H2590D.			
17. COSATI CODES		18. SUBJECT TERMS (Continue on reverse if necessary and identify by block number)	
FIELD	GROUP	SUB-GROUP	
20	11	Rock Dilatancy Nonhydrostatic Loading	
08	13	Elastoplastic Models Laboratory Experiments	
		Hydrostatic Loading Variable Dilatancy.	
19. ABSTRACT (Continue on reverse if necessary and identify by block number) This report documents the results of an investigation aimed at developing analytical models for calculating closure and failure resistance of deep tunnels, based on an improved dilatation model for the rock. The phenomenon of rock dilatancy is first reviewed, and an improved dilatation model - in which the rate of dilatation progressively vanishes with the plastic deformation - is described. The improved dilatation model involves the introduction of a single parameter: the maximum inelastic volume increase that the material can experience. The new dilatation model was then used for the development of two mathematical models of a deep cylindrical tunnel, one for hydrostatic, the other one for nonhydrostatic loading. For the hydrostatic loading, it was shown that closure of the tunnel requires the solution of a nonlinear ordinary differential equation and, for the nonhydrostatic loading, a system of nonlinear partial differential equations of the hyperbolic type is involved. In both cases, the numerical procedures are discussed in detail: Runge-Kutta for the hydrostatic loading, and the method of characteristics for the nonhydrostatic case. Model test experi-			
20. DISTRIBUTION / AVAILABILITY OF ABSTRACT <input type="checkbox"/> UNCLASSIFIED/UNLIMITED <input checked="" type="checkbox"/> SAME AS RPT <input type="checkbox"/> DTIC USERS		21. ABSTRACT SECURITY CLASSIFICATION UNCLASSIFIED	
22a. NAME OF RESPONSIBLE INDIVIDUAL Betty L. Fox		22b. TELEPHONE (include Area Code) (202) 325-7042	22c. OFFICE SYMBOL DNA/STTI

DD FORM 1473, 84 MAR

83 APR edition may be used until exhausted
All other editions are obsoleteSECURITY CLASSIFICATION OF THIS PAGE
UNCLASSIFIED

18. SUBJECT TERMS (Continued)

Constant Dilatancy
Deep Based Tunnels

19. ABSTRACT (Continued)

ments were then reviewed in an attempt to validate the improved dilatation model.

PREFACE

This project was carried out at Agbabian Associates in accordance with Contract No. DNA 001-84-C-0145 for the Defense Nuclear Agency (DNA). Lt. Colonel Gary Gibson was the Contract Technical Manager (CTM) during the initial phase of the research; Dr. Michael J. Shore was the CTM during the conclusion of work. This support is gratefully acknowledged.

Grateful acknowledgements are also extended to the persons who assisted in the preparation of this report: J. Rubottom for typing a particularly difficult manuscript and for overseeing the production of the report, and E. Harding and J. Peters for preparing the figures.

Handwritten checkmark ✓

SEARCHED _____

SERIALIZED _____

INDEXED _____

FILED _____

APR 1984

ATLANTA

Special

AT



**CONVERSION FACTORS FOR U.S. CUSTOMARY
TO METRIC (SI) UNITS OF MEASUREMENT**

MULTIPLY \longrightarrow BY \longrightarrow TO GET
 TO GET \longleftarrow BY \longleftarrow DIVIDE

angstrom	1.000 000 X E -10	meters (m)
atmosphere (normal)	1 013 25 X E +2	kilo pascal (kPa)
bar	1 000 000 X E +2	kilo pascal (kPa)
barn	1 000 000 X E -28	meter ² (m ²)
British thermal unit (thermochemical)	1.054 350 X E +3	joule (J)
calorie (thermochemical)	4 184 000	joule (J)
cal (thermochemical)/cm ²	4.184 000 X E -2	mega joule/m ² (MJ/m ²)
curie	3 700 000 X E +1	*giga becquerel (GBq)
degree (angle)	1 745 329 X E -2	radian (rad)
degree Fahrenheit	$t_{\text{F}} = (t_{\text{C}} + 459.67)/1.8$	degree kelvin (K)
electron volt	1 602 19 X E -19	joule (J)
erg	1.000 000 X E -7	joule (J)
erg/second	1.000 000 X E -7	watt (W)
foot	3.048 000 X E -1	meter (m)
foot-pound-force	1.355 818	joule (J)
gallon (U.S. liquid)	3 785 412 X E -3	meter ³ (m ³)
inch	2.540 000 X E -2	meter (m)
jerk	1 000 000 X E +9	joule (J)
joule/kilogram (J/kg) (radiation dose absorbed)	1.000 000	Gray (Gy)
kilotons	4.183	terajoules
kip (1000 lbf)	4.448 222 X E +3	newton (N)
kip/inch ² (ksi)	6 894 757 X E +3	kilo pascal (kPa)
ktop	1.000 000 X E +2	newton-second/m ² (N-s/m ²)
micron	1 000 000 X E -6	meter (m)
mil	2.540 000 X E -5	meter (m)
mile (international)	1.609 344 X E +3	meter (m)
ounce	2.934 952 X E -2	kilogram (kg)
pound-force (lbs avoirdupois)	4.448 222	newton (N)
pound-force inch	1.129 848 X E -1	newton-meter (N-m)
pound-force/inch	1 751 268 X E +2	newton/meter (N/m)
pound-force/foot ²	4.788 026 X E -2	kilo pascal (kPa)
pound-force/inch ² (psi)	6.894 757	kilo pascal (kPa)
pound-mass (lbm avoirdupois)	4.535 924 X E -1	kilogram (kg)
pound-mass-foot ² (moment of inertia)	4 214 011 X E -2	kilogram-meter ² (kg-m ²)
pound-mass/foot ³	1 601 946 X E +1	kilogram/meter ³ (kg/m ³)
rad (radiation dose absorbed)	1.000 000 X E -2	*Gray (Gy)
roentgen	2.579 760 X E -4	coulomb/kilogram (C/kg)
shake	1 000 000 X E -8	second (s)
slug	1.459 390 X E +1	kilogram (kg)
torr (mm Hg, 0° C)	1.333 22 X E -1	kilo pascal (kPa)

*The becquerel (Bq) is the SI unit of radioactivity; 1 Bq = 1 event/s.
**The Gray (Gy) is the SI unit of absorbed radiation.

TABLE OF CONTENTS

<u>Section</u>	<u>Page</u>
PREFACE	iii
CONVERSION TABLE.	iv
LIST OF ILLUSTRATIONS	vii
LIST OF TABLES.	ix
1 INTRODUCTION.	1
1-1 Scope and Background	1
1-2 Report Organization.	3
2 DILATANCY OF ROCKS.	4
2-1 Causes of Dilatancy.	4
2-2 Critical Review of Laboratory Experiments.	6
2-3 Theoretical Models for Rock Dilatancy.	7
3 ELASTOPLASTIC MODELS OF TUNNELS UNDER HYDROSTATIC AND NONHYDROSTATIC LOADING.	11
3-1 Introduction	11
3-2 Hydrostatic Model.	12
3-2.1 Symmetry Conditions	12
3-2.2 Concept of the Unit-Plane	14
3-2.3 Governing Equations	14
3-3 Nonhydrostatic Model	18
3-3.1 Modes of Failure.	18
3-3.2 Consequences of Statical Determinacy.	20
3-3.3 Governing Equations	21
3-3.4 Validation and Application.	25
4 LABORATORY EXPERIMENTS.	28
4-1 Model Studies.	28
4-2 Isotropic Loading of Low Friction Simulants.	29
4-3 Isotropic Loading of High Friction Simulants.	36
4-4 Biaxial Loading of High Friction Simulants	42
4-5 Effect of Tunnel Reinforcement	45
4-6 Conclusions.	46
5 CONCLUSIONS	51
6 LIST OF REFERENCES.	53

TABLE OF CONTENTS (CONCLUDED)

Appendices

A	ELASTOPLASTIC MODEL OF A DEEP TUNNEL FOR A ROCK WITH VARIABLE DILATANCY	57
B	DISPLACEMENT FIELD IN THE PLASTIC ZONE - CONSTANT DILATANCY ANGLE	69
C	DISPLACEMENT FIELD IN THE PLASTIC ZONE-VARIABLE DILATANCY	89

LIST OF ILLUSTRATIONS

<u>Figure</u>		<u>Page</u>
1	Results of a hypothetical triaxial test on a rock sample.	5
2	Geometrical interpretation of the coefficient of friction μ and the dilatancy factor β	9
3	Variable flow rule, characterized by a maximum inelastic volume change Δ_*	9
4	Hydrostatic model	13
5	Normalized radial displacement of tunnel wall versus radius of plastic zone, for various values of $\tilde{\Delta}_*$ ($K_p = 3, \nu = 0.25$).	16
6	Apparent constant dilatancy factor K^* versus radius of plastic zone, for various $\tilde{\Delta}_*$ values of $\tilde{\Delta}_*$ ($K_p = 3, \nu = 0.25$).	16
7	Nonhydrostatic model.	17
8	Relationship between the initial stress state and failure modes for an unsupported circular tunnel.	19
9	Geometrical interpretation of the tangent (K_p^*) and secant (\bar{K}_p^*) dilatancy factors	23
10	Validation of KINVAR ($m = 0, K_p = 3, \nu = 0.25, \tilde{\Delta}_* = 1$)	26
11	Validation of KINVAR ($m = 0, K_p = 3, \nu = 0.25, \tilde{\Delta}_* = 10$).	26
12	Normalized radial displacement of springline (1) and roof (2) ($m = 0.1, K_p = 3, \nu = 0.25, \tilde{\Delta}_* = 1$).	27
13	Normalized radial displacement of springline (1) and roof (2) ($m = 0.1, K_p = 3, \nu = 0.25, \tilde{\Delta}_* = 10$).	27
14	Tunnel closure versus applied pressure for isotropic loading of SRI RMG 2C2. Liner: 6061-TO aluminum, $a/h = 11.5$	30
15	Tunnel closure versus applied pressure for static isotropic loading of SRI RMG 2C2 - the curves are based on a closed-form solution that neglects out-of-plane plastic strain	32

LIST OF ILLUSTRATIONS (CONTINUED)

<u>Figure</u>		<u>Page</u>
16	Uniaxial stress-strain curve for Al 6061-TO in compression.	33
17	Calculated tunnel closure versus applied pressure curves using closed form solution with constant dilatation angles. SRI rock simulant RMG 2C2 with lined (1015 steel liner, a/h = 18) and unlined tunnel.	34
18	Relationship between radius of plastic region around hole and radius of thick-walled cylinder. Curves are plotted for selected normalized external pressures for material with a friction angle of 2.5°	37
19	Comparison of Hendron theory (curves) with laboratory experiments (points) for symmetric loading	38
20	Relationship between radius of plastic region around hole and radius of thick walled cylinder. Curves are plotted for selected normalized external pressures for material with a friction angle of 33°	40
21	Closure versus support pressure for an external pressure of 10, 15, and 20 ksi.	41
22	Experimental tunnel closure versus applied pressure points for uniaxial strain loading . . .	43
23	Comparison of isotropic loading and biaxial loading under numerical prediction of behavior of tunnel in rock simulant 6B	44
24	Load path for SRI test LSUX-39 on HF5 rock simulant.	47
25	Experimental results from SRI tests LSUX-35 and LSUX-39	48
26	Numerical predictions of closure of reinforced and unreinforced tunnels in rock simulant HF5 . .	49
27	Hydrostatic model	58
28	Unit-plane transformation	58
29	Displacement characteristics.	81

LIST OF ILLUSTRATIONS (CONCLUDED)

30	Method of characteristics	81
31	Contravariant components of displacement.	81
32	Geometrical relation between ρ , $d\rho$, and $d\phi$ for two points infinitesimally close on the same characteristic	94
33	Calculation of displacement by the method of characteristics	94
34	Calculation of average extension between A and B.	94

LIST OF TABLES

Table

1	Critical obliquity m_*	20
---	------------------------------------	----

SECTION 1
INTRODUCTION

1-1 SCOPE AND BACKGROUND.

This report documents the results of an investigation conducted with the objectives of (1) developing an improved analytical model for calculating closure and failure resistance of deep-based tunnels and (2) relating the improved models to results of laboratory studies.

This study is a continuation of "An Investigation of the Failure Resistance of Rockbolted Tunnels for Deep Missile Basing" (AA, 1983). That report described an improved design methodology for minimally hardened tunnels that relies on elastoplastic models of a cylindrical tunnel in an infinite homogeneous rock mass. In these models, the strength of rock is simply defined in terms of a friction angle and a cohesion, and the volumetric expansion of rock during failure in terms of a dilatancy angle (the dilatancy angle controls the rate of increase of the inelastic volume change of the material with the plastic shear strain). With respect to previous methodologies (see Reed et al., 1983, for a state-of-the-art review), three significant improvements were achieved in the course of that investigation:

- Consideration of an arbitrary dilatancy angle with values anywhere between zero (no inelastic dilatation) and the value of the friction angle (the maximum theoretical limit), thus providing a generalization of the models of Newmark (1970) and Hendron and Aiyer (1971) for hydrostatic far-field stress loading.
- Consideration of a deviatoric component in the far-field stress (previous analytical models were restricted to consideration of a hydrostatic far-field loading), with the consequence that the model can predict ovaling of the tunnel during closure.

- Development of design charts based on the semi-analytical nonhydrostatic model. These charts constitute a powerful and quick means of calculating the support pressure to be provided by a support system, to limit closure to within a preset amount.

That investigation concluded that prediction of tunnel closure (and thus of the support pressure) is very sensitive to the assumed (constant) value of the dilatancy angle, and that the dilatation model of rock based on a constant value of the dilatancy angle is inadequate for this class of problems. In practice, the rate of increase of the plastic volume change with the plastic shear strain has not been observed to be constant in rocks; it changes with the amount of plastic deformation approaching zero as the "damage" increases. In contrast, the theoretical models based on the assumption of a constant dilatancy angle predict that there is no upper limit on the maximum inelastic volume increase that the material can experience. The inadequacy of the assumption of a constant dilatancy angle is particularly severe in the tunnel problem, which is characterized by a high distortional strain field in the rock mass.

The principal objective of the present investigation was then to develop an elastoplastic model of a tunnel under either hydrostatic or nonhydrostatic loading, using a more realistic dilatation model for the rock. The improved dilatation model considered in this report assumes an exponential decay of the dilatancy angle, from an initial value equal to the friction angle. It is a simple law that has the advantage of depending on only one physically meaningful parameter; the maximum plastic volume change that the material can experience. Secondary objectives of this investigation consisted of a review of the rock dilatation phenomenon and an analysis of physical model experiments, with the purpose of validating the improved dilatation model.

1-2 REPORT ORGANIZATION.

The main body of this report is comprised of three major sections covering respectively (1) the phenomenon of rock dilatancy, (2) a general description of the elastoplastic models of a tunnel under hydrostatic and nonhydrostatic loading, and (3) an analysis of physical model tests. Mathematical derivation and description of numerical procedures have been documented in three Appendices.

SECTION 2

DILATANCY OF ROCKS

2-1 CAUSES OF DILATANCY.

The phenomenon of volumetric expansion, or dilatancy, has long been observed during shear deformation of densely packed granular media, where it is associated with relative movement of grains and is a geometrical necessity for deformation to occur. Dilatant behavior of rocks during failure was observed first by Bridgman (1949) during compression tests on soapstone and calcite marble. Dilatancy during uniaxial and triaxial compression tests was subsequently confirmed for a large variety of rocks: norite and quartzite (Bieniawski, 1967), granite (Brace et al., 1966; Zoback and Byerlee, 1975), marble, sandstone, limestone, etc. Dilatancy therefore appears to be a pervasive property of many rocks.

A typical result of a triaxial compression test on a dense brittle rock is shown in figure 1a. In the early stage of the test, the volumetric change is negative (i.e., volume decrease); which is mainly attributable to the elastic behavior of the rock but also reflects the closing of some open cracks. At about 50 percent of the peak stress the curve of the volumetric strain versus axial stress starts to deviate from linearity; the deviation becoming progressively greater with increasing stress. Eventually, at fracture, the volumetric curve shows a net volume increase with respect to the original unstressed configuration. In figure 1b, the data have been presented differently, in the form of the variation of the volumetric strain with respect to the axial strain. This curve shows that before the peak stress is reached the accumulated inelastic volume increase (i.e., the difference between total and elastic volume increase) remains relatively small.

The phenomenon of dilatancy in rocks, which finds its cause in several mechanisms of fracturation, is controlled by the mean pressure the initial porosity of the rock. In brittle rock the dilatant behavior observed during compression test is

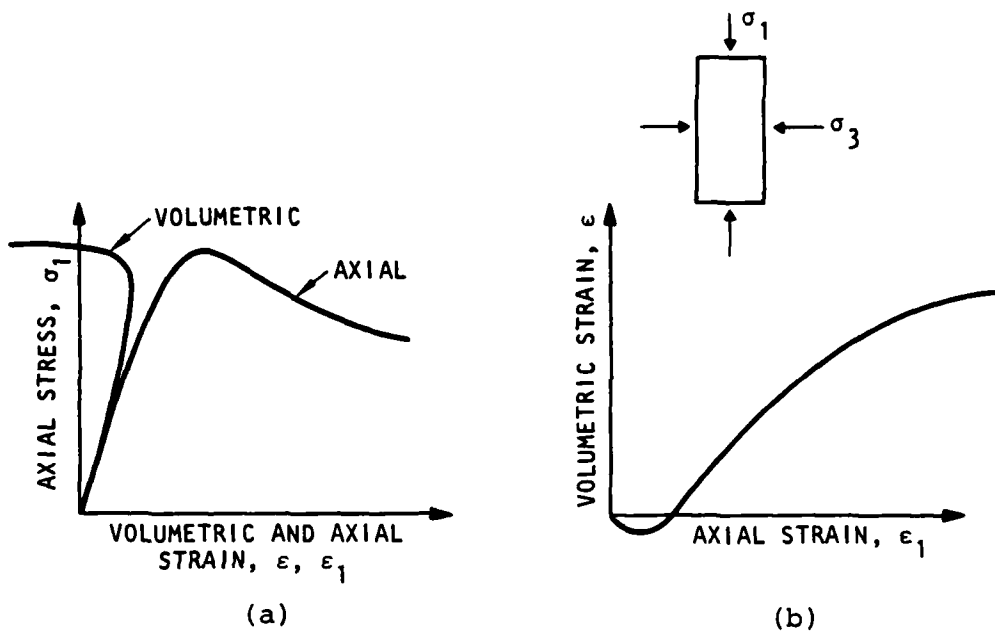


Figure 1. Results of a hypothetical triaxial test on a rock sample.

associated with microcracking and propagation of cracks parallel to the direction of maximum compressive stress (Brace et al., 1966; Cook, 1970). In porous sedimentary rocks dilatancy is not only caused by an increase of the crack space (porosity) but also by sliding along intergranular surfaces (cataclastic flow). At high confining pressure, tendency of dilatancy is suppressed or even reversed (Swanson and Brown, 1972), depending on the initial porosity of the rock, as the high pressure forces intracrystalline flow to occur. For very porous rock, negative dilatancy can even occur at failure, as two processes compete: (1) dilatancy caused by shearing, (2) volume decrease caused by collapse of the pore structure.

Dilatation is thus an all pervasive property of hard rock, and the stress values at which it starts reflect more permanent changes occurring in the rock structure. It has finally to be noted that, although dilatancy is closely associated with the process of macrofracturation, there is no close correlation - as it is sometimes speculated - between suppression of dilatancy and the transition between brittle to ductile failure (Edmond and Paterson, 1972).

2-2 CRITICAL REVIEW OF LABORATORY EXPERIMENTS.

Unfortunately, only a few of the investigations on the dilatancy of rocks can be used in the understanding of the rock response around deep underground excavations. Indeed, many experimental studies of rock dilatation find their motivation in the analysis of earthquake precursors, and are thus concerned with measuring rock dilatancy at very high confining pressures (e.g., Brace et al., 1966; Edmond and Paterson, 1972; Shock et al., 1973). In contrast, modeling the response of rock tunnels requires data on rock dilatancy at relatively low confining pressure (of the orders of tens of bars, as opposed to the thousands of bars which have been reached in high confining pressure experiments). Also rocks around excavations experience a stress path which involves increase of the deviatoric stress accompanying unloading of the mean pressure, while most laboratory experiments are characterized by a concomitant increase of

both the confining pressure and the deviatoric stress. Finally, few data are available beyond peak strength because many experiments were carried out on a "soft" testing machine. (Actually, not only a knowledge of the rock volume change in the post-failure stage is required, but also in test conditions where failure is pervasive throughout the rock sample - the kinematic constraints during triaxial test experiments allows localized failure modes to develop.)

2-3 THEORETICAL MODELS FOR ROCK DILATANCY.

The modern approach for modeling the response of geomaterials is based on the theories of incremental elasto-plasticity which involve the existence of a yield function, f , and a plastic potential, g . The yield function, f , marks the boundary of the elastic state in the stress space; f is not only a function of the stress but also of some measure of the plastic deformation, either the plastic work or the accumulated plastic shear strain. The response to an increment of stress $d\underline{\sigma}$ is elastic if the stress point $\underline{\sigma}$ is inside the current yield surface, or if the current stress point is on the yield surface, and the stress increment is pointing inside the yield surface (elastic unloading). During continued plastic flow, i.e., during a loading history where the stress point remains on the yield surface, the strain increment $d\underline{\epsilon}$ associated with the stress increment $d\underline{\sigma}$ is compounded of an elastic part $d\underline{\epsilon}^e$ (related to $d\underline{\sigma}$ by Hooke's law) and a plastic part $d\underline{\epsilon}^p$ which is proportional to the gradient to the potential surface (flow rule). The condition of continued plastic flow is expressed mathematically by

$$df = 0 \quad (1)$$

while the flow rule is given by

$$d\underline{\epsilon}^p = \lambda \frac{\partial g}{\partial \underline{\sigma}} \quad (2)$$

Like the yield function, f , the plastic potential, g , is a function of the stress and of some measure of past plastic flow.

In this investigation, we are dealing with material models characterized by Mohr-Coulomb yield and potential functions intended to simulate the response of pressure-sensitive dilatant rock materials. The Mohr-Coulomb functions are of the intrinsic curve type; i.e., the plastic deformation is independent of the intermediate principal stress τ_2 . For a Mohr-Coulomb material, the constitutive equations for continuous plastic flow reduce to

$$ds - \mu dP = hdy \quad (3)$$

$$d\Delta = \beta dy \quad (4)$$

where $dP = (d\tau_1 + d\tau_3)/2$, $ds = (d\tau_1 - d\tau_3)/2$, and $d\Delta$ and dy represent, respectively, the variation of plastic volume change $(d\varepsilon_1^P + d\varepsilon_3^P)$ and plastic distortion $(d\varepsilon_1^P - d\varepsilon_3^P)$, and where h represents the hardening modulus. Figure 2 gives the geometrical interpretation of the dilatancy parameter $\beta = \sin \phi^*$ and the friction coefficient $\mu = \sin \phi$. Note that if the $\phi = \phi^*$, the flow rule is associated (ϕ represents the highest theoretical value for the dilatancy angle ϕ^*).

In the previous investigations of elastoplastic models of tunnels (Labreche and Auld, 1980; Reed et al., 1983; AA, 1983) it is assumed that (1) the coefficient of friction is a constant, (2) the material is nonhardening; i.e., $h = 0$, and (3) the dilatancy factor is a constant. These assumptions imply that both yield and potential functions are fixed in the stress space, and that only three parameters are needed to describe the plastic deformation (q , the unconfined compressive strength, the friction angle ϕ , and the dilatancy angle ϕ^*). However, as discussed in the introduction, the weakest of these assumptions is the hypothesis of a constant dilatancy angle, since it results in unbounded inelastic volume changes. In the present investigation, the first two assumptions are maintained while the third assumption is relaxed to a variable condition.

The experimental results reported in the previous section suggest that the dilatancy parameter is both a function

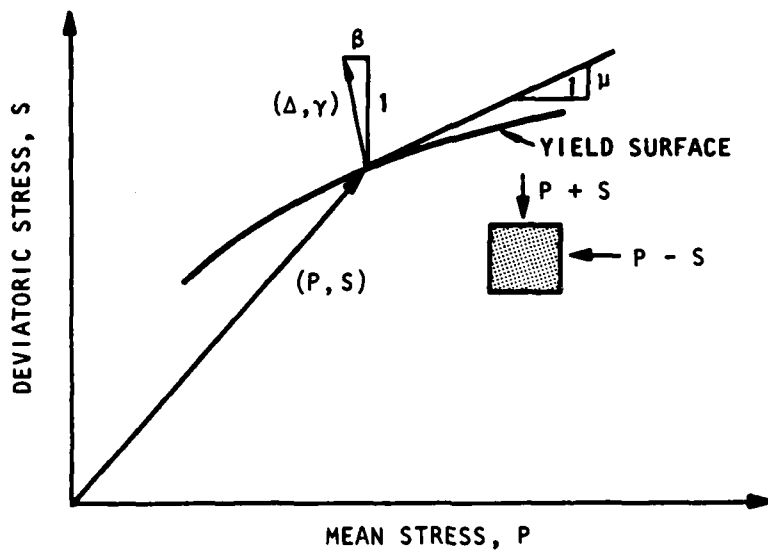
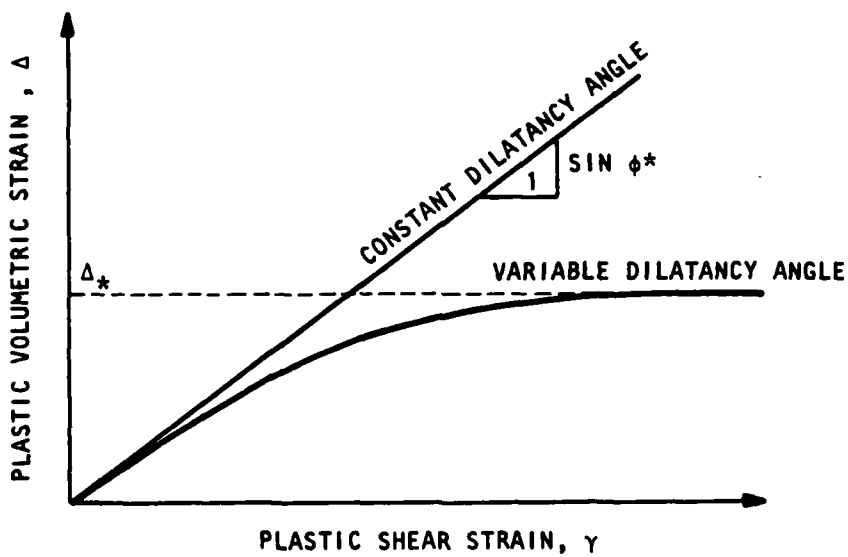


Figure 2. Geometrical interpretation of the coefficient of friction μ and the dilatancy factor β .



AA760

Figure 3. Variable flow rule, characterized by a maximum inelastic volume change Δ_* .

of the accumulated plastic shear strain and the mean pressure. However, since we are interested in the phenomenon of dilatancy at relatively low confining pressure, and in the interest of keeping the model simple, the dependence upon the mean pressure will here be ignored.

The proposed flow rule is based on an exponential decay of the dilatancy factor K_p^* (which is defined as minus the ratio of the maximum to the minimum plastic strain rates, i.e., $K_p^* = - \dot{\epsilon}_1^p / \dot{\epsilon}_3^p$)

$$K_p^* = 1 + (K_p - 1) \exp \left(- \frac{\gamma}{\gamma_*} \right) \quad (5)$$

This law is based on some limited experimental evidence which suggests that (1) the rate of dilatation at peak stress in dense brittle material appears to be consistent with an associated flow rule (Ladanyi and Don, 1970; Gerionopoulos and Brown, 1978), and that (2) the rate of dilatation progressively drops to zero, beyond the peak stress. The parameters γ_* in the exponential law (equation 5) can most usefully be related to the maximum inelastic volume increase Δ_* by integrating the relation

$$\frac{d\Delta}{d\gamma} = \frac{K_p^* - 1}{K_p^* + 1} \quad (6)$$

to yield

$$\Delta_* = \gamma_* \ln \frac{K_p + 1}{2} \quad (7)$$

Section 3 which follows outlines the development of an elasto-plastic model of a deep tunnel which is based on the variable flow rule (equation 5).

SECTION 3

ELASTOPLASTIC MODELS OF TUNNELS UNDER HYDROSTATIC AND NONHYDROSTATIC LOADING

3-1 INTRODUCTION.

In this chapter, the development of two elastoplastic models of a deep cylindrical tunnel, which implement the material model described in Section 2 is outlined. Two models are considered, one for hydrostatic far-field loading, the other one for nonhydrostatic loading. The nonhydrostatic model is restricted to loading conditions for which the problem remains statically determinate; as is always the case for the hydrostatic loading. This restriction ensures that many features of the solution that were derived for a constant dilatancy angle still apply for the improved dilatation model (e.g., the extent and shape of the failed region around the tunnel).

The mathematical foundation of the elastoplastic models is developed for a hydrostatic case in Appendix A and in Appendixes B and C for the nonhydrostatic far-field loading. Appendix B details a formulation for calculating the tunnel closure for the case of a constant dilatancy angle that is developed for solving the general case with variable dilatancy in Appendix C. The formulation discussed in Appendix B is an alternative to that derived previously (Detournay, 1983). It was developed because the original formulation could not be implemented easily with a material characterized by a variable dilatancy.

The equations for calculating the closure of the tunnel are derived for a stress history intended to simulate the excavation unloading of a prestressed rock mass. As discussed in the AA report (1983), an elastic correction has to be applied, to account for a stress history with a far-field stress surcharge.

3-2 HYDROSTATIC MODEL.

3-2.1 Symmetry Conditions.

In the hydrostatic model, the boundary conditions consist of an internal pressure p inside the tunnel and a mean pressure P_0 at infinity (see figure 4). Because of the symmetry of the boundary conditions and the geometry for this problem, the stress, strain, and displacement field in the medium depend only on the radial coordinate r of the cylindrical coordinate system which has its origin at the center of the cavity.

Provided that

$$p < \frac{2}{K_p + 1} \left(P_0 - \frac{q}{K_p - 1} \right) - \frac{q}{K_p - 1} \quad (8)$$

(it is assumed that $P_0 > 2q$), the tunnel is surrounded by a plastic zone of external radius aR_0 . Since the problem is statically determinate, the normalized radius R_0 of the elasto-plastic interface is only a function of p , P_0 , and the yield parameters q and K_p :

$$R_0 = \left[\frac{2}{K_p + 1} \frac{P_0 + \frac{q}{(K_p - 1)}}{p + \frac{q}{(K_p - 1)}} \right]^{1/(K_p - 1)} \quad (9)$$

Since only the loading processes of interest (either internal unloading or external loading) cause a monotonic increase of the radius of the plastic zone, it is advantageous to use R_0 instead of either p or P_0 as a kinematic parameter. In other words, to determine the mechanical fields (stress, strain, and displacement) as a dual function of the coordinate r and the history parameter R_0 .

The problem being statically determinate, the stress field in the medium and the displacement field in the elastic region $r > aR_0$ are actually independent of the flow rule. (Their expressions can, for example, be found in Newmark, 1970, or Hendron and Aiyer, 1971.) To calculate the closure of the tunnel as a function of R_0 , determine the displacement field

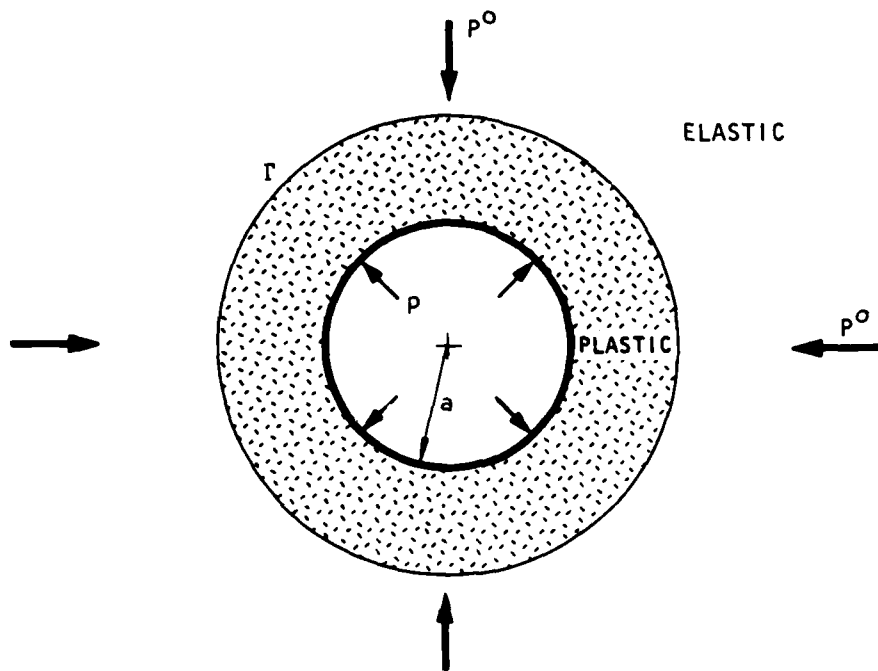


Figure 4. Hydrostatic model.

$u(r, R_0)$ in the plastic zone ($a < r < aR_0$). However, as proven in Appendix A, the general form of the displacement field $u(r, R_0)$ is given by

$$u(r, R_0) = \frac{aR_0 s_\ell^0}{2G} \tilde{u} \left(\frac{r}{aR_0} \right) \quad (10)$$

i.e., the displacement is only a function of the ratio r/aR_0 .

3-2.2 Concept of the Unit-Plane.

Conceptually, it is advantageous to introduce the unit plane transformation $\rho = r/aR_0$. In the unit plane, the circle of radius $\rho = 1$ separates two regions; an interior plastic one from an exterior elastic one. As the plastic annulus grows as a consequence of changes in the boundary conditions, the image of a physical point in the unit plane moves inwards along a radial line, crossing the unit circle when the radius of the plastic boundary reaches that physical point.

The concept of the unit plane is a powerful one, because it substantially simplifies the mathematics of the problem.

3-2.3 Governing Equations.

The normalized displacement $\tilde{u}(\rho)$ ($\rho < 1$) is calculated by solving the differential equation

$$\rho^2 \tilde{u}'' + K_p^* \rho \tilde{u}' - K_p^* \tilde{u} = -\lambda_* \rho^{K_p} \quad (11)$$

with

$$\lambda_* = (K_p - 1)(K_p^* - 1) + (1 - 2\nu)(K_p + 1)(K_p^* + 1)$$

subject to the boundary conditions

$$\tilde{u}(1) = -1 ; \tilde{u}'(1) = 1 \quad (12)$$

The dilatancy factor K_p^* is a function of the maximum plastic shear distortion γ , which can be expressed in terms of ρ , \tilde{u} , and \tilde{u}' :

$$\gamma = \frac{S_{\ell}^0}{2G} \left(\tilde{u}'(\rho) - \frac{\tilde{u}(\rho)}{\rho} - 2\rho^{K_p-1} \right) \quad (13)$$

The differential equation can thus be cast in the general form

$$\tilde{u}'' = F(\rho, \tilde{u}, \tilde{u}') \quad (14)$$

which is well suited for numerical solution, using an algorithm such as Runge-Kutta. (Such an algorithm is usually included in the math library of a scientific calculator, thus making the solution of equation 14 straightforward.)

The function $\tilde{u}(\rho)$ depends only on three dimensionless parameters: K_p , ν , and $\tilde{\Delta}_*$, which is defined as

$$\tilde{\Delta}_* = \frac{2G}{S_{\ell}^0} \Delta_* \quad (15)$$

Experimental evidence suggests that the maximum inelastic volume increase Δ_* is generally less than 5 percent, thus leading to a possible range of values for Δ_* between 0 and 100.

Once the function $\tilde{u}(\rho)$ has been determined, the displacement at the tunnel wall, as a function of the history parameter R_0 , is simply given by

$$u = \frac{aR_0 S_{\ell}^0}{2G} \tilde{u} \left(\frac{1}{R_0} \right) \quad (16)$$

The variation of the normalized displacement $(2G/aS_{\ell}^0) u$ at the boundary has been plotted in figure 5 as a function of the normalized radius of the plastic zone for $K_p = 3$, $\nu = 0.25$, and various values of the parameter $\tilde{\Delta}_*$. To illustrate how the use of a constant dilatancy angle can be misleading, figure 6 presents the apparent constant dilatancy factor K_p^* which yields, for any given value of R_0 , the same displacement at the boundary as obtained with the variable flow rule (equation 5). Figure 7 suggests that the solution for $\tilde{\Delta}_* = 0.1$ should approximate closely the solution for a plastically incompressible material ($K_p^* = 1$) for values of R_0 greater than 1.5; while the displacement for $\tilde{\Delta}_* = 100$ should be close to the one predicted by an

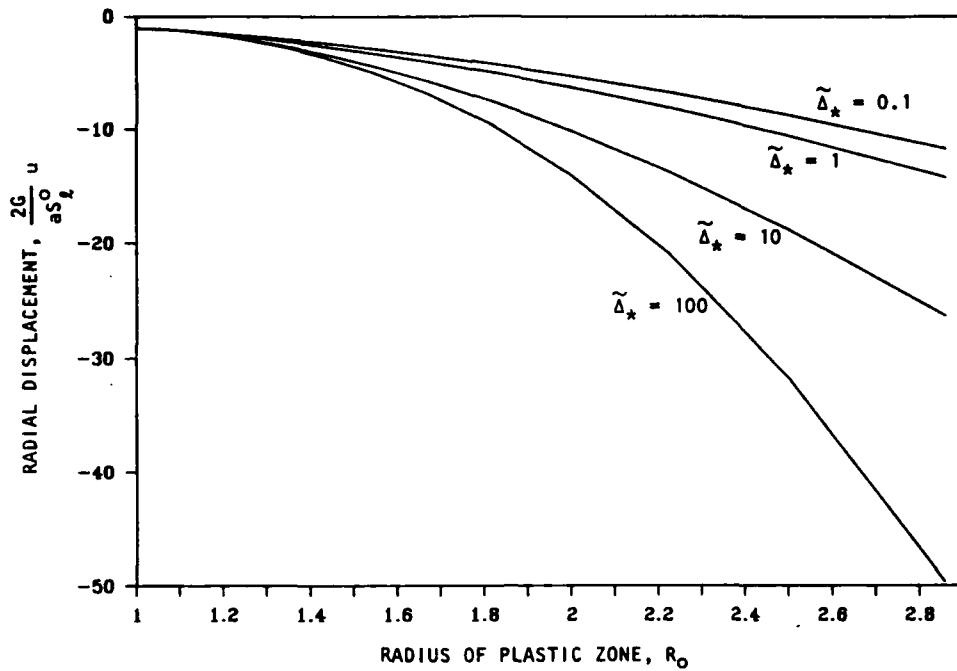


Figure 5. Normalized radial displacement of tunnel wall versus radius of plastic zone, for various values of $\tilde{\Delta}_*$ ($K_p = 3$, $\nu = 0.25$).

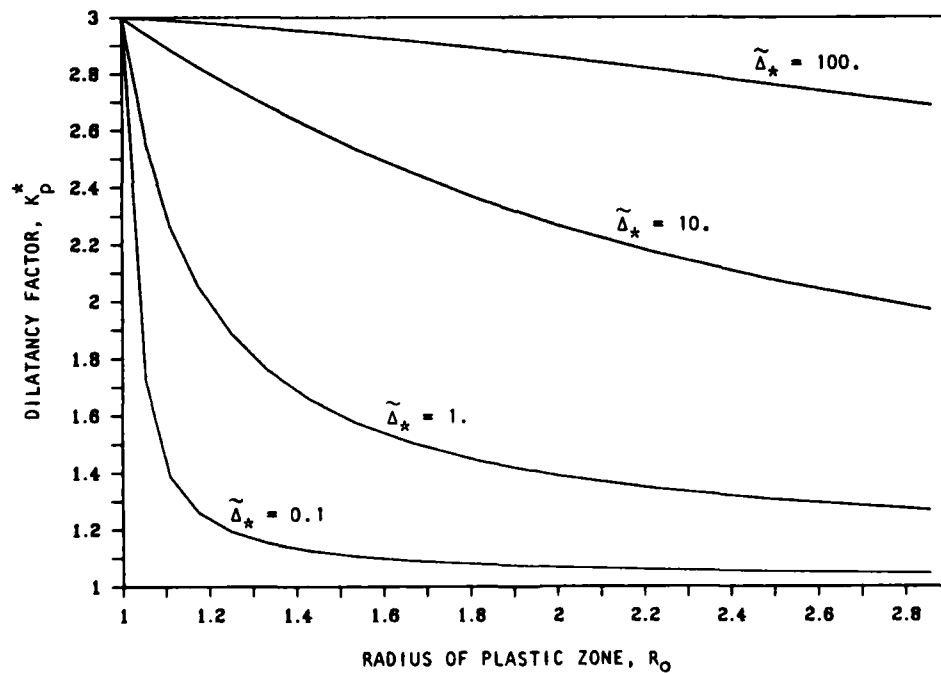


Figure 6. Apparent constant dilatancy factor K_p^* versus radius of plastic zone, for various values of $\tilde{\Delta}_*$ ($K_p = 3$, $\nu = 0.25$).

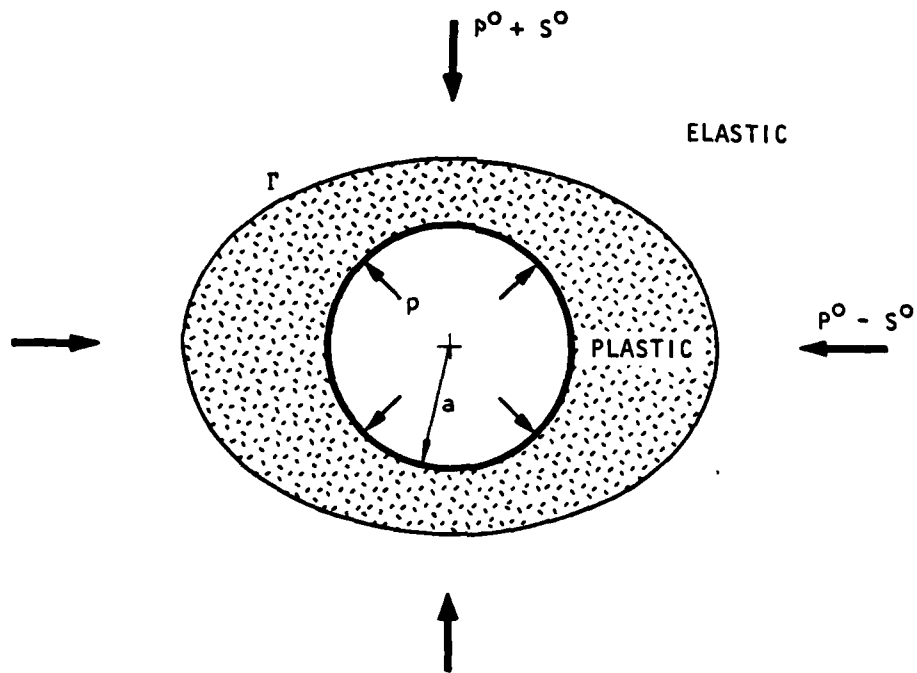


Figure 7. Nonhydrostatic model.

associated flow rule ($K_p^* = 3$) for R_0 less than 2.5. The numerical analysis indicates that the plastic dilatation on the boundary rapidly reaches its maximum value in the first case ($\tilde{\Delta} \cong 0.1$ for $R_0 = 1.1$; $\tilde{\Delta}_* = 0.1$), but that only 45 percent of the maximum inelastic dilatation has been reached for $R_0 = 2.5$ in the second case ($\tilde{\Delta}_* = 100$).

3-3 NONHYDROSTATIC MODEL.

3-3.1 Modes of Failure.

In this model the stress at infinity is characterized by a mean pressure P^0 and a stress deviatoric S^0 (see figure 7). In this case, the problem is characterized by two axes of symmetry, which are parallel to the principal stress directions at infinity. Due to the existence of a stress deviatoric S^0 at infinity, different modes of failures can develop around the tunnel depending on the relative values of P^0 , S^0 , p , and q . Consider first the case of an unsupported tunnel ($p = 0$). The different types of behaviors can graphically be depicted in the normalized stress space (P^0/q , S^0/q) (see figure 8):

- Type 1: Elastic behavior only (region designated I)
- Type 2: Limited failure in a direction perpendicular to the major in-situ stress (region designated IIa)
- Type 3: Tunnel completely surrounded by an oval-shaped yield zone (region designated IIb)
- Type 4: A "butterfly"-shaped plastic region around the tunnel (region designated III)

Region II in the stress diagram corresponds to statically determinate cases; i.e., conditions for which the extent and shape of the plastic region are entirely controlled by the stress boundary conditions and the yield parameters q and K_p . The boundary between statically determinate and indeterminate conditions corresponds to a line of critical obliquity m^* (recall

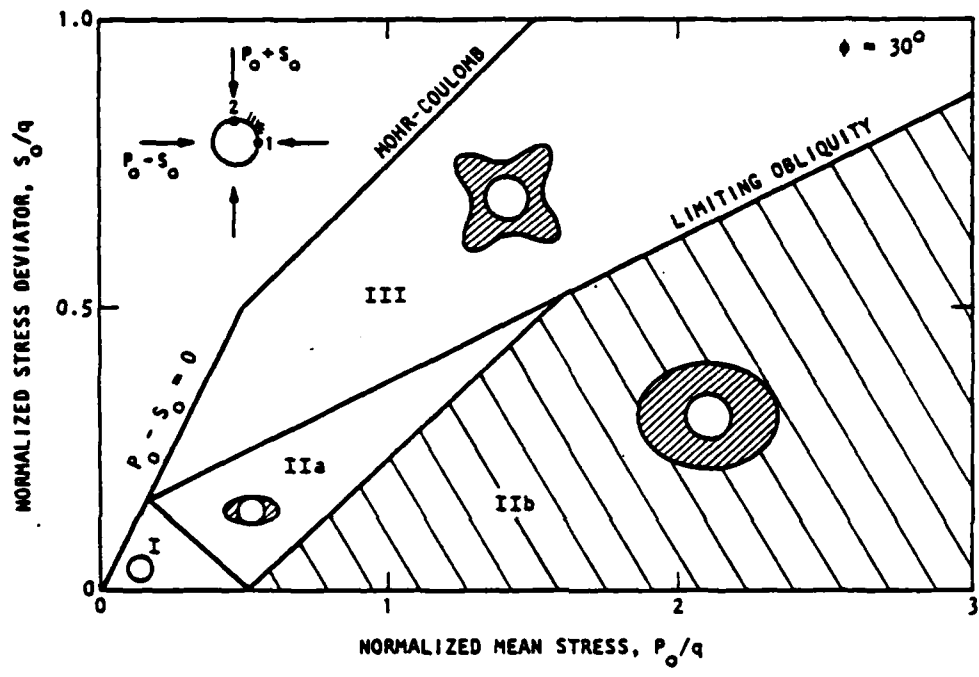


Figure 8. Relationship between the initial stress state and failure modes for an unsupported circular tunnel.

that the obliquity is defined as the ratio of s^0/s_p^0). The critical obliquity m^* is only a function of the friction angle ϕ (see table 1). Far-field stress points on a line of equal obliquity correspond to elastoplastic interfaces that are geometrically identical, but of different sizes.

TABLE 1. Critical obliquity m^* .

ϕ	0°	10°	20°	30°	40°
m_*	0.414	0.437	0.466	0.500	0.542

The existence of an internal support pressure in the tunnel causes the boundary between regions I and IIa and the boundary between regions IIa and IIb to move to the left. As discussed in AA (1983), the effect of an internal support pressure can be taken into account by a simple geometrical construction, which involves moving the far-field stress point along a line of equal obliquity. Accordingly, the presence of an internal pressure changes neither the boundary between statically determinate and indeterminate conditions, nor does it change the shape of the elastoplastic interface.

3-3.2 Consequences of Statical Determinacy.

The semianalytical solution developed in this report is restricted to far-field conditions for which the problem is statically determinate; i.e., for obliquity less than the critical obliquity m^* . The restriction to statically determinate conditions ensures that, similarly to the hydrostatic loading, the location of the elastoplastic boundary is solely controlled by the stress boundary conditions P^0 , s^0 , and p , and the yield parameters q and K_p . For conditions for which the tunnel is completely engulfed by a plastic zone, the interface is characterized by a major to minor axis ratio equal to

$$\frac{\text{major axis}}{\text{minor axis}} = \left(\frac{1 + m}{1 - m} \right)^{2/(K_p + 1)} \quad (17)$$

with the obliquity m defined as

$$m = \frac{S^o}{S_l^o} \quad (18)$$

The average radius of the plastic zone corresponds, however, to the one computed for hydrostatic loading. Also, the stress field in the medium and the displacement field in the elastic region are the same as the one computed for a constant dilatancy angle. To calculate closure of the tunnel, we need to calculate the displacement in the plastic region as a function of the boundary conditions, or equivalently as a function of the average radius of the plastic zone (as for the case of hydrostatic loading). In this case, however, the displacement has not only a radial component but also a tangential one (except on the axes of symmetry), and is a function of both cylindrical coordinates (r, θ) and of the kinematic parameter R_o .

3-3.3 Governing equations.

Derivation of the equations governing the displacement in the plastic region of a material with a variable dilatancy follows closely the approach adopted for a constant dilatancy (see Appendixes B and C). The derivation is based on the property exhibited by the stress solution that there is no rotation of the principal stress directions in the plastic zone during propagation of the failure zones around the tunnel. This property of the solution ensures that the principal directions of the incremental plastic strain tensor $d\varepsilon^p$ remains locked in the radial and tangential directions everywhere in the plastic zone and at any time during the monotonic loading. This feature of the problem allows integration of the flow rule

$$\frac{d\varepsilon_r^p}{d\varepsilon_\theta^p} = - K_p^* \quad (19)$$

thus yielding the following relation between the radial and tangential plastic strain components ε_r^P and ε_θ^P .

$$\varepsilon_r^P = -\bar{K}_p^*(\gamma) \varepsilon_\theta^P \quad (20)$$

with

$$\gamma = \varepsilon_r^P - \varepsilon_\theta^P$$

The symbol \bar{K}_p^* stands for the secant dilatancy factor, which, on the basis of equation (5), is given by

$$\bar{K}_p^* = \frac{1 + \alpha}{1 - \alpha}; \quad \alpha = \frac{\gamma^*}{\gamma} \ln \frac{K_p + 1}{2 + (K_p - 1)e^{-\gamma/\gamma^*}}; \quad (21)$$

with

$$\gamma^* = \frac{\Delta_*}{\ln \frac{K_p + 1}{2}}$$

Figure 9 illustrates the geometrical interpretation of the tangent and secant dilatancy factor (note that for a constant dilatancy, the distinction between tangent and secant dilatancy factor disappears).

The governing equations of the displacement in the plastic region are deduced from equation (20) as follows: the plastic strain is expressed as the difference between the total and the elastic strain; the elastic strain field in the plastic zone is explicitly determined, using Hooke's law and the stress solution; and, the total strain can be related to the partial spatial derivatives of the displacement. These relationships result in a set of partial differential equations for the displacement that are solved using the elastic displacement on the elastoplastic interface as boundary conditions. It turns out, that as for the hydrostatic case, the general form of the displacement is given by

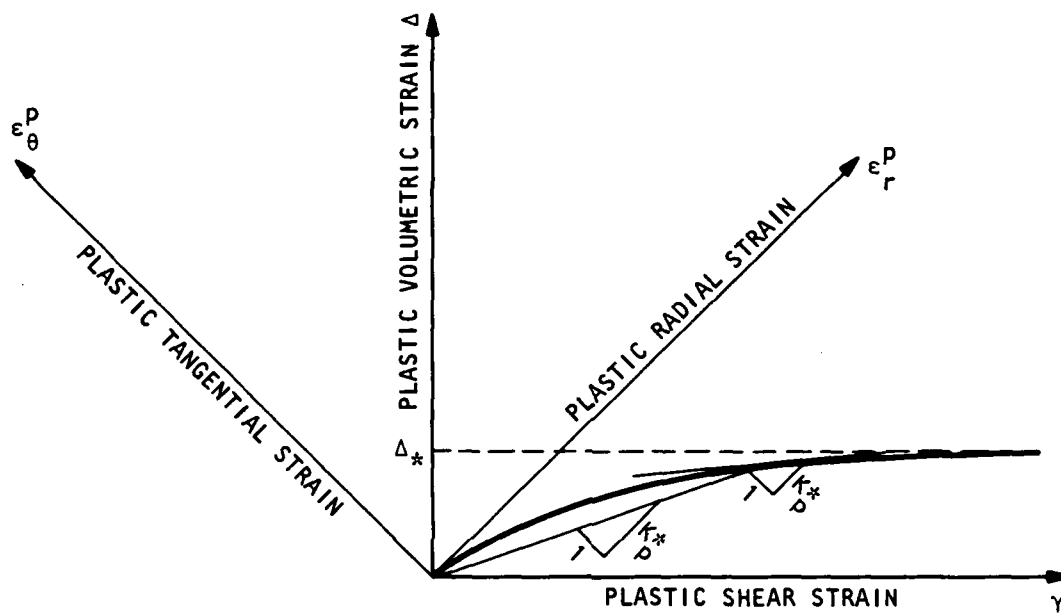


Figure 9. Geometrical interpretation of the tangent (K_p^*) and secant (\bar{K}_p^*) dilatancy factors.

$$\underline{u}(r, \theta; R_0) = \frac{aR_0 S_0^0}{2G} \tilde{u} \left(\frac{r}{aR_0}, \theta \right) \quad (22)$$

The displacement field is thus a unique function of the coordinates of the unit-plane.

All calculations done, the partial differential equations governing the normalized displacement in the plastic zone are given by

$$\begin{aligned} \left(\frac{\partial \tilde{u}_x}{\partial x'} + \frac{\partial \tilde{u}_y}{\partial y'} \right) \cos 2\phi - \left(\frac{\partial \tilde{u}_x}{\partial x'} - \frac{\partial \tilde{u}_y}{\partial y'} \right) \sin 2\phi &= H_1(\rho, \phi) \\ \left(\frac{\partial \tilde{u}_y}{\partial y'} + \frac{\partial \tilde{u}_x}{\partial x'} \right) \cos 2\phi - \left(\frac{\partial \tilde{u}_x}{\partial x'} - \frac{\partial \tilde{u}_y}{\partial y'} \right) \sin 2\phi &= H_2(\rho, \phi) \end{aligned} \quad (23)$$

where

$$\begin{aligned} H_1(\rho, \phi) &= - \frac{2\bar{\lambda}_*}{(K_p - 1)(\bar{K}_p^* + 1)} \rho^{K_p - 1} \cos 2\phi \\ &\quad + 2(1-2\nu) \frac{K_p + 1}{K_p - 1} \cos 2\phi + 2m \frac{\bar{K}_p^* - 1}{\bar{K}_p^* + 1} \\ H_2(\rho, \phi) &= 2m \sin 2\phi \end{aligned} \quad (24)$$

with

$$\bar{\lambda}_* = (K_p - 1)(\bar{K}_p^* - 1) + (1 - 2\nu)(K_p + 1)(\bar{K}_p^* + 1) \quad (25)$$

This nonlinear system of equations is of the hyperbolic type, and can thus be solved by the method of characteristics. This system is however very stiff and as a result, poor accuracy is achieved if standard algorithms of solution are used. Because of the ill-conditioned nature of equation (23), a special scheme had to be used. This involved transforming the equations into a system of two ordinary differential equations along the characteristics and solving them using a central node finite difference technique.

3-3.4 Validation and Application.

As a means of validating the numerical algorithm (program KINVAR) developed to calculate the closure of a tunnel in the presence of a nonhydrostatic far-field stress, two hydrostatic test cases were run and compared with results obtained by the code GROUND, which solves the differential equation with the Runge-Kutta algorithm. The comparison is shown in figures 10 and 11, where the normalized radial displacement at the tunnel wall is plotted as a function of the radius R_0 of the elasto-plastic interface. These figures indicate that with relatively few points, (which is indicative of a relatively coarse characteristic mesh), KINVAR is able to faithfully predict the closure of the tunnel.

Two nonhydrostatic cases have also been solved, and the results shown in figures 12 and 13 (radial displacement on the two axes of symmetry as a function of R_0). These plots confirm that the tunnel ovals during closure, with the direction of maximum closure becoming perpendicular to the maximum compressive far-field stress, once the plastic region around the tunnel becomes sufficiently large.

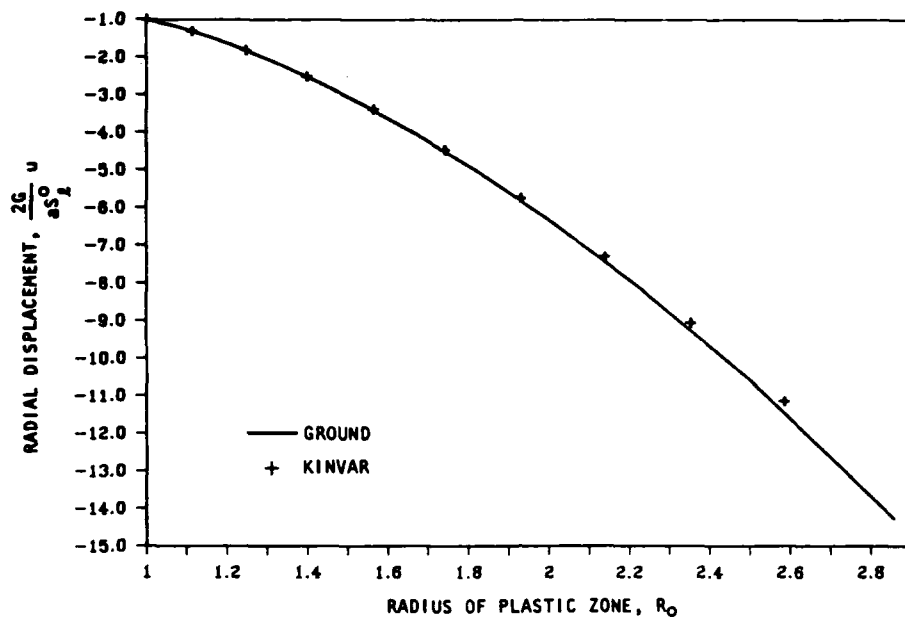


Figure 10. Validation of KINVAR ($m = 0$, $K_p = 3$, $\nu = 0.25$, $\tilde{\Delta}_* = 1$).

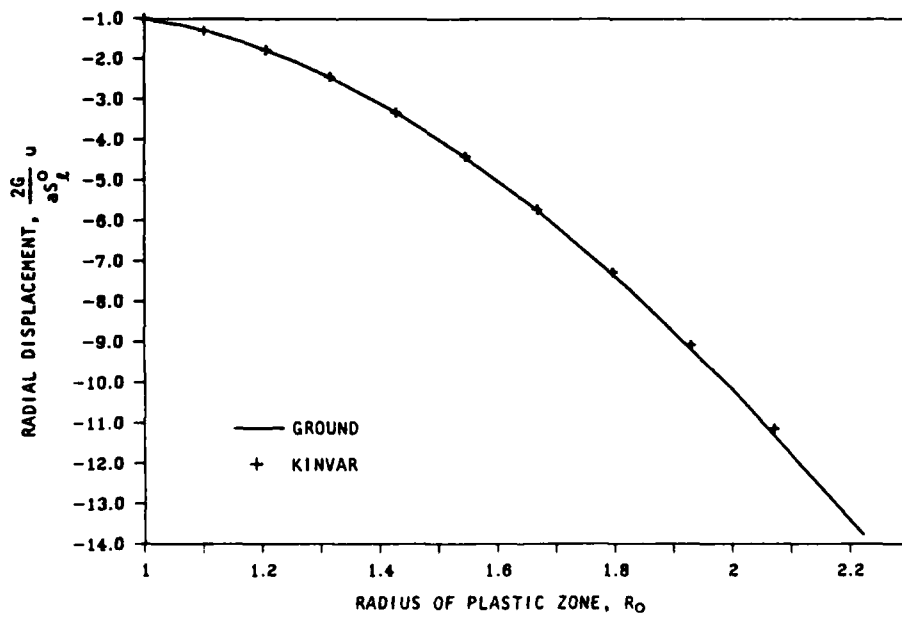


Figure 11. Validation of KINVAR ($m = 0$, $K_p = 3$, $\nu = 0.25$, $\tilde{\Delta}_* = 10$).

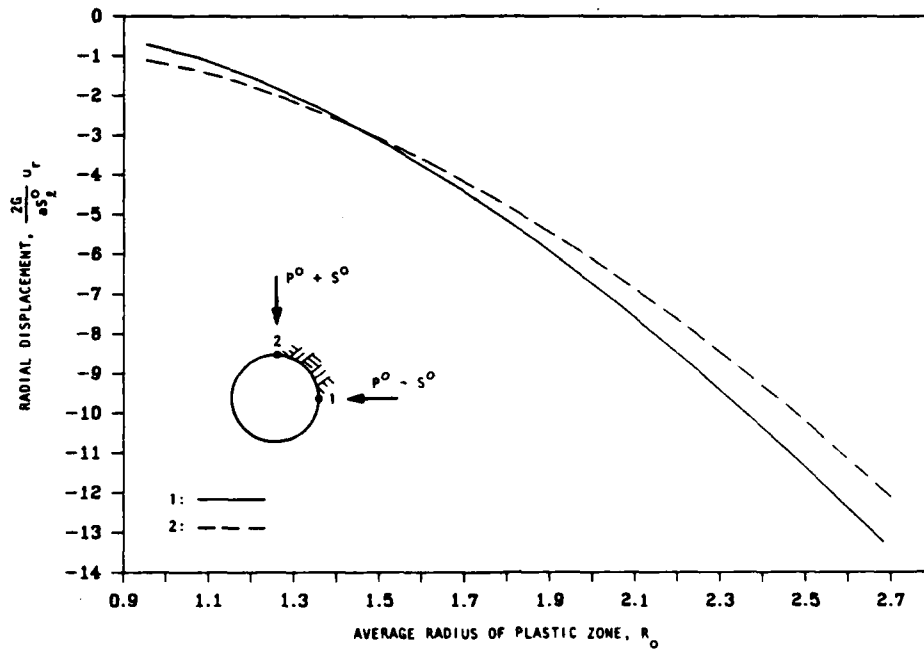


Figure 12. Normalized radial displacement of springline (1) and roof (2) ($m = 0.1$, $K_p = 3$, $\nu = 0.25$, $\tilde{\Delta}_* = 1$).

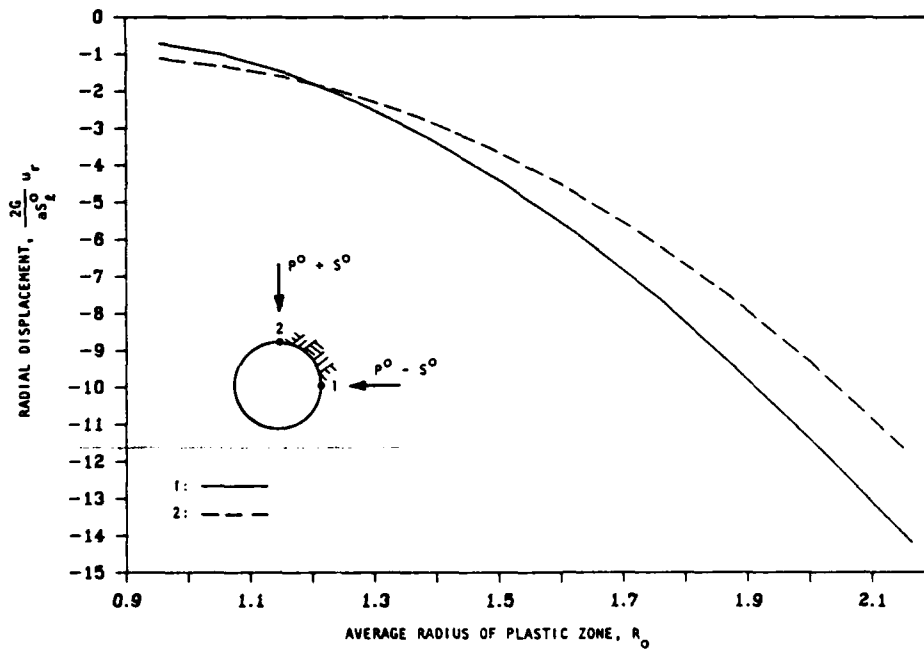


Figure 13. Normalized radial displacement of springline (1) and roof (2) ($m = 0.1$, $K_p = 3$, $\nu = 0.25$, $\tilde{\Delta}_* = 10$).

SECTION 4

LABORATORY EXPERIMENTS

4-1 MODEL STUDIES.

Over the past 15 years or more the Department of Defense, through several agencies and contractors, has conducted a large number of scaled model studies of underground excavations, mostly in rock simulant. The studies have investigated a number of significant parameters governing the behavior of hardened excavations, including: alternative ground support systems, monotonic loading, and static versus dynamic loading. The tests have undoubtedly contributed significantly to the understanding of the behavior of underground excavations and the results of the scaled model tests have been demonstrated to be qualitatively similar to those observed during testing of full-scale structures in the vicinity of underground weapons tests.

The most extensive series of tests have been performed by the Stanford Research Institute (SRI), using cylindrical specimens 4 in. and 12 in. in diameter into which excavations have been drilled or cast. Emphasis during the earlier tests was on simulating the behavior of excavations in tuff, and a number of rock simulants with relatively low friction angles were used to fabricate lined and unlined tunnels in intact and jointed rock. Emphasis was also placed on understanding the impact of static versus dynamic loading. More recently the interest in siting a deep based missile system in a sedimentary stratigraphy has resulted in testing of a number of different types of structures in rock simulants exhibiting higher friction angles.

As part of the present investigation a detailed review of the scaled model tests was conducted, with a view to identifying data that may be used to validate the variable dilatancy model described in the previous sections of this report. Despite the large number of tests that have been performed, very few lend themselves easily to the desired purpose. There are two important reasons for this difficulty. The first is that

the majority of the tests have been performed under conditions intended to reproduce the uniaxial strain loading that might be experienced by an excavation as a consequence of a distant nuclear burst, for example. As will be discussed later, the selected loading path rapidly leads to conditions that are statically indeterminate and are, therefore, not amenable to analysis in closed form. The second problem is that the region of failed rock around the tunnels is typically relatively large when compared to the dimensions of the cylinder within which it is located. Under such circumstances the influence of the boundary can significantly modify the response. Again, this effect cannot be accounted for in the analytical model. The third problem is that most of the support systems tested exert a nonuniform pressure on the rock simulant unless the model is subjected to isotropic loading. As currently developed, the analytical model requires that the support be approximated as a uniform internal pressure. The approximation may be acceptable for rock bolted or backpacked structures, but is inappropriate for integral steel or concrete liners subjected to nonisotropic loading.

In the following sections the results of a number of laboratory tests are discussed. Considering the problems associated with the uniaxial loading conditions, emphasis is placed on cases in which the loading was isotropic. However, there is also a discussion of the results of selected tests under uniaxial strain conditions.

4-2 ISOTROPIC LOADING OF LOW FRICTION SIMULANTS.

A large number of tests have been performed using a tuff simulant designated RMG-2C2. Typical results from early tests on lined and unlined tunnels in intact rock subjected to static and dynamic loads are reproduced in figure 14. These tests revealed a significant difference between behavior under static and dynamic loads, and dry and saturated conditions. The differences were attributed, in the most part, to pore water effects; with the pore water weakening the specimens in the static tests and strengthening them in the dynamic tests.

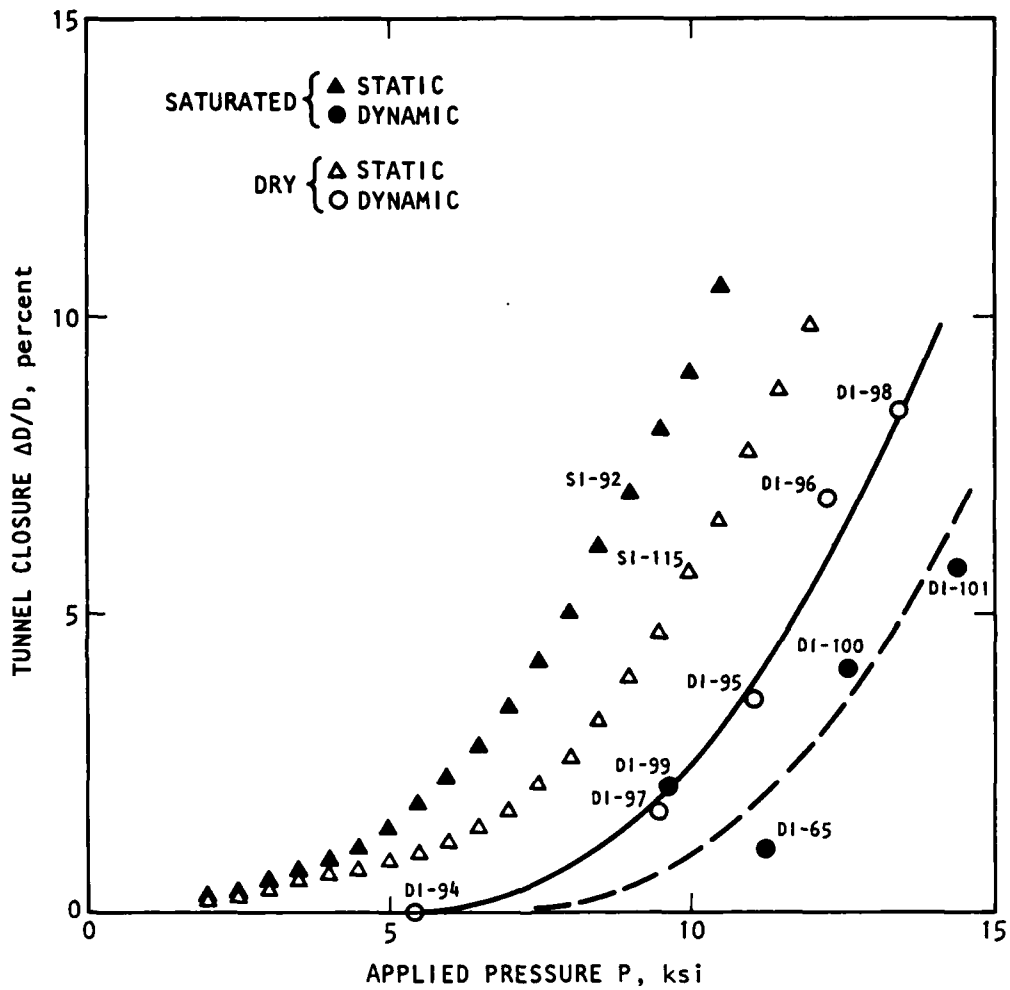


Figure 14. Tunnel closure versus applied pressure for isotropic loading of SRI RMG 2C2. Liner: 6061-T0 aluminum, $a/h = 11.5$.

Following this finding, testing has emphasized static loading of saturated samples. Under such circumstances the properties of the RMG-2C2 simulant are reported to be (SRI, 1979):

Young's Modulus	$E = 1.6 \times 10^6$ psi
Poisson's Ratio	$\nu = 0.18$
Unconfined Compressive Strength	$q = 3200$ psi
Friction Angle	$\phi = 2.5^\circ$

For reasons discussed above we shall consider the case of lined excavations subjected to isotropic loading. Typical results of such tests conducted with different thicknesses of Al 6061 aluminum liner are reproduced in figure 15. Superimposed on the laboratory data are closure versus applied pressure curves computed using a model that assumes associated behavior ($\phi = \phi_*$) for the simulant and the strain hardening property illustrated in figure 16. It may be observed that the analytical model reasonably reproduces the laboratory data. However, as discussed below, this finding cannot be regarded as evidence of the validity of the constitutive model assumed for the rock simulant.

The most important factor affecting the value of this data is the very low friction angle. In figure 17 the tunnel closure histories predicted using full dilatation ($\phi^* = \phi$) and zero dilatation ($\phi^* = 0$) are illustrated for lined and unlined tunnels in the RMG-2C2 simulant. (Models based on these two extreme assumptions have been referred to as the Hendron and Newmark models respectively.) If figure 17 is compared to figure 15 it is clear that the differentiation between the full dilatation and zero dilatation is not an important phenomenon for such a low friction material.

The second consideration for these tests on low friction materials is the boundary conditions. For the isotropic loading conditions considered here this effect can be investigated analytically using the solution for a thick-walled cylinder subjected to uniform internal and external pressures (p and P_0). The extent of the plastic region in the cylinder is given by the equation (Kennedy, 1975):

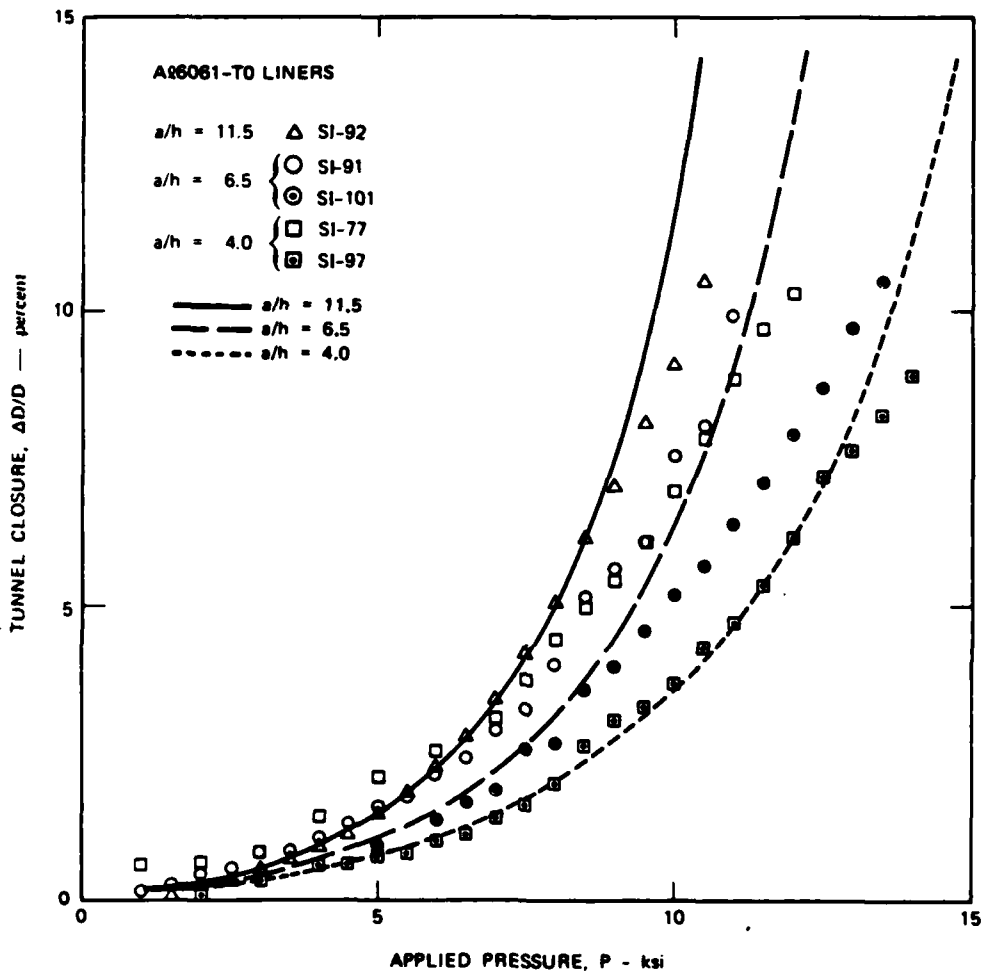


Figure 15. Tunnel closure versus applied pressure for static isotropic loading of SRI RMG 2C2 - the curves are based on a closed-form solution that neglects out-of-plane plastic strain .

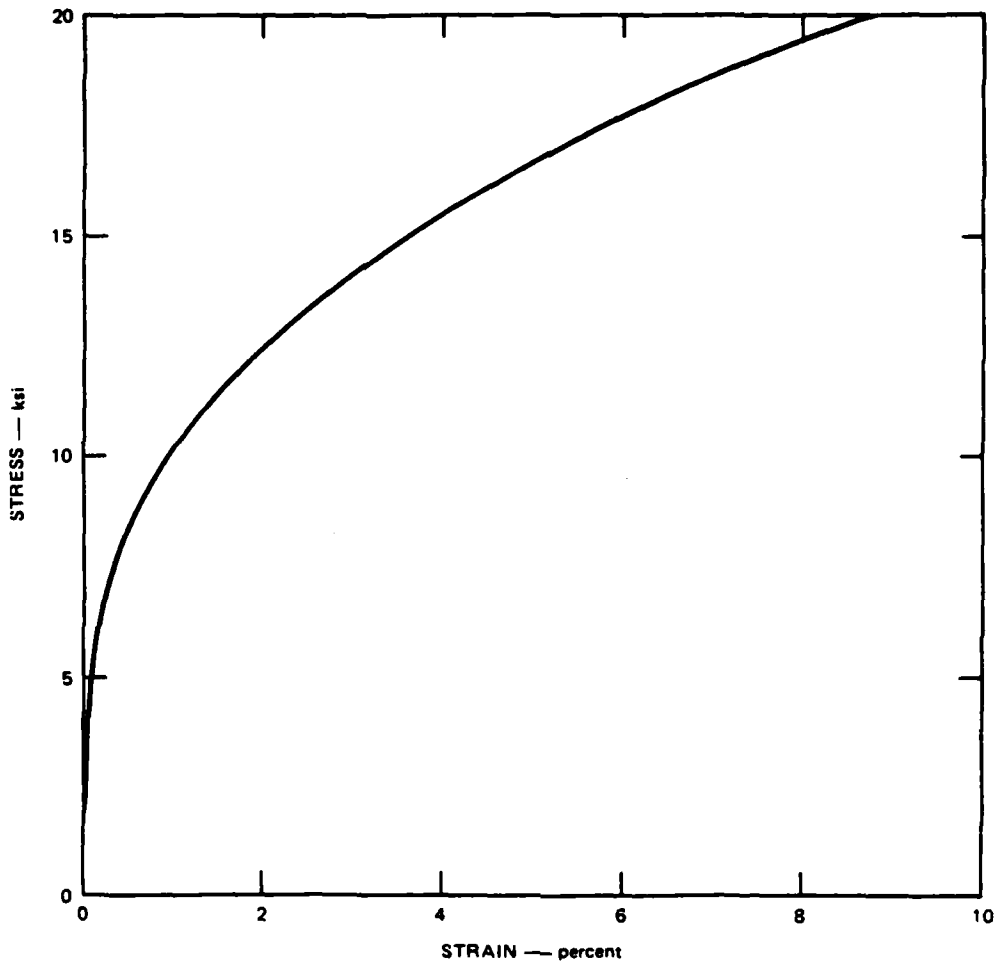


Figure 16. Uniaxial stress-strain curve for Al 6061-T0 in compression .

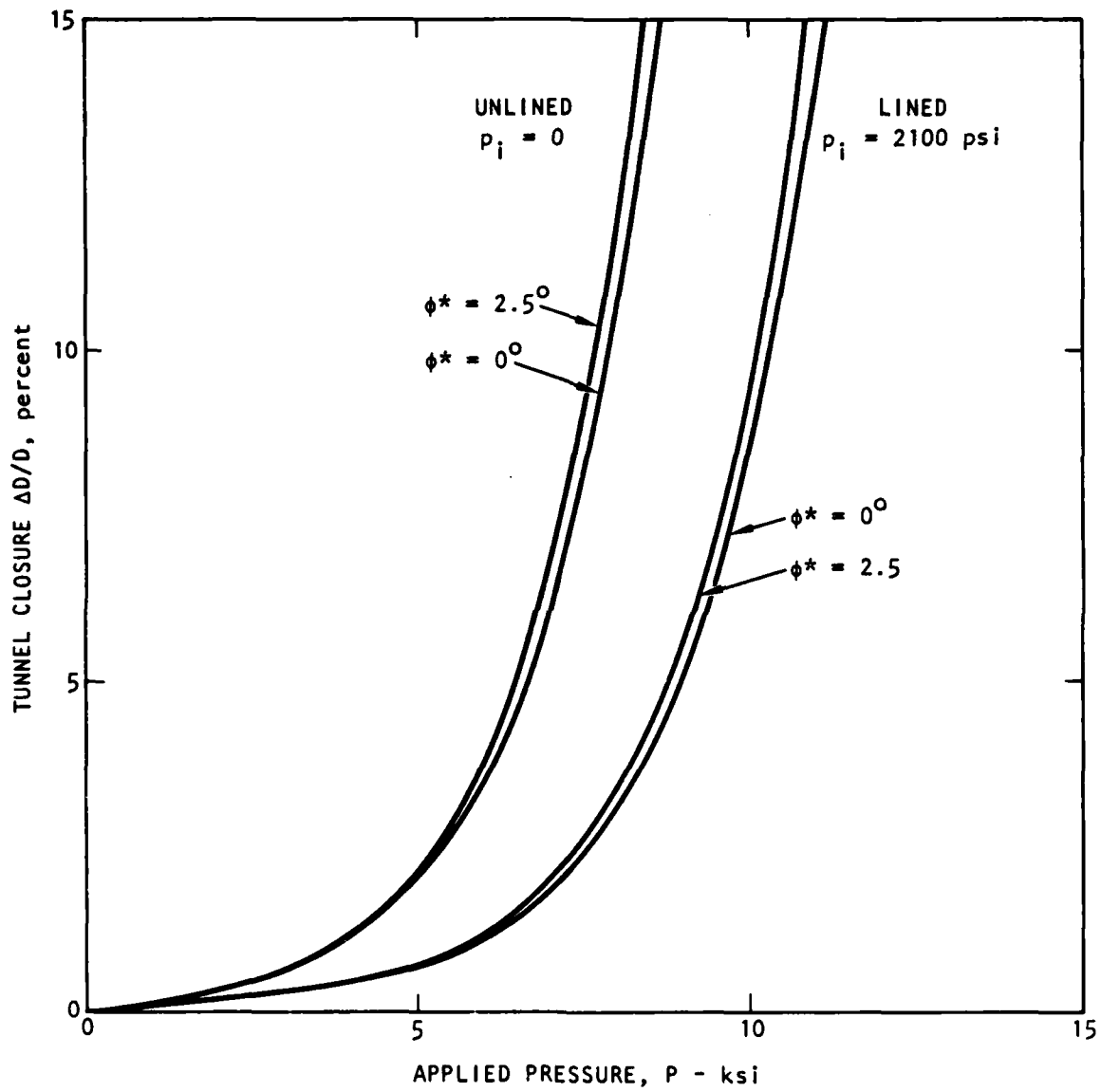


Figure 17. Calculated tunnel closure versus applied pressure curves using closed form solution with constant dilatation angles. SRI rock simulant RMG 2C2 with lined (1015 steel liner, $a/h = 18$) and unlined tunnel.

$$R^{(K_p+1)} - \frac{(K_p + 1)}{(K_p - 1)} \left(\frac{b}{a}\right)^2 R^{(K_p-1)} + \frac{2}{(K_p - 1)} \left(\frac{b}{a}\right)^2 \left[\frac{p^o + \frac{q}{(K_p - 1)}}{p + \frac{q}{(K_p - 1)}} \right] = 0 \quad (26)$$

in which a and b are respectively the internal and external radii of the cylinder and R is the radius of the plastic zone normalized by a. As noted earlier, the radius of the plastic zone around a tunnel in an infinite region is given by:

$$R_o = \left[\frac{2}{K_p + 1} \frac{p^o + \frac{q}{(K_p - 1)}}{p + \frac{q}{(K_p - 1)}} \right]^{1/(K_p-1)} \quad (27)$$

which is a special case of the thick walled cylinder equation, that can be deduced by allowing (b/a) to approach infinity. Equation (26) can be solved to define the minimum thickness below which the thick-walled cylinder will be completely plastic. This thickness is a function of the internal and external pressures and the material properties:

$$\left(\frac{b}{a}\right)_{\min} = \left[\frac{p^o + \frac{q}{(K_p - 1)}}{p + \frac{q}{(K_p - 1)}} \right]^{1/(K_p-1)} \quad (28)$$

Referring to equation (27), it can be seen that this minimum thickness can be much larger than the extent (R_o) of the plastic zone around a hole in an infinite region. Specifically:

$$\left(\frac{b}{a}\right)_{\min} = \left(\frac{2}{K_p - 1}\right)^{1/(K_p-1)} R_o \quad (29)$$

Clearly the difference is more important for very low friction angle materials, such as the RMG-2C2 rock simulant.

This can be illustrated best by solving equation (26) to obtain the relationship between the radius of the plastic zone and the dimensions of the thick-walled cylinder for a particular choice of material properties. Such a relationship is illustrated in figure 18. That figure is for the case of a thick-walled cylinder of RMG-2C2 without internal pressure and with external pressure expressed as a multiple of the uniaxial strength. At relatively high loads the extent of the plastic zone in the finite region is considerably enlarged, which indicates that the displacements observed in these models will be much greater than would be observed in the field. Hence the results of tests of tunnels in RMG-2C2 simulant are unsatisfactory for validating the variable dilatancy model on two counts. First, the friction angle is too small to provide a differentiation between alternative dilatation models. Second, the results of the model studies are strongly influenced by the boundary conditions.

4-3 ISOTROPIC LOADING OF HIGH FRICTION SIMULANTS.

A series of tests on lined and unlined tunnels were performed by SRI on a relatively high friction simulant designated 6B. Material properties of this simulant are reported (Lindberg, 1983):

Young's Modulus	$E = 2.0 \times 10^6$ psi
Poisson's Ratio	$\nu = 0.25$
Unconfined Compressive Strength	$q = 4300$ psi
Friction Angle	$\phi = 33^\circ$

Results for four cases of isotropic loading are reproduced in figure 19 (Lindberg, 1983). Superimposed on the experimental data are theoretical results obtained using the full (associated) dilatation model. The theoretical results are for three different steel liner thicknesses in addition to the unlined case.

It may be observed from figure 19 that there are significant differences between the experimental data and the theoretical model. The most obvious is that the effect of the liner is overestimated in all cases.

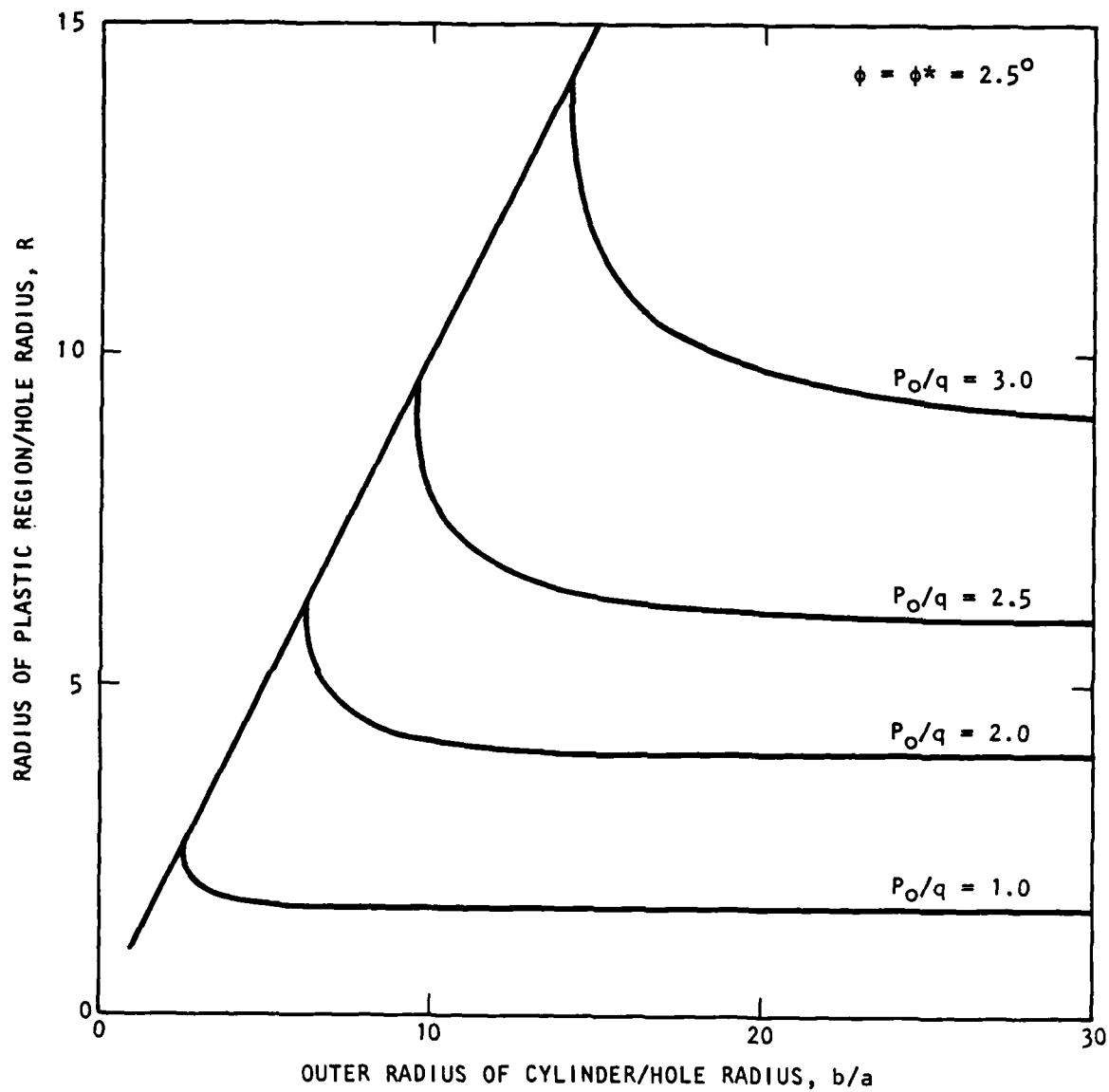


Figure 18. Relationship between radius of plastic region around hole and radius of thick-walled cylinder. Curves are plotted for selected normalized external pressures for material with a friction angle of 2.5° .

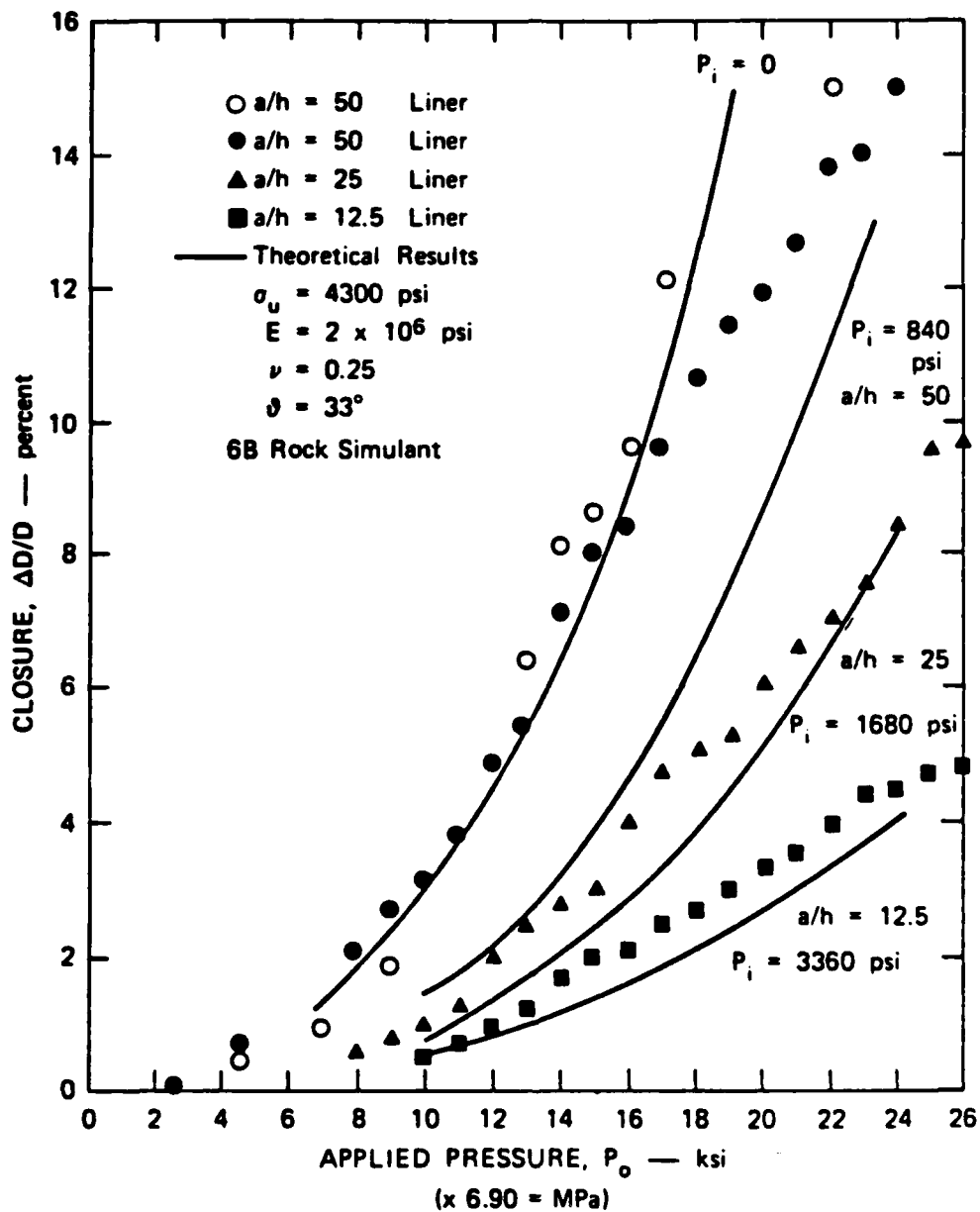


Figure 19. Comparison of Hendron theory (curves) with laboratory experiments (points) for symmetric loading.

This is relatively easy to explain for the very thin liner since it was reported that the thin liners were severely buckled during loading. For the thicker liners it must be assumed that their effect is delayed by a certain amount of "consolidation" and elastic response before the full support pressure is mobilized, when the liner is fully yielding.

A second important departure of the experimental behavior from the theoretical model is that the theoretical model appears to overestimate the closure at higher loads. Unfortunately the uncertainty as to the efficiency of the liners makes it difficult to quantify this effect. Despite this uncertainty it is instructive to compare these test results with predictions made using the variable dilatancy model. First, however, it is appropriate to evaluate the importance of the boundary conditions, and to ascertain whether these are an important consideration in this case.

In figure 20 the relationship between the radius of the plastic region and the radius of a thick-walled cylinder of 6B rock simulation subjected to external pressure is illustrated. The format of that figure is the same as figure 18, except that the vertical scale has been enlarged because the effect of using a higher friction simulant is to restrict the growth of the plastic region. From the figure it is clear that once the boundaries lie beyond approximately six tunnel radii they cease to have a significant influence. Since the tests performed by SRI satisfy this constraint we conclude that, for high friction simulants, the tunnel deformation should be relatively unaffected by the fact that the test specimen is finite.

Figure 21 illustrates the relationship between tunnel closure and support pressure for alternative assumptions regarding the maximum inelastic strain. Superimposed on the plots are the results extracted from figure 19, using the theoretical level of support offered by the three liners. It is evident that either the effect of the liners is being overestimated or that there is an initial displacement that is not accounted for

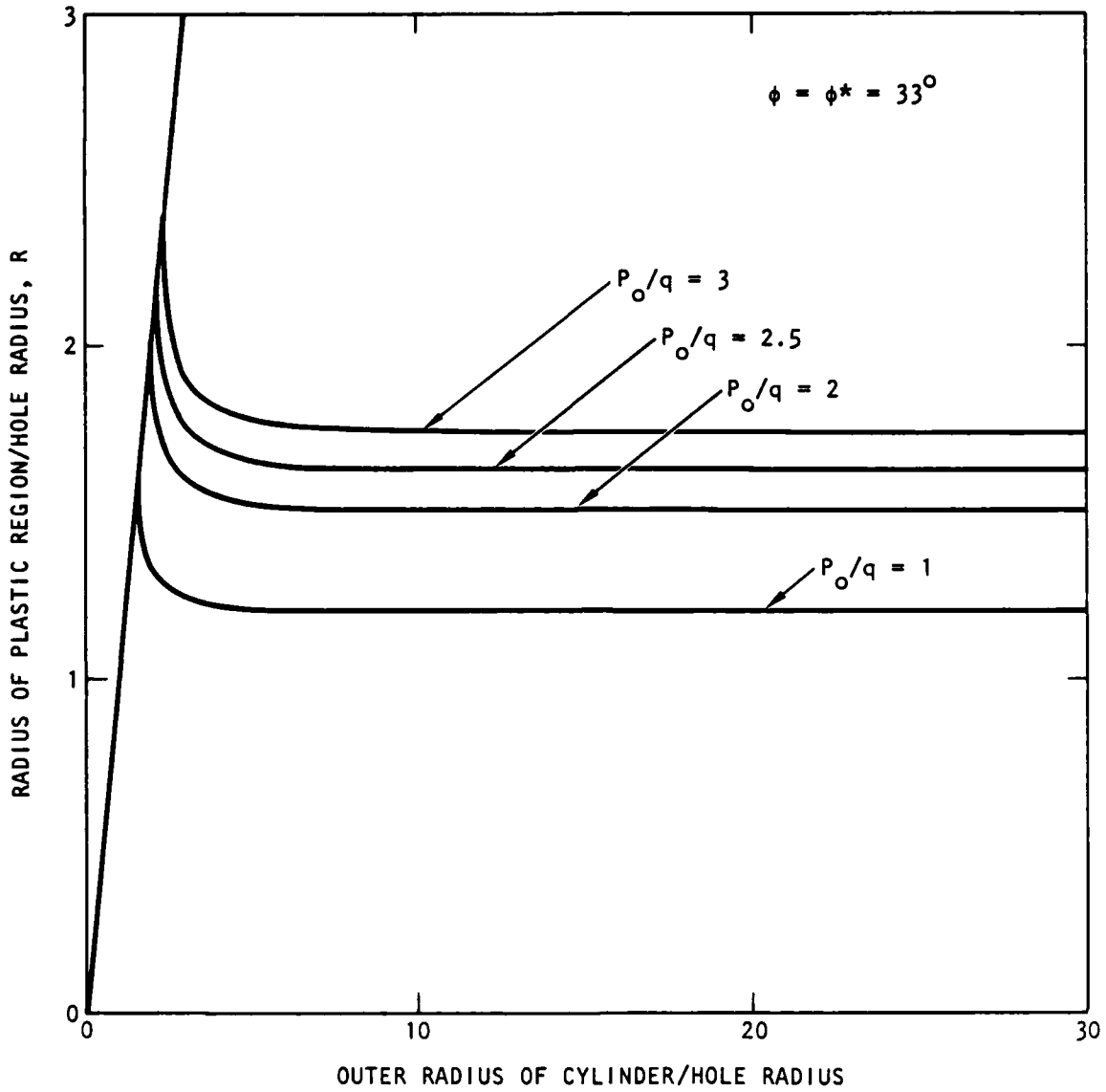
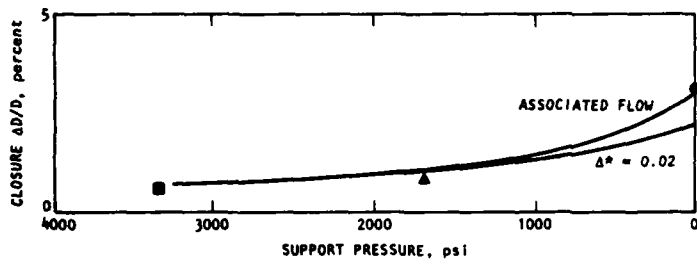
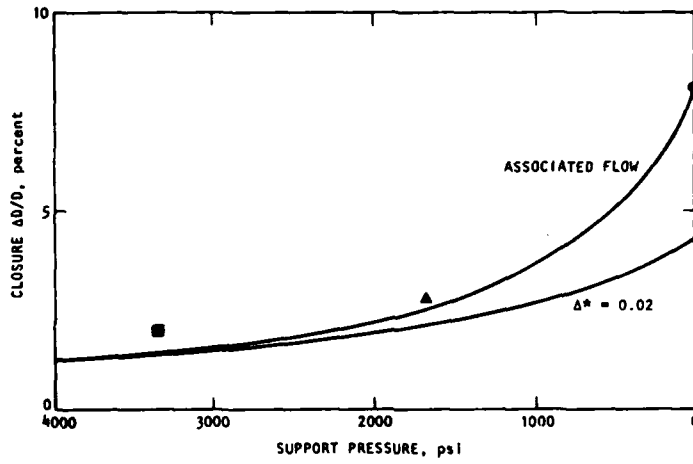


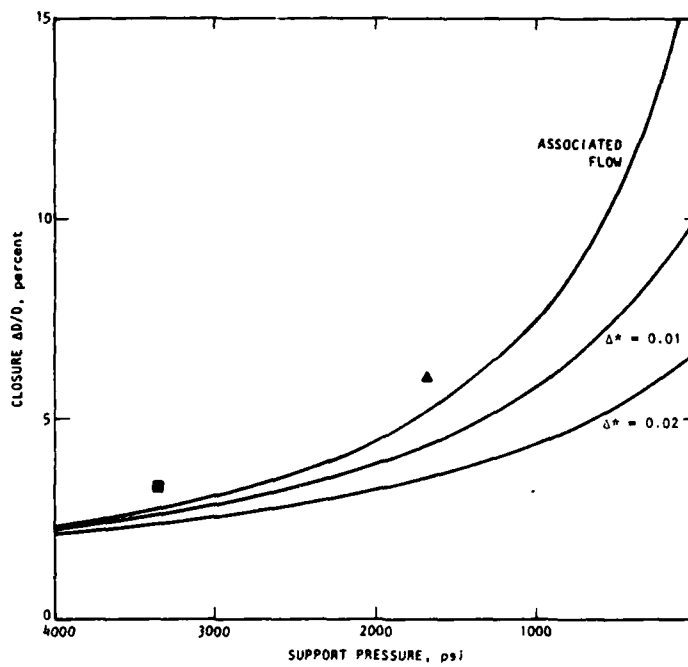
Figure 20. Relationship between radius of plastic region around hole and radius of thick walled cylinder. Curves are plotted for selected normalized external pressures for material with a friction angle of 33° .



(a)



(b)



(c)

AAB96

Figure 21. Closure versus support pressure for an external pressure of 10, 15, and 20 ksi.

in the theoretical model. It is difficult to reconcile either of these alternatives with the fact that the closures appear to be underestimated at low loads. Despite this problem, the results of this comparison do tend to suggest that the variable dilatancy model will provide an improved simulation of observed behavior. There is evidence that the rate of increase of closure does decrease at the higher loads. If forced to estimate the maximum inelastic strain using this limited data base it might be set at approximately 10 percent.

4-4 BIAXIAL LOADING OF HIGH FRICTION SIMULANTS.

Additional data for the response of lined tunnels in SRI rock simulant 6B is provided by Lindberg (1983), but for the case of simulated uniaxial loading. In this case the solution for the closure is not available in closed form because the problem rapidly becomes statically indeterminate. However, in an attempt to gain further data on the properties of the 6B, it was considered appropriate to perform analysis of the uniaxial loading tests using a finite element code capable of simulating a Mohr-Coulomb material, providing associated behavior is assumed.

Results from the uniaxial strain model studies performed by SRI are reproduced in figure 22. Before attempting to reproduce those results a preliminary calculation was performed for the case of isotropic loading. The result of that calculation is illustrated in figure 23, where it is used to verify that the numerical prediction was in good agreement with the earlier closed-form solution. Having thus confirmed the adequacy of the numerical model, two alternative simulations of the uniaxial strain condition were investigated. First, uniaxial strain was imposed by restraining lateral displacement of the model. To be reasonably consistent with the laboratory configuration, the lateral boundary was placed 6.5 tunnel radii from the centerline of the tunnel. Since this boundary is comparatively close to the tunnel, it is probable that the first boundary conditions unrealistically restrains the model. Second, a confining stress equal to that generated in the free field under

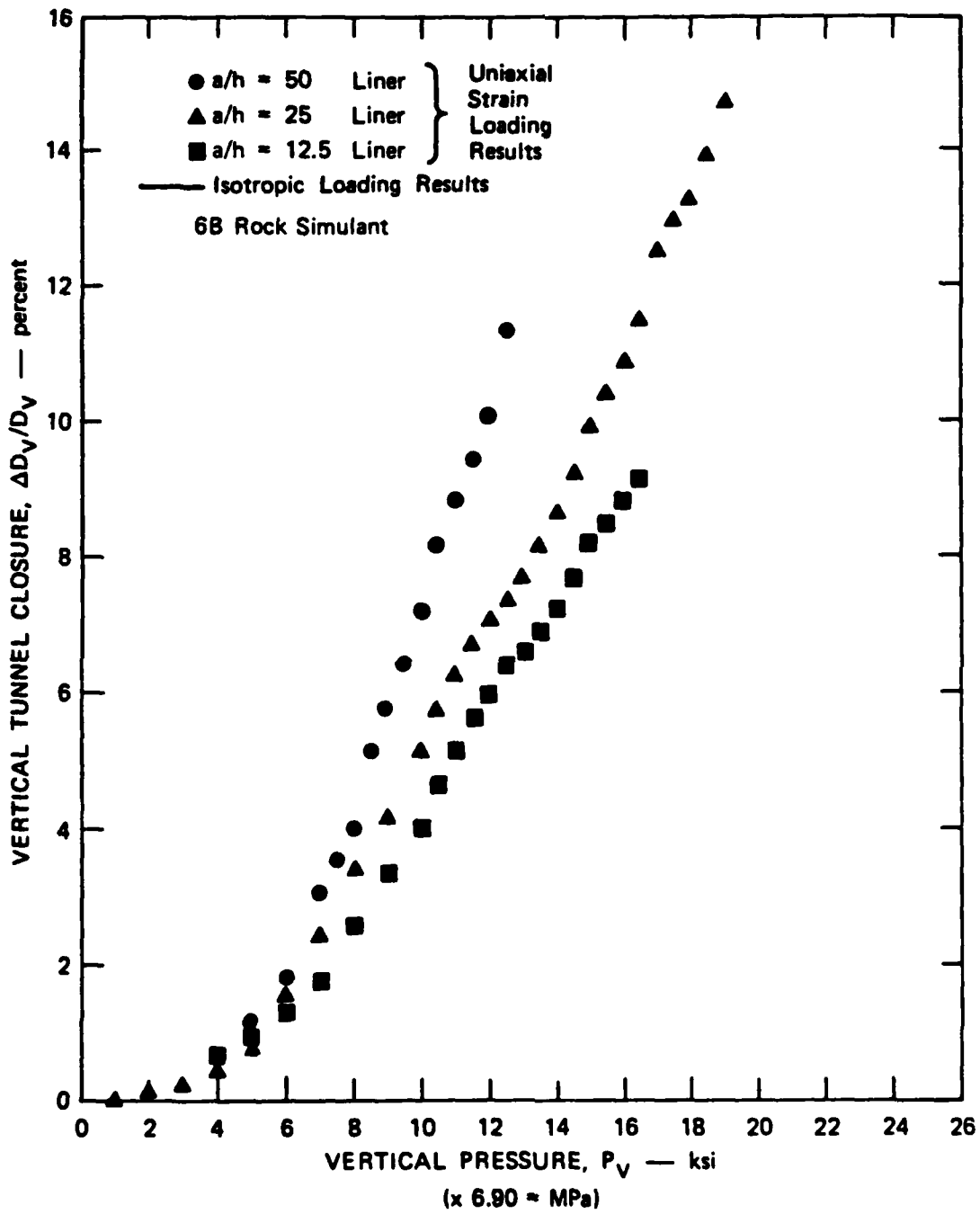


Figure 22. Experimental tunnel closure versus applied pressure points for uniaxial strain loading.

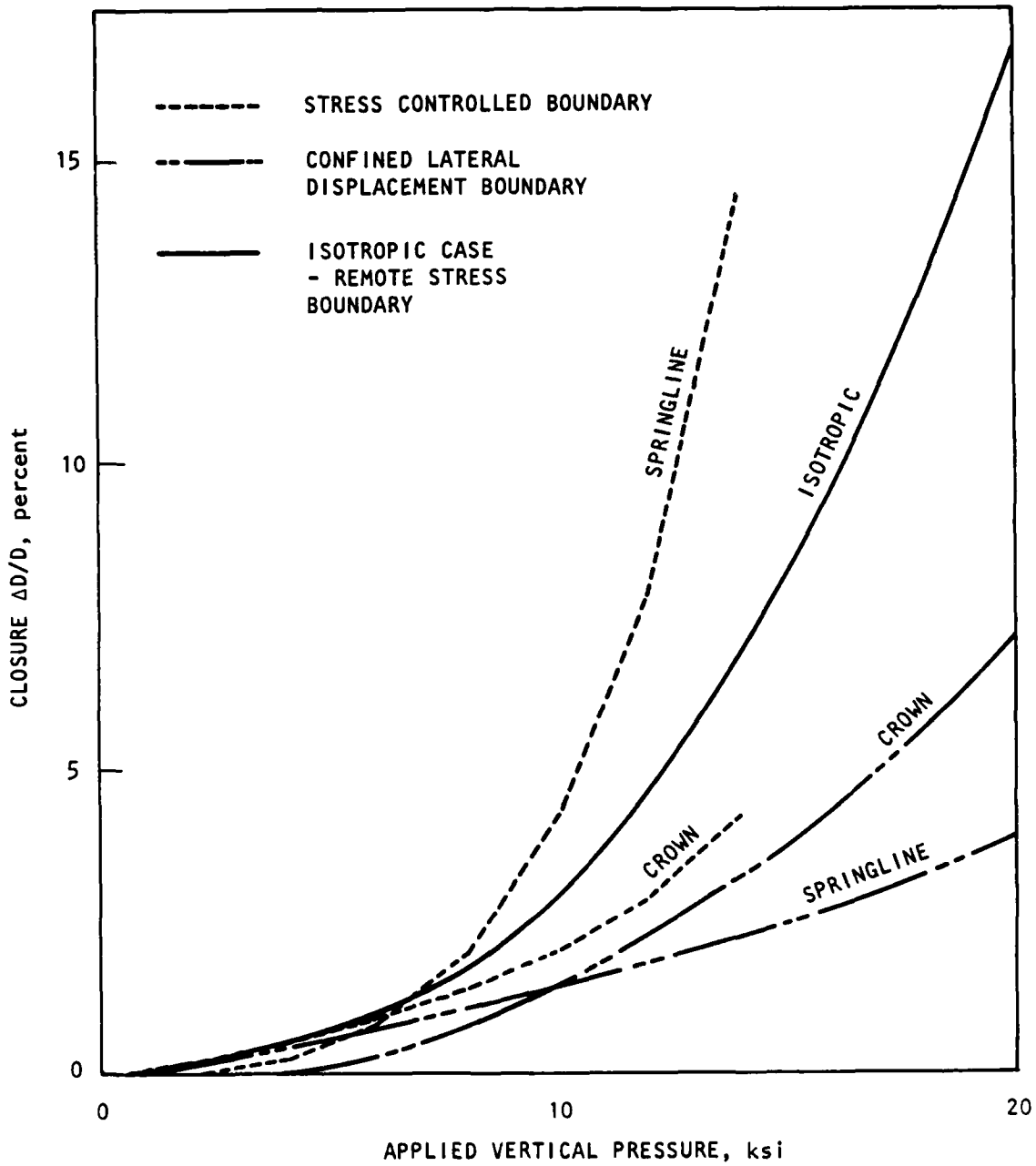


Figure 23. Comparison of isotropic loading and biaxial loading under numerical prediction of behavior of tunnel in rock simulant 6B.

conditions of uniaxial strain was imposed. This second condition is probably too compliant, which suggests that displacement of the tunnel wall would be overestimated.

Results from the two numerical simulations of uniaxial strain loading are illustrated in figure 23. Two aspects of the behavior are very interesting. First, the results are extremely sensitive to the assumed boundary conditions, with larger displacements resulting from the stress controlled boundary. Second, the displacements are significantly smaller than observed in the laboratory, even though the liners were not incorporated in the numerical simulation. Since the stress controlled boundary conditions should have resulted in an overestimate of the tunnel closure it appears that there must be some deficiency in the material model. Probably, either the reported properties are incorrect, or the Mohr-Coulomb model does not adequately describe the material behavior. These observations are reinforced by the fact that the numerical model assumed associated behavior, and therefore predicts the maximum possible dilatation.

4-5 EFFECT OF TUNNEL REINFORCEMENT.

SRI provided data on a series of tests to evaluate the effect of rockbolts as a means of tunnel hardening. These tests were intended to simulate 18 ft diameter tunnels either unsupported or supported with #20 rockbolts on 2 ft centers. This degree of reinforcement amounts to an internal pressure of approximately 680 psi (4.7 MPa), if it can be assumed that the bolts exert a pressure equal to the yield stress of the steel. The tests selected for analysis here were designated by SRI as LSUX-35 and LSUX-39. The reported properties of the rock simulant HF5 used for these two tests are, for material from the mix used in LSUX-39:

Young's Modulus	$E = 1.4 \times 10^6 \text{ psi}$
Poisson's Ratio	$\nu = 0.25$
Unconfined Compressive Strength	$q = 4900 \text{ psi}$
Friction Angle	$\phi = 40^\circ$

Since the results of the simulation of the uniaxial loading tests performed on material 6B indicated a considerable sensitivity to the boundary conditions, the load path used by SRI was followed as closely as possible. The record of the relationship between the vertical and lateral pressures during the LSUX-39 test is reproduced in figure 24. (This relationship is generated by slaving the lateral pressure to maintain zero circumferential strain at sample points close to midheight of the cylinder of rock simulant.) To simplify the numerical modeling, this load path was idealized as three linear segments and the internal support pressure was applied incrementally during the first load segment.

Results of the laboratory tests are reproduced in figure 25 and those of the numerical simulation in figure 26. In both cases the predicted displacements are substantially less than observed in the laboratory. Since any uncertainty in the loading conditions was removed by carefully following the laboratory procedure, it is concluded that there are deficiencies in the material description. Once again, this may be in the definition of the properties or in the constitutive model. The most likely explanations are either that the Mohr-Coulomb model substantially under-predicts the extent of the plastic region or that some other failure mechanism, such as near surface spalling, is occurring.

4-6 CONCLUSIONS.

The results of evaluation of the results of laboratory tests using models based on the closed-form solution and a finite element procedure indicate that the Mohr-Coulomb model substantially under-predicts the closure even when associated behavior is assumed. This implies that the material description used is inadequate, either in the choice of material properties or in the constitutive model. Not enough is known about the material properties (uniaxial strength, elastic modulus, Poisson's ratio, and friction angle) to determine whether that is the source of error. However, it is reasonable to question whether appropriate account has been taken of scale effects that

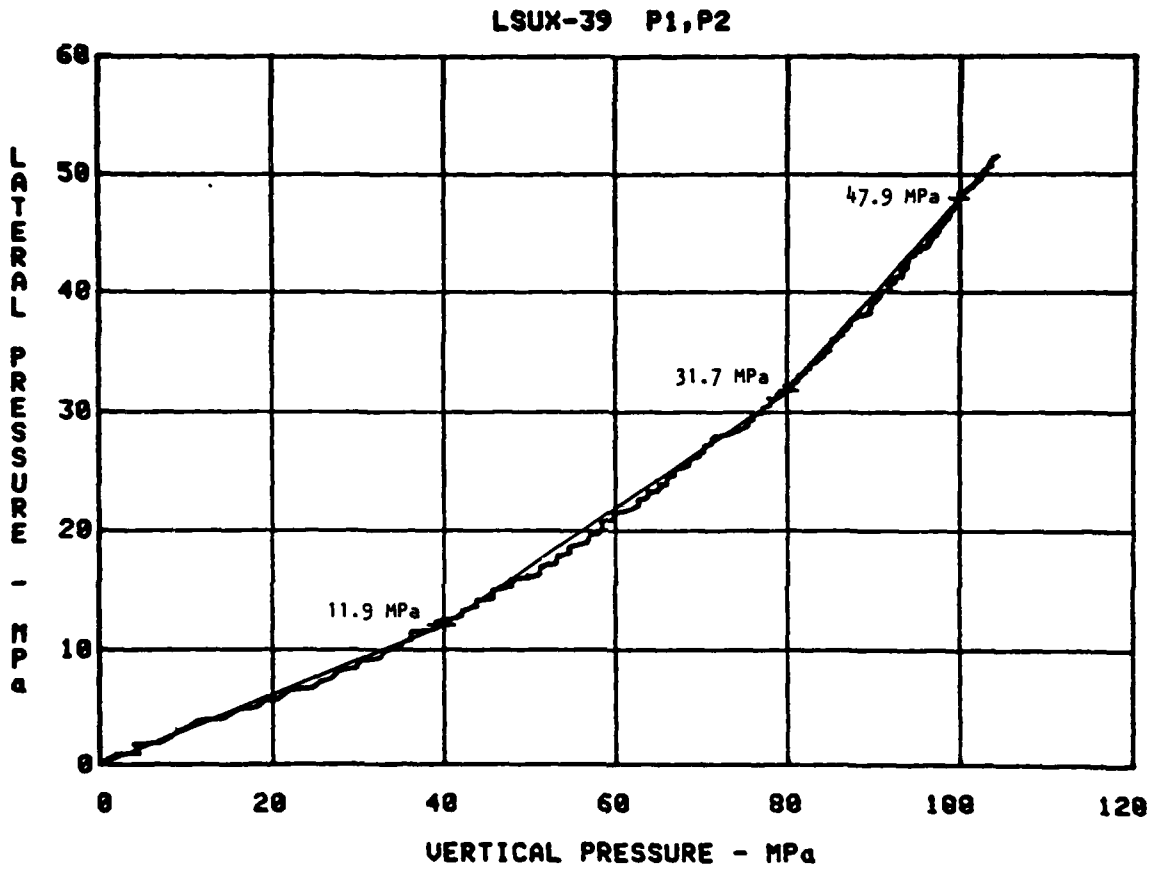


Figure 24. Load path for SRI test LSUX-39 on HF5 rock simulant.

EFFECT OF #20 ROCK BOLTS IN HF5 SIMULANT

($\sigma_u = 5000$ psi, $\phi = 40^\circ$)

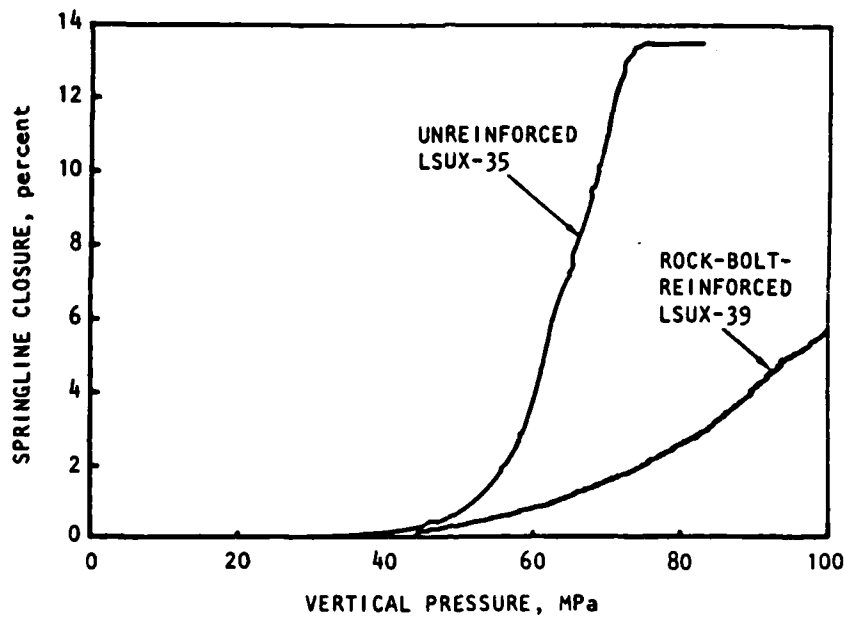
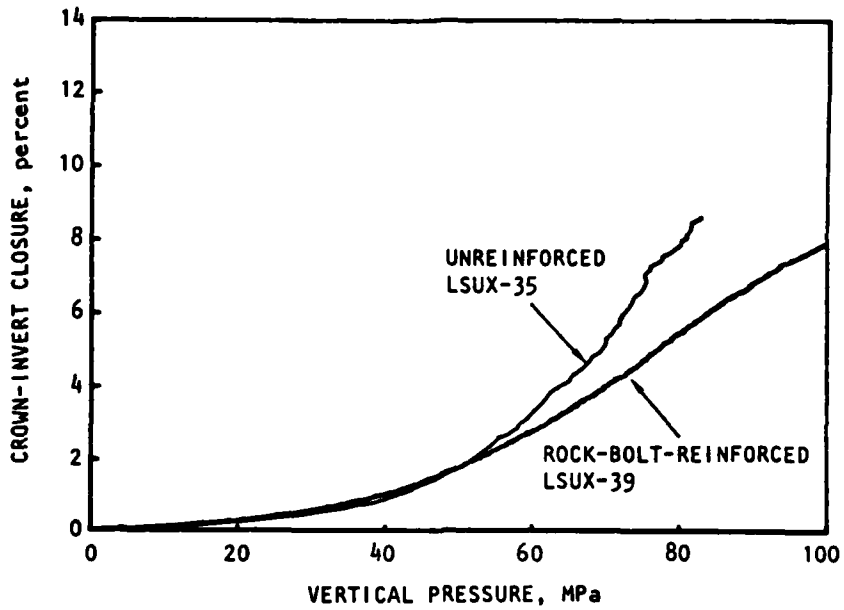


Figure 25. Experimental results from SRI tests LSUX-35 and LSUX-39.

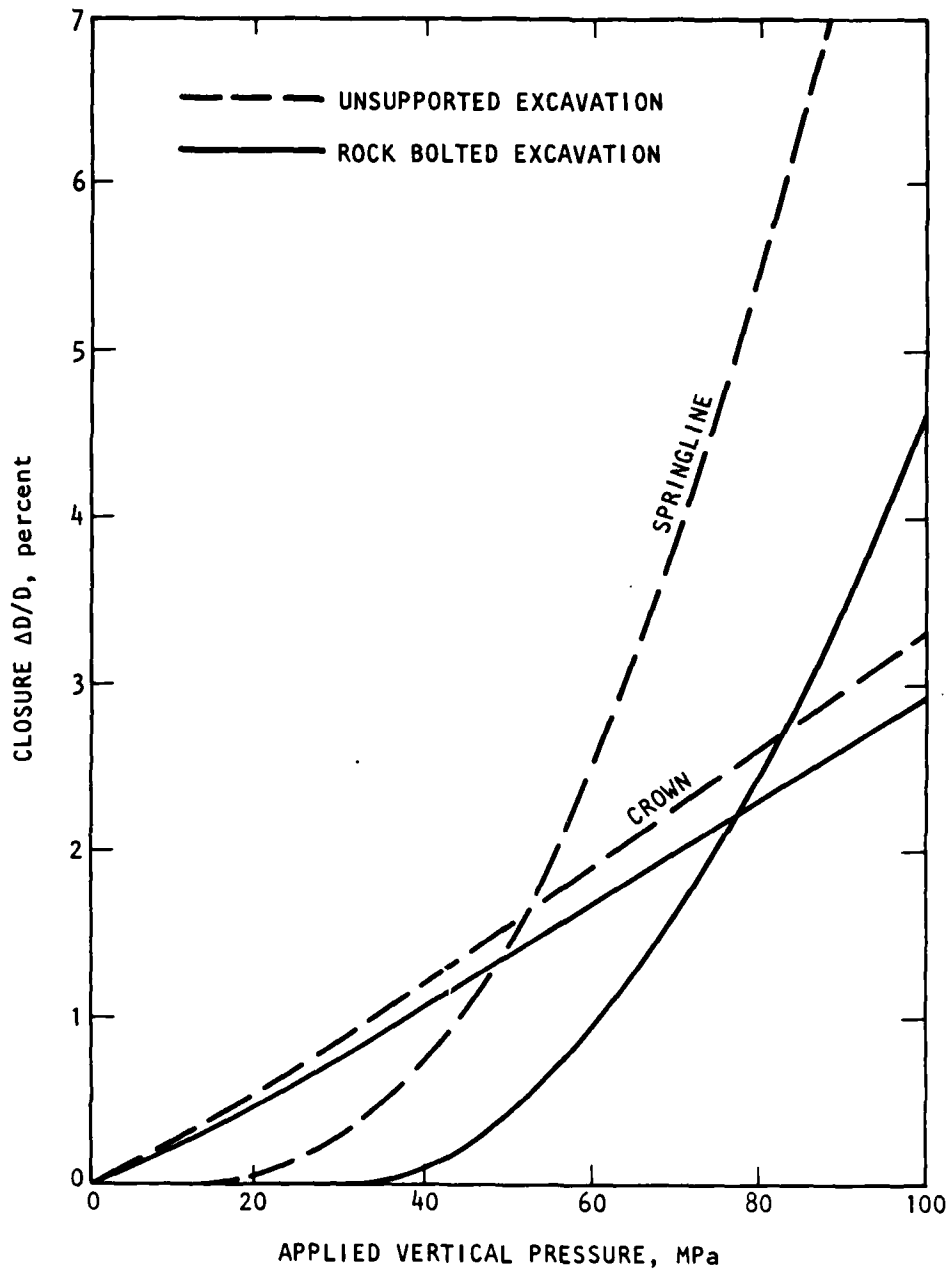


Figure 26. Numerical predictions of closure of reinforced and unreinforced tunnels in rock simulant HF5.

are important in reality but are ignored in the mathematical descriptions.

Given the uncertainty in the material properties it is difficult to draw any firm conclusions about the adequacy of the Mohr-Coulomb model. However, the fact that the models based on associated behavior consistently under predict the observed deformation, except in the case of isotropic loading, suggests that the simple constant friction plasticity model is inadequate. Additional laboratory testing would be required to identify the nature of the deficiency, but it seems most likely that the model underpredicts the extent of the plastic region around the tunnel. Careful inspection of cross sections of a tunnel structure after testing could be used as a means to test this hypothesis. Also, consideration could be given to monitoring microseismic emissions during tests to detect regions of inelastic behavior.

SECTION 5

CONCLUSIONS

This study had as its main objective the development of a mathematical model of a deep tunnel based on an improved dilatancy model of the rock, so as to overcome the principal shortcoming of existing models based on the assumption of a constant dilatancy angle.

A review of published laboratory experiments on rock dilatancy revealed that very few experimental data could be used to support the development of an improved dilatation model for rock at low confining pressure. Reasons for this deficiency can be found in the use of "soft" testing machines, which are responsible for the lack of data beyond the peak stress, or in the fact that many experiments were conducted at very high confining pressure, so as to simulate the behaviors of rock at great depth. Some limited experimental evidence suggest, however, that at peak strength, the maximum theoretical dilation rate is achieved (associated flow rule) and that it progressively diminishes afterwards with the plastic shear strain. On that basis, a very simple dilatation model was implemented which involved the introduction of a single parameter, the maximum inelastic volume increase, in contrast to the constant dilatancy angle parameter used in previous dilatation models. This constitutive model fits between the two extremes: constant dilatation models - the so-called full dilatation model (dilatancy angle constant and equal to the friction angle) - and the zero dilatation model (zero dilatancy angle). It has the advantage of relying on a physically meaningful parameter.

The improved dilatation model of rock was then used for the development of two mathematical models of a deep cylindrical tunnel, one for hydrostatic, the other one for nonhydrostatic loading. For the hydrostatic loading, it was shown that closure of the tunnel requires the solution of a nonlinear ordinary differential equation, and for the nonhydrostatic loading a system of nonlinear partial differential equations of

the hyperbolic type. In both cases, the numerical procedures are discussed in detail: Runge-Kutta for the hydrostatic loading, and the method of characteristics for the nonhydrostatic case. The numerical models have, however, been devised in such a way that more elaborate dilatation models - accounting, for example, for the influence of the mean pressure - can be implemented in a straightforward manner.

Model test experiments were then reviewed in an attempt to validate the improved dilatation model. The review proved, however, to be inconclusive because:

1. Many tests have been performed using a very low friction angle (2.5 deg) rock simulant, which, because it hardly dilates, can never provide a clear differentiation between full dilatation and zero dilatation models.
2. Numerical simulation of tests conducted with a high-friction rock simulant demonstrates that the observed closure is generally underpredicted with a linear Mohr-Coulomb material even if a full-dilatation model is assumed. This implies that a simple linear Mohr-Coulomb criterion is not sufficient to describe the behavior of rock during failure.

Although the elastoplastic models developed in the course of this investigation are based on a relatively simple constitutive law, they nonetheless represent a significant improvement over previous analytical models. These models are, however, best used for parametric analyses and/or to delimit the conditions for which a more sophisticated (but costly) finite element analysis is warranted. In that regard, design charts similar to those developed during a previous investigation should be devised (AA, 1983). Such charts would enhance the practical usefulness of the models developed in this study.

SECTION 6

LIST OF REFERENCES

1. Agbabian Associates. (1983) "An Investigation of the Failure Resistance of Rockbolted Tunnels for Deep Basing," R-8227-5534. El Segundo, CA, prepared for Defense Nuclear Agency.
2. Algorithm 392 of CACM, "Systems of Hyperbolic Partial Differential Equations."
3. Bieniawski, Z.T. (1967) "Mechanism of Brittle Fracture of Rock. Part I - Theory of the Fracture Process, Part II - Experimental Studies, Part III- Fracture in Tension and Under Long-term Loading," Int. Jnl. Rock Mech. Min. Sci, Vol. 4, pp 356-438.
4. Brace, W.F., Paulding, B.W. and Scholz, C. (1966) "Dilatancy in the Fracture of Crystalline Rocks," Jnl. Geophys. Res., Vol. 71, pp 3939-3953.
5. Bridgman, P.W. (1949) "Volume Changes in the Plastic Stages of Simple Compression," Jnl. Appl. Phys., Vol. 20, pp 1241-1251.
6. Brown, E.T. et al. (1983) "Ground Response Curves for Rock Tunnels," Jnl. Geotech. Eng. Div. Am. Soc. Civil Eng., 109:1, pp 15-39
7. Cook, N.G.W. (1970) "An Experiment Proving Dilatancy is a Pervasive Volumetric Property of Brittle Rock Loaded to Failure," Rock Mech., Vol. 2, pp 181-188.
8. Detournay, E. (1985) "An Approximate Statical Solution of the Elastoplastic Interface for the Problem of Galin with a Cohesive-Frictional Material," submitted to Int. Jnl. Solids and Structures.
9. Detournay, E. (1983) "Two-Dimensional Elasto-plastic Analysis of a Deep Cylindrical Tunnel Under Non-hydrostatic Loading," Ph.D. dissertation, University of Minnesota.
10. Edmond, J.M. and Paterson, M.S. (1972) "Volume Changes During the Deformation of Rocks at High Pressures," Int. Jnl. Rock Mech. Min. Sci., Vol. 9, 1972, pp 161-182.
11. Gerogiannopoulos, N.G. and Brown, E.T. (1978) "The Critical State Concept Applied to Rock," Int. Jnl. Rock Mech. Sci. and Geomech., Vol. 15, pp 1-10.
12. Hendron, A.J. Jr., and Aiyer, A.K. (1971) "Stresses and Strains Around a Cylindrical Tunnel in an Elasto-plastic

- Material with Dilatancy," Omaha Dist., Corps of Engineers, Jan.
13. Henrici, P. (1962) "Discrete Variable Methods in Ordinary Differential Equations," John Wiley and Sons, Inc., New York.
 14. Kennedy, T.C. (1975) "Laboratory Investigation of Response of Deep-Buried Structures," SRI Intl., Menlo Park, CA, for DNA, Oct.
 15. Labreche, D.A. and Auld, H.E. (1980) "Analysis of Tunnel Linings for Deep Basing Structures," AFWL-TR-80-5. Kirtland AFB, NM: Air Force Weapons Laboratory.
 16. Ladanyi, B. and Don, N. (1970) "Study of Strains in Rock Associated with Brittle Failure," Proc. 6th Can. Rock Mech. Symp., Montreal, pp 49-64.
 17. Lindberg, H.E. (1983) "Comments on Tunnel Hardening for Deep Basing," SRI Intl., Jun.
 18. Masseau, J. (1899) *Memoire sur l'integration Graphique Des Equations Aus Derivees Partielles*, Ann. Ass. Ing. Ec. Gand. Reprinted as Edition du Centenaire, Comite National du MECE, Brussels, 1952.
 19. Muskhelishvili, N.I. (1962) *Some Basic Problems of the Mathematical Theory of Elasticity*, Noordhoff, Groningen.
 20. Newmark, N.M. et al. (1970) "Ground Motion Technology Review," SAMSO, TR-70-114, Nathan M. Newmark Consulting Engineering Services, Urbana, IL, Apr.
 21. Reed, M. et al. (1983) "Deep Underground Technical Review - A State-of-the-Art Analysis," AFWL-TR-82-30, Air Force Weapons Lab, Kirtland AFB, NM, Mar.
 22. Salencon, J. (1969) "Contraction Quasi-Statique d'une Cavité a Symétrie Sphérique ou Cylindrique dans un Milieu Elastoplastique," *Annales des Ponts et Chaussées*, Vol. 4, pp 231-236.
 23. Shock, R.N., Heard, H.C., Stephens, D.R. (1973) "Stress-Strain Behavior of a Grandodiorite and Two Graywackes on Compression to 20 Kilobars," *Jnl. of Geophys. Research*, 78:26, Sep.
 24. SRI International (1979) "Theoretical and Laboratory Study of Deep-Based Structures, Vol. II - Model Tests and Analysis of Mighty Epic Structures," SRI Intl., Menlo Park, CA, for DNA, Jan.

25. Swanson, S.R. and Brown, W.S. (1972) "The Influence of State of Stress on the Stress-Strain Behavior of Rocks," Jnl. Basic Eng., Trans. ASME, Vol. 94, Mar, pp 238-242.
26. Zoback, M.D. and Byerlee, J.D. (1975) "The Effect of Micro-crack Dilatancy on the Permeability of Westerly Granite," Jnl. Geoth. Research, 80:5 pp 752-755.

APPENDIX A

ELASTOPLASTIC MODEL OF A DEEP TUNNEL FOR A ROCK WITH VARIABLE DILATANCY

A-1 INTRODUCTION.

The hydrostatic model of a deep tunnel has been the subject of so many papers (see Brown et al., 1983, for an exhaustive list of references), that it might appear unnecessary to devote yet another to the subject. A review of the existing models reveals, however, that in most accounts the dilatancy of the rock - defined as the rate of increase of the inelastic volume change with the plastic shear strain - is assumed constant. This assumption may be responsible for unrealistic prediction of tunnel closure, since it does not set any bound on the volume increase that the material can experience. In some investigations, a variable dilatancy has been implemented, but calculation of the tunnel closure is then based on an approximate solution method.

The objective of this paper is to present a rigorous solution of the tunnel closure, for a general class of materials characterized by a Mohr-Coulomb yield envelope and a plastic dilatation, which may be an arbitrary function of the stress and the plastic shear distortion.

A-2 THE HYDROSTATIC MODEL.

Consider the plane strain model of a cylindrical tunnel of radius a , driven in a homogeneous and isotropic rock mass (see figure 27). A far-field stress of magnitude P^0 acts at infinity (it is assumed that the gravity force can be ignored). Excavation unloading of the prestressed rock mass is simulated by a monotonic decrease of the internal pressure p , from an initial value P_0 to zero. The rock is assumed to behave as an elastoplastic material with a linear Mohr-Coulomb envelope:

$$\tau_3 = K_p \tau_1 - q \quad (30)$$

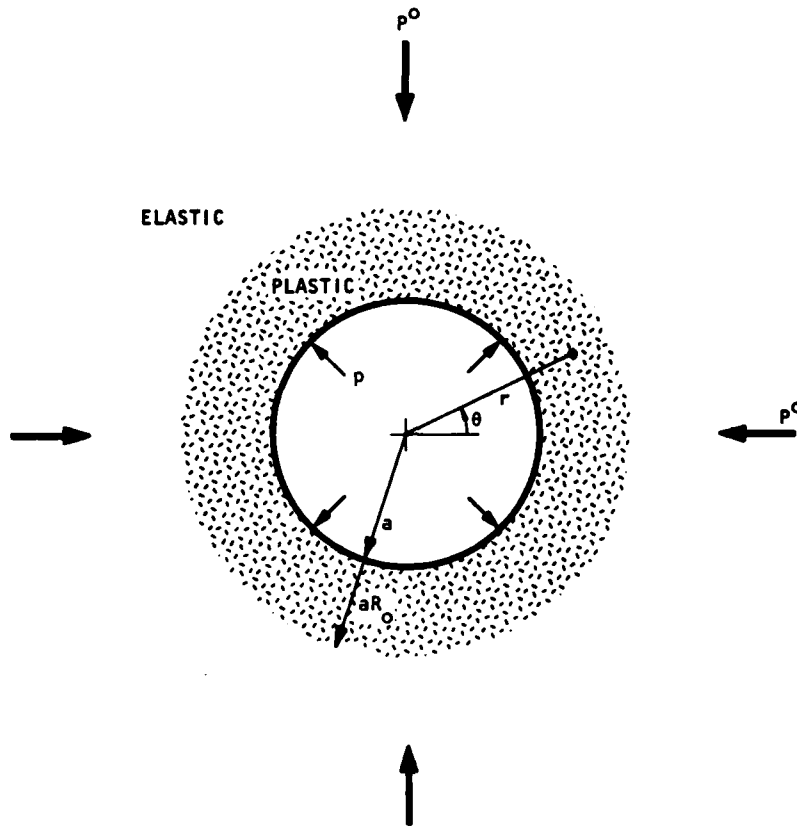


Figure 27. Hydrostatic model.

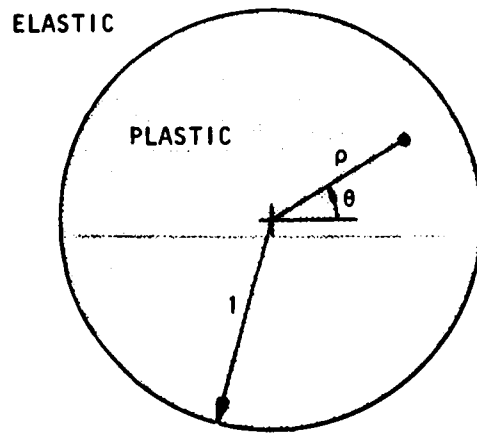


Figure 28. Unit-plane transformation.

in which q is the unconfined compressive strength, K_p the passive coefficient, a function of the friction angle, and tension and extension are taken as positive. We restrict consideration to cases where the out-of-plane principal stress is the strict intermediate stress τ_2 in regions of plastic deformation, so that the normal elastic strain, perpendicular to the plane of deformation, vanishes everywhere. (It can be proven that satisfaction of the inequality $(K_p + 1) > 1/\nu$ represents a sufficient condition to that effect (Detournay, 1985).)

We seek to determine the stress and displacement fields in terms of the radial coordinate r (the problem is axisymmetric) and the internal pressure p , for a general class of materials characterized by a plastic dilatation function of the stress and the accumulated plastic shear strain.

In the early stage of unloading, the rock around the tunnel remains elastic; however, provided that

$$p < \frac{2}{K_p + 1} \left(p^0 + \frac{q}{K_p - 1} \right) - \frac{q}{K_p - 1} \quad \text{with } p^0 > \frac{q}{2} \quad (31)$$

the problem is characterized by the existence of a plastic zone ($a < r < aR_0$) surrounded by an infinite elastic region ($aR_0 < r$). Since the problem is statically determinate, the normalized radius R_0 of the elastoplastic interface is the only function of the stress boundary conditions p and p^0 and the yield parameters q and K_p (e.g., Salencon, 1969):

$$R_0 = \left[\frac{2}{K_p + 1} \frac{p^0 + \frac{q}{(K_p - 1)}}{p + \frac{q}{(K_p - 1)}} \right]^{1/(K_p - 1)} \quad (32)$$

Since R_0 is a monotonic function of p , it can be used as a kinematic parameter instead of p (at least beyond the elastic limit); in other words any mechanical field (such as stress, strain, displacement) can be viewed as a dual function of r and R_0 .

The stress field in the plane is independent of the flow rule of the material. In the cylindrical coordinates system (r, θ) the stresses are given by (e.g., Salencon, 1969):

Plastic

$$\left\{ \begin{array}{l} \tau_r = -P^0 + \frac{S_\ell^0}{K_p - 1} \left[K_p + 1 - 2 \left(\frac{r}{aR_0} \right)^{K_p - 1} \right] \\ \tau_\theta = -P^0 + \frac{S_\ell^0}{K_p - 1} \left[K_p + 1 - 2 K_p \left(\frac{r}{aR_0} \right)^{K_p - 1} \right]; \\ \tau_{r\theta} = 0 \end{array} \right. ; \quad a \leq r \leq aR_0 \quad (33)$$

Elastic

$$\left\{ \begin{array}{l} \tau_r = -P^0 + S_\ell^0 \left(\frac{r}{aR_0} \right)^{-2} \\ \tau_\theta = -P^0 - S_\ell^0 \left(\frac{r}{aR_0} \right)^{-2} \\ \tau_{r\theta} = 0 \end{array} \right. ; \quad r \geq aR_0 \quad (34)$$

in which the symbol S_ℓ^0 denotes the limiting value of the stress deviatoric at infinity:

$$S_\ell^0 = \frac{K_p - 1}{K_p + 1} \left(P^0 + \frac{q}{K_p - 1} \right) \quad (35)$$

Within the elastic region the induced displacement field is given by:

$$u = - \frac{aS_\ell^0}{2G} R_0 \left(\frac{r}{aR_0} \right)^{-1} \quad r \geq aR_0 \quad (36)$$

A-3 DISPLACEMENT IN THE PLASTIC REGION.

Within the plastic region ($a \leq r \leq aR_0$), the displacement cannot be described in simple form except for the case of constant dilatancy angle. Instead, it is necessary to solve numerically the differential equation that is developed in the following text.

Since R_0 is used as the kinematic parameter, the rate of change of a mechanical quantity is defined as its partial derivative with respect to R_0 . The velocity v is thus defined by:

$$v = \frac{\partial u}{\partial R_0} \quad (37)$$

and the strain rate $\dot{\epsilon}_r, \dot{\epsilon}_\theta$ by:

$$\dot{\epsilon}_r = \frac{\partial \epsilon_r}{\partial R_0}; \quad \dot{\epsilon}_\theta = \frac{\partial \epsilon_\theta}{\partial R_0} \quad (38)$$

The strain rates are also related to the velocity by:

$$\dot{\epsilon}_r = \frac{\partial v}{\partial r}; \quad \dot{\epsilon}_\theta = \frac{v}{r} \quad (39)$$

In the plastic region, the strain (and strain rate) consists of an elastic and a plastic part. The elastic part can be expressed in terms of the stress (and stress rate) by means of Hooke's law. The plastic part of the strain rate tensor is controlled by the flow rule

$$\dot{\epsilon}_r^p = -K_p^* \dot{\epsilon}_\theta^p \quad (40)$$

where the tangent dilatancy factor K_p^* can be an arbitrary function of the stress (generally the mean pressure) and the accumulated plastic shear strain, $\gamma = \epsilon_r^p - \epsilon_\theta^p$. The flow rule (equation 40) can then be rewritten in terms of the total and elastic strain rate:

$$\dot{\epsilon}_r + K_p^* \dot{\epsilon}_\theta = \dot{\epsilon}_r^e + K_p^* \dot{\epsilon}_\theta^e \quad (41)$$

The elastic strain rates $\dot{\epsilon}_r^e$, $\dot{\epsilon}_\theta^e$ in the plastic zone can be computed from Hooke's law and the partial derivative of τ_r and τ_θ , given by equation (33), with respect to R_0 . Specifically:

$$\dot{\epsilon}_r^e + K_p^* \dot{\epsilon}_\theta^e = \frac{S_\ell^0}{2G} \frac{\lambda_*}{R_0} \left(\frac{r}{aR_0} \right)^{K_p-1} \quad (42)$$

in which

$$\lambda_* = (K_p - 1) (K_p^* - 1) + (1 - 2\nu) (K_p + 1) (K_p^* + 1) \quad (43)$$

The differential equation for the velocity field in the plastic zone can then be deduced from equation (41) using equations (39) and (42),

$$\frac{\partial v}{\partial r} + K_p^* \frac{v}{r} = \frac{S_\ell^0}{2G} \frac{\lambda_*}{R_0} \left(\frac{r}{aR_0} \right)^{K_p-1} \quad a \leq r \leq aR_0 \quad (44)$$

The velocity field in the plastic zone can thus be calculated from equation (44) using as boundary condition, the value of velocity on the elastoplastic interface. This boundary value, which is obtained by differentiating equation (36) with respect to R_0 , and setting $r = aR_0$ is equal to

$$v = - 2 \frac{aS_\ell^0}{2G} \quad (45)$$

Once the velocity field has been calculated from equations (44) and (45), the displacement is obtained by integrating $v(r, R_0)$ with respect to R_0 . However, calculation of the displacement can be dramatically simplified by noting that the displacement field (like the stress and velocity) is actually only a function of the dimensionless ratio r/aR_0 . For the purpose of demonstration it is convenient to introduce the unit plane (ρ, θ) defined by the affine transformation

$$\rho = \frac{r}{aR_0} \quad (46)$$

In the unit plane, the circle $\rho = 1$ separates an internal plastic region from an external elastic region (see figure 28). Using the transformation (equation 46), the differential equation for the velocity field becomes:

$$\frac{\partial \tilde{v}}{\partial \rho} + K_p^* \frac{\tilde{v}}{\rho} = \lambda_* \rho^{K_p - 1} \quad \rho \leq 1 \quad (47)$$

in which \tilde{v} stands for the velocity normalized by the characteristic length L defined as:

$$L = \frac{aS_l^0}{2G} \quad (48)$$

Equation (47), subject to the boundary condition $\tilde{v} = -2$ at $\rho = 1$, demonstrates that \tilde{v} is indeed a function of only the cylindrical coordinate ρ of the unit plane. Hence, the general form of the displacement field is necessarily given by:

$$u(r, R_0) = R_0 L \tilde{u} \left(\frac{r}{aR_0} \right) \quad (49)$$

The differential equation (47) can now be expressed in terms of the normalized displacement \tilde{u} , using the fact that

$$\tilde{v}(\rho) = \tilde{u}(\rho) - \rho \tilde{u}'(\rho) \quad (50)$$

thus

$$\rho^2 \tilde{u}'' + K_p^* \rho \tilde{u}' - K_p^* \tilde{u} = -\lambda_* \rho^{K_p} \quad (51)$$

This differential equation is subject to the boundary conditions

$$\tilde{u}(1) = -1 \quad ; \quad \tilde{u}'(1) = 1 \quad (52)$$

which are deduced from the elastic solution (equation 36) for the displacement.

If the dilatancy factor K_p^* is assumed constant ($1 < K_p^* < K_p$), equation (51) is an Euler equation which can be solved in closed form to yield

$$\tilde{u}(\rho) = -\rho \left[1 + \frac{\lambda_* + 2K_p + 2K_p^*}{(K_p^* + 1)(K_p + K_p^*)} \left(\rho^{-(K_p^*+1)} - 1 \right) \right]$$

$$+ \frac{\lambda_*}{(K_p - 1)(K_p + K_p^*)} \left(\rho^{K_p - 1} - 1 \right) \quad (53)$$

Realistically, K_p^* should be a function of the accumulated plastic shear strain, and possibly of the mean pressure. In such circumstances, equation (51) must be solved numerically; this involves expressing K_p^* (and thus λ_*) as an explicit function of the radial coordinate ρ and the displacement \tilde{u} . Any dependence of K_p^* on the mean stress can be transformed into a function of ρ by means of equation (33), since the problem is statically determinate. The dependence of K_p^* on the plastic shear strain γ involves expressing γ in terms of ρ , \tilde{u} , and \tilde{u}' .

From equation (49) and the strain-displacement relations:

$$\varepsilon_r - \varepsilon_\theta = \frac{S_0^o}{2G} \left(\tilde{u}'(\rho) - \frac{\tilde{u}(\rho)}{\rho} \right) \quad (54)$$

The elastic components of the deviatoric strain in the plastic region are deduced from Hooke's law and equation (33):

$$\varepsilon_r^e - \varepsilon_\theta^e = \frac{S_0^o}{2G} 2\rho^{K_p - 1} \quad (55)$$

Hence

$$\gamma = \frac{S_0^o}{2G} \tilde{\gamma} \quad (56)$$

in which:

$$\tilde{\gamma} = \tilde{u}'(\rho) - \frac{\tilde{u}(\rho)}{\rho} - 2\rho^{K_p - 1} \quad (57)$$

It follows from equations (57) and (33) if K_p^* depends on the stress, that the differential equation (51) can be rewritten in the general form

$$\tilde{u}'' = F(\rho, \tilde{u}, \tilde{u}') \quad (58)$$

This equation can be solved readily using a numerical method, such as the fourth-order Runge-Kutta technique (Henrici, 1962), which is summarized in Attachment A-1. Applicable solvers are often contained within the math library of a scientific pocket calculator, thus making the solution of equation (58) straightforward even with limited computational resources.

A-4 APPLICATION.

As a simple application of the theory developed above, we investigate a material characterized by a tangent dilatancy factor K_p^* that decays from an initial value K_p according to an exponential function of the plastic shear strain γ :

$$K_p^* = 1 + (K_p - 1) \exp\left(-\frac{\gamma}{\gamma_*}\right) \quad (59)$$

The parameter γ_* can most usefully be related to the maximum inelastic volume increase Δ_* , by integrating the relation

$$\frac{d\Delta}{d\gamma} = \frac{K_p^* - 1}{K_p^* + 1} \quad (60)$$

to yield

$$\Delta_* = \gamma_* \ln \frac{K_p + 1}{2} \quad (61)$$

Equations (59) - (61) indicate that the normalized displacement field $\tilde{u}(\rho)$ only depends on three dimensionless parameters, K_p , ν , and $\tilde{\Delta}_*$, which is defined as

$$\tilde{\Delta}_* = \frac{2G}{S_0} \Delta_* \quad (62)$$

Experimental evidence indicates that the maximum inelastic volume increase is less than 5 percent; thus $\tilde{\Delta}_*$ should lie in the range 0-100.

A-5 CONCLUSIONS.

The preparation of this paper was prompted by the need to improve predictions of tunnel closure. The assumption of a constant dilatancy angle is believed to be unrealistic because the dilatation should be a function of the plastic strain (damage) and the confining stress. Accordingly, a variable dilatation model was sought. Here we have shown that (1) the differential equation for the tunnel closure can be derived in a rigorous manner for a plastic dilatation which is an arbitrary function of the stress and the plastic shear strain and (2) that by using the unit-plane transformation, the differential equation can be cast in a form which is well suited for numerical resolution.

* * * * *

Attachment 1: Solution of a second-order differential equation by the fourth-order Runge-Kutta Method.

Consider a second-order differential equation of the form $y'' = f(x, y, y')$, with initial values of x_0, y_0, y'_0 . The fourth-order Runge-Kutta method leads to a recursive algorithm for calculating the values of y_{i+1}, y'_{i+1} at $x_{i+1} = x_i + h$, from the known values of y_i, y'_i at x_i :

$$y'_{i+1} = y'_i + \frac{1}{6} (k_1 + 2k_2 + 2k_3 + k_4)$$

$$y_{i+1} = y_i + h [y'_i + \frac{1}{6} (k_1 + k_2 + k_3)]$$

where the coefficients $k_1, k_2, k_3,$ and k_4 are given by

$$k_1 = hf(x_i, y_i, y'_i)$$

$$k_2 = hf\left(x_i + \frac{h}{2}, y_i + \frac{h}{2} y'_i + \frac{h}{8} k_1, y'_i + \frac{k_1}{2}\right)$$

$$k_3 = hf \left(x_i + \frac{h}{2}, y_i + \frac{h}{2} y'_i + \frac{h}{8} k_1, y'_i + \frac{k_2}{2} \right)$$

$$k_4 = hf \left(x_i + h, y_i + hy'_i + \frac{h}{2} k_3, y'_i + k_3 \right)$$

where h is the integration step size.

APPENDIX B

DISPLACEMENT FIELD IN THE PLASTIC ZONE
CONSTANT DILATANCY ANGLE

B-1 INTRODUCTION.

This analysis of the closure of a tunnel in a cohesive, frictional, and dilatant medium, under nonhydrostatic loading, is based on the elastoplastic solution derived by Detournay (1983) (see also AA, 1983). In that model, the excavation of the tunnel is simulated by quasi-static unloading of a hole located in an infinite prestressed plane. The particular load path selected for that analysis was characterized by the fact that, beyond the elastic limit of the system, unloading of the hole corresponds to a decrease of an internal pressure p . Two successive stages could then be differentiated in the plastic response of the rock system: first, the development of two isolated plastic zones on either side of the hole, and, then, the formation of a unique yield region around the hole. For cases where the hole is completely surrounded by a plastic region and for cases where the problem is statically determinate, the equation of the interface is given in complex formulation by:

$$x + iy = aR_0 \hat{w}(\sigma) \quad (63)$$

where

$$\hat{w}(\sigma) = \lambda \sigma \left(1 + \frac{m}{\sigma^2} \right)^{2/(K_p+1)} ; \sigma = e^{i\theta} \quad (64)$$

$$\lambda = \left[F \left(-\delta; -\delta; 1; m^2 \right) \right]^{-1(K_p-1)} \quad (65)$$

(F is the Gaussian hypergeometric series)

$$\delta = \frac{K_p - 1}{K_p + 1} \quad (66)$$

$$R_o = \left[\frac{2}{K_p + 1} \frac{p^o + \frac{a}{K_p - 1}}{p + \frac{a}{K_p - 1}} \right]^{1/(K_p - 1)} \quad (67)$$

m = the obliquity of the stress at infinity

a = the tunnel radius

The equation (63) for interface was shown to be asymptotically correct for small departures from hydrostatic loading; nonetheless, it provides a good approximation of the interface, for cases where the solution is statically determinate.

In the original analysis, the tunnel closure was calculated by integrating the variation of the incremental displacement δu at the tunnel boundary with the loading parameter; the incremental displacement δu at the boundary being calculated by solving a system of hyperbolic partial differential equations governing δu in the plastic zone, using as a boundary condition the value of δu on the elastoplastic interface. The implementation of a variable dilatancy angle necessitates, however, that the governing differential equations in the plastic zone be expressed in terms of displacement instead of incremental displacement. As a first step toward implementing the complete mathematical model with variable dilatancy (of Appendix C), we describe in this appendix, the new model for the case of a constant dilatancy angle. After giving in Section B-2, the explicit expression of the elastic displacement along the elastoplastic interface, we detail in Section B-3 the derivation of the equations governing the displacement field u in the plastic zone and the numerical calculation of u by the method of characteristics.

B-2 ELASTIC DISPLACEMENT AT THE ELASTOPLASTIC INTERFACE.

The induced stresses $\underline{\sigma}^1$ in the infinite elastic region bounded by the elastoplastic interface can be expressed in terms of the complex potentials $\hat{\phi}_1(\zeta)$ and $\hat{\psi}_1(\zeta)$ of Muskhelishvili (1962) and the analytic function $\hat{w}(\zeta)$ which maps the region exterior to the unit circle in the parametric plane ζ onto the

elastic region in the unit plane $z' = z/aR_0$ (z is the complex variable $x + iy$ defined in the physical plane):

$$\tau_{xx}^1 + \tau_{yy}^1 = 2 S_\ell^0 \left[\hat{\phi}_1(\zeta) + \overline{\hat{\phi}_1(\zeta)} \right] \quad (68)$$

$$\tau_{yy}^1 - \tau_{xx}^1 + 2i \tau_{xy}^1 = 2 S_\ell^0 \left[\frac{\hat{w}(\zeta)}{\hat{w}'(\zeta)} \hat{\phi}_1'(\zeta) + \hat{\psi}_1(\zeta) \right] \quad (69)$$

Where S_ℓ^0 is the limiting value of the stress deviatoric S^0 at infinity, and a function of the mean pressure P^0 :

$$S_\ell^0 = \frac{K_p - 1}{K_p + 1} \left[P^0 + \frac{q}{K_p - 1} \right] \quad (70)$$

The induced displacement in the elastic region can also be expressed in terms of the complex potentials $\hat{\phi}_1(\zeta)$ and $\hat{\psi}_1(\zeta)$, and $\hat{w}(\zeta)$. For this particular elastoplastic problem, it can be shown that on the interface, the Cartesian components u_x , u_y of the elastic displacement are given by (Detournay, 1983):

$$(u_x + iu_y) = \frac{aR_0 S_\ell^0}{2G} \tilde{U} \quad (71)$$

where

$$\begin{aligned} \tilde{U} = & 4(1-\nu) \hat{w}(\sigma) \hat{\phi}_1(\sigma) - (3-4\nu) \hat{\chi}(\sigma) \\ & - \frac{\hat{w}(\sigma)}{\delta} + \frac{\hat{w}(\sigma)}{\delta} \hat{r}^{*K_p-1}(\sigma) - \overline{\hat{\psi}_1(\sigma)} \end{aligned}$$

$$\sigma = e^{i\theta}$$

$$\hat{\chi}(\sigma) = \int_{\infty}^{\sigma} \hat{w}(\xi) \hat{\phi}_1'(\xi) d\xi \quad (72)$$

$$\hat{\psi}_1(\sigma) = \int_{\infty}^{\sigma} \hat{w}'(\xi) \hat{\psi}_1(\xi) d\xi \quad (73)$$

$$\hat{f}_*^{K_p-1}(\sigma) = [\hat{w}(\sigma) \overline{\hat{w}(\sigma)}]^{(K_p-1)/2}$$

$$\delta = \frac{K_p - 1}{K_p + 1} \quad (74)$$

For the asymptotic solution of the elastoplastic interface, the Laurent series expression of the analytic functions $\hat{\chi}(\zeta)$, $\hat{\psi}_1(\zeta)$, $\hat{\phi}_1(\zeta)$ are:

$$\hat{\phi}_1(\zeta) = \sum_{j=1}^{\infty} \frac{a_{2j}}{\zeta^{2j}} ; a_{2j} = -\frac{m^j}{\delta} \binom{\delta}{j} \frac{F(-\delta; -\delta+j; j+1; m^2)}{F(-\delta; -\delta; 1; m^2)}$$

(75)

$$\hat{\chi}(\zeta) = \sum_{j=1}^{\infty} \frac{X_{2j-1}}{\zeta^{2j-1}} ;$$

with

$$X_{2j-1} = -\frac{m^j}{2^{j-1}} \frac{\lambda^K}{\delta} \sum_{k=0}^{j-1} 2^{(j-k)} \binom{1-\delta}{K} \binom{\delta}{j-k} F(-\delta; -\delta+j-k; j-k+1; m^2)$$

(76)

$$\hat{\psi}_1(\zeta) = \sum_{j=1}^{\infty} \frac{\beta_{2j-1}}{\zeta^{2j-1}} ; \beta_{2j-1} = \frac{g''_{2j} + h_{2j}}{2^{j-1}} + m\lambda m_{2j}$$

(77)

with

$$g''_{2j} = \lambda^K \frac{m^{j-1}}{\delta} \sum_{k=0}^{\infty} 2^{(j-1+k)} \binom{\delta}{j-1+k} \binom{1-\delta}{k} m^{2k} F(-\delta; -\delta+j+k-1; j+k; m^2)$$

(78)

$$h_{2j} = \lambda^K m^{j-1} \left[m^2 \binom{\delta-1}{j} + \left(1 + \frac{K_p-3}{K_p+1} m^2 \right) \binom{\delta-1}{j-1} + \frac{K_p-3}{K_p+1} \binom{\delta-1}{j-2} \right] \quad (79)$$

but

$$h_2 = \lambda^K \left[m^2 \binom{\delta-1}{1} + \left(1 + \frac{K_p-3}{K_p+1} m^2 \right) \right]$$

$$m_{2j} = m^j \binom{1-\sigma}{j} \quad (80)$$

Note that for an incompressible frictionless material, the displacement at the interface is given by

$$u_x + iu_y = \frac{aR_o S_l^o}{2G} \left[\frac{2m}{\sigma} - \left(\sigma + \frac{m}{\sigma} \right) \ln \left(\frac{1 + \frac{m}{\sigma^2}}{1 + m\sigma^2} \right) - (m^2 + 1) \sigma \right] \quad (81)$$

where

$$R_o = \exp \left(\frac{P^o - P}{2c} - \frac{1}{2} \right) \quad (82)$$

$$S_l^o = c \quad (c \text{ is the cohesion of the material}) \quad (83)$$

B-3 CALCULATION OF THE DISPLACEMENT FIELD IN THE PLASTIC ZONE.

B-3.1 Governing Partial Differential Equations for the Displacement.

B-3.1.1 Integration of the Flow Rule. The monotonic load path responsible for the propagation of the plastic zone around the tunnel ensures that there is no rotation of the principal stress directions in the plastic zone. Once the stresses at one point reach the yield surface (i.e., the point becomes plastic), from then on, the principal stress directions remain locked along

the radial and tangential directions. It thus follows that the principal directions of the incremental plastic strain tensor $\delta \underline{\varepsilon}^P$ are radial and tangential everywhere in the plastic zone and at any time during the monotonic loading. This feature of the problem allows us to integrate the incremental flow rule

$$\frac{\delta \varepsilon_r^P}{\delta \varepsilon_\phi^P} = - K_p^* \quad (84)$$

To obtain the following relation between the plastic strain increments in the radial and tangential directions:

$$\frac{\varepsilon_r^P}{\varepsilon_\phi^P} = - K_p^* \quad (85)$$

The integrated flow rule (equation 85) is actually equivalent to the following two equations which are expressed in terms of the Cartesian components of the plastic strain tensor $\underline{\varepsilon}^P$

$$\left(\varepsilon_x^P + \varepsilon_y^P \right) \cos 2\phi - \left(\varepsilon_x^P - \varepsilon_y^P \right) \sin \phi_* = 0 \quad (86)$$

$$2\varepsilon_{xy}^P \cos 2\phi - \left(\varepsilon_x^P - \varepsilon_y^P \right) \sin 2\phi = 0 \quad (87)$$

where

$$\sin \phi_* = \frac{K_p^* - 1}{K_p^* + 1} \quad (88)$$

In order to relate to the displacement, equations (86) and (87) are expressed in terms of the total strain, using the decomposition of the strain into a plastic and an elastic part:

$$\underline{\varepsilon} = \underline{\varepsilon}^e + \underline{\varepsilon}^P \quad (89)$$

Hence:

$$\begin{aligned} (\varepsilon_x + \varepsilon_y) \cos 2\phi - (\varepsilon_x - \varepsilon_y) \sin \phi_* \\ = \left(\varepsilon_x^e + \varepsilon_y^e \right) \cos 2\phi - \left(\varepsilon_x^e - \varepsilon_y^e \right) \sin \phi_* \end{aligned} \quad (90)$$

$$\begin{aligned}
2\varepsilon_{xy} \cos 2\phi - (\varepsilon_x - \varepsilon_y) \sin 2\phi \\
= 2\varepsilon_{xy}^e \cos 2\phi - (\varepsilon_x^e - \varepsilon_y^e) \sin 2\phi
\end{aligned}
\tag{91}$$

The strain components ε_x , ε_y , and ε_{xy} can be written as partial derivatives of the displacement components u_x and u_y . Before doing so, however, we derive an explicit expression for the elastic strain in the plastic zone.

B-3.1.2 Expressions for the Elastic Strains in the Plastic Zone. The elastic strain in the plastic zone can be derived explicitly as a function of the coordinates, using Hooke's law and the closed-form expression for the plastic stresses. Under the constraint

$$\varepsilon_z^e = 0 \tag{92}$$

which is assumed to hold, the elastic stress-strain relations in the plane (x,y) can be written as

$$\begin{aligned}
\varepsilon_x^e &= \frac{1}{2G} [(1 - \nu) \Delta\tau_x - \nu\Delta\tau_y] \\
\varepsilon_y^e &= \frac{1}{2G} [(1 - \nu) \Delta\tau_y - \nu\Delta\tau_x] \\
\varepsilon_{xy}^e &= \frac{1}{2G} \Delta\tau_{xy}
\end{aligned}
\tag{93}$$

Where $\Delta\tau$ denotes variation of the stress with respect to a reference state characterized by the uniform stress τ^0 . Thus

$$\begin{aligned}
\Delta\tau_x &= \tau_x + P^0 - S^0 \\
\Delta\tau_y &= \tau_y + P^0 + S^0 \\
\Delta\tau_{xy} &= \tau_{xy}
\end{aligned}
\tag{94}$$

Using equation (94), the plane stress-strain relations (equation 93) can be rewritten as

$$\begin{aligned}
\varepsilon_x^e + \varepsilon_y^e &= \frac{1-2\nu}{2G} (\tau_x + \tau_y) + \frac{1-2\nu}{2G} 2P^o \\
\varepsilon_x^e - \varepsilon_y^e &= \frac{1}{2G} (\tau_x - \tau_y) - \frac{2S^o}{2G} \\
\varepsilon_{xy}^e &= \frac{1}{2G} \tau_{xy}
\end{aligned} \tag{95}$$

In terms of the cylindrical coordinates (ρ, ϕ) of the unit-plane, the plastic stresses read:

$$\begin{aligned}
\tau_x + \tau_y &= \frac{2q}{K_p - 1} - 2 S_\ell^o \frac{K_p + 1}{K_p - 1} \rho^{K_p - 1} \\
\tau_x - \tau_y &= 2 S_\ell^o \cos 2\phi \rho^{K_p - 1} \\
\tau_{xy} &= S_\ell^o \sin 2\phi \rho^{K_p - 1}
\end{aligned} \tag{96}$$

Using equation (96), the expressions (95) for the elastic stresses in the plastic zone transform into

$$\begin{aligned}
\varepsilon_x^e + \varepsilon_y^e &= \left(\frac{S_\ell^o}{2G} \right) 2(1 - 2\nu) \frac{K_p + 1}{K_p - 1} \left(1 - \rho^{K_p - 1} \right) \\
\varepsilon_x^e - \varepsilon_y^e &= \frac{S_\ell^o}{2G} \left(2 \rho^{K_p - 1} \cos 2\phi - m \right) \\
\varepsilon_{xy}^e &= \left(\frac{S_\ell^o}{2G} \right) \rho^{K_p - 1} \sin 2\phi
\end{aligned} \tag{97}$$

where m is the obliquity defined as S^o/S_ℓ^o .

B-3.1.3 Normalized Partial Differential Equations. The strain components ε_x , ε_y , and ε_{xy} in equations (90) and (91) are now expressed as partial derivatives of the displacement components u_x and u_y . We will, however, operate the differentiation in the unit plane (x', y') instead of the physical plane (x, y) . Thus

$$\varepsilon_x = \frac{1}{aR_o} \frac{\partial u_x}{\partial x'} ; \quad \varepsilon_y = \frac{1}{aR_o} \frac{\partial u_y}{\partial y'} ; \quad 2\varepsilon_{xy} = \frac{1}{aR_o} \left(\frac{\partial u_x}{\partial y'} + \frac{\partial u_y}{\partial x'} \right) \tag{98}$$

since

$$x = aR_0 x'$$

$$y = aR_0 y'$$

Using equation (98) and the closed-form expressions (equation 97) for the elastic strain, equations (90) and (91) become:

$$\begin{aligned} \left(\frac{\partial u_x}{\partial x'} + \frac{\partial u_y}{\partial y'} \right) \cos 2\phi - \left(\frac{\partial u_x}{\partial x'} - \frac{\partial u_y}{\partial y'} \right) \sin 2\phi \\ = aR_0 \frac{S_\ell^0}{2G} H_1(\rho, \phi) \end{aligned}$$

$$\begin{aligned} \left(\frac{\partial u_x}{\partial y'} + \frac{\partial u_y}{\partial x'} \right) \cos 2\phi - \left(\frac{\partial u_x}{\partial x'} - \frac{\partial u_y}{\partial y'} \right) \sin 2\phi \\ = aR_0 \frac{S_\ell^0}{2G} H_2(\rho, \phi) \end{aligned} \quad (99)$$

where

$$\begin{aligned} H_1(\rho, \phi) = - \frac{2\lambda_*}{(K_p - 1)(K_p^* + 1)} \rho^{K_p - 1} \\ \cos 2\phi + 2(1 - 2\nu) \frac{K_p + 1}{K_p - 1} \cos 2\phi + 2m \frac{K_p^* - 1}{K_p^* + 1} \\ H_2(\rho, \phi) = 2m \sin 2\phi \end{aligned} \quad (100)$$

with

$$\lambda_* = (K_p - 1)(K_p^* - 1) + (1 - 2\nu)(K_p + 1)(K_p^* + 1) \quad (101)$$

The system of partial differential equations (99) and the expression (equation 71) for the displacement at the elasto-plastic interface (equation 71) represents the boundary conditions for the differential (equation 99), indicate that we can

define a normalized displacement $(\tilde{u}_x, \tilde{u}_y)$, which is the only function of the coordinates of the unit plane:

$$\underline{u} = aR_0 \frac{s_l^0}{2G} \underline{\tilde{u}} \quad (102)$$

The normalized displacement field $\underline{\tilde{u}}$ in the plastic zone is controlled by the three material parameters ν , K_p , K_p^* , and the stress obliquity m . Note that the consistent "normalized" strain field $\underline{\tilde{\epsilon}}$, which is defined as

$$\tilde{\epsilon}_{ij} = \frac{1}{2} \left(\frac{\partial \tilde{u}_i}{\partial x'_j} + \frac{\partial \tilde{u}_j}{\partial x'_i} \right) \quad (103)$$

is related to the physical strain field $\underline{\epsilon}$ by

$$\underline{\epsilon} = \frac{s_l^0}{2G} \underline{\tilde{\epsilon}} \quad (104)$$

We now have to calculate the normalized displacement components \tilde{u}_x, \tilde{u}_y in the plastic region of the unit plane, by solving the following set of partial differential equations:

$$\begin{aligned} \left(\frac{\partial \tilde{u}_x}{\partial x'} + \frac{\partial \tilde{u}_y}{\partial y'} \right) \cos 2\phi - \left(\frac{\partial \tilde{u}_x}{\partial x'} - \frac{\partial \tilde{u}_y}{\partial y'} \right) \sin 2\phi &= H_1(\rho, \phi) \\ \left(\frac{\partial \tilde{u}_x}{\partial y'} + \frac{\partial \tilde{u}_y}{\partial x'} \right) \cos 2\phi - \left(\frac{\partial \tilde{u}_x}{\partial x'} - \frac{\partial \tilde{u}_y}{\partial y'} \right) \sin 2\phi &= H_2(\rho, \phi) \end{aligned} \quad (105)$$

with the boundary conditions

$$\tilde{u}_x = \text{Re} [\tilde{U}^e] ; \quad \tilde{u}_y = \text{Im} [\tilde{U}^e] \quad (106)$$

along the curve Γ' , which is the image of the elastoplastic interface in the unit plane. As shown in the next section, the system of equations (105) is hyperbolic; it can therefore be solved by the method of characteristics.

B-3.2 Differential Equations along the Characteristics.

B-3.2.1 Normal Form. The partial differential equations (105), together with the expressions for the differentials $d\tilde{u}_x$ and $d\tilde{u}_y$ in terms of the partial derivatives i.e.,

$$\begin{aligned} d\tilde{u}_x &= \frac{\partial \tilde{u}_x}{\partial x'} dx' + \frac{\partial \tilde{u}_x}{\partial y'} dy' \\ d\tilde{u}_y &= \frac{\partial \tilde{u}_y}{\partial x'} dx' + \frac{\partial \tilde{u}_y}{\partial y'} dy' \end{aligned} \quad (107)$$

can be used to calculate the first partial derivatives of \tilde{u}_x and \tilde{u}_y at a point (x', y') at which the differentials $d\tilde{u}_x$ and $d\tilde{u}_y$ are known in a given direction dy'/dx' . Rewriting equations (105) and (107) as a system of four equations in the unknown first partial derivatives of \tilde{u}_x and \tilde{u}_y we obtain:

$$\begin{bmatrix} \cos 2\phi - \sin \phi^* & 0 & 0 & \cos 2\phi + \sin \phi^* \\ -\sin 2\phi & \cos 2\phi & \cos 2\phi & \sin 2\phi \\ dx' & 0 & dy' & 0 \\ 0 & dx' & 0 & dy' \end{bmatrix} \begin{Bmatrix} \frac{\partial \tilde{u}_x}{\partial x'} \\ \frac{\partial \tilde{u}_y}{\partial x'} \\ \frac{\partial \tilde{u}_x}{\partial y'} \\ \frac{\partial \tilde{u}_y}{\partial y'} \end{Bmatrix} = \begin{Bmatrix} H_1(\rho, \phi) \\ H_2(\rho, \phi) \\ d\tilde{u}_x \\ d\tilde{u}_y \end{Bmatrix} \quad (108)$$

If the system of equations (108) is hyperbolic, there exist two real characteristic directions dy'/dx' , for which the determinant D of the system (equation 108) vanishes. (Along the characteristics, the first derivatives of \tilde{u}_x and \tilde{u}_y cannot be determined from the differential $d\tilde{u}_x$ and $d\tilde{u}_y$.) The vanishing of the determinant D leads to the quadratic equation

$$\begin{aligned} (\cos 2\phi - \sin \phi^*) \left(\frac{dy}{dx}\right)^2 - 2 \sin 2\phi \left(\frac{dy}{dx}\right) \\ - (\cos 2\phi + \sin \phi^*) = 0 \end{aligned} \quad (109)$$

This quadratic equation has 2 real roots:

$$\frac{dy}{dx} = \tan (\phi \mp \varepsilon) \quad (110)$$

where

$$\varepsilon = \frac{\pi}{4} + \frac{\phi^*}{2} \quad (111)$$

(The upper sign refers to the α -, the lower to the β -characteristic, see figure 29). The system of equations (105) is therefore hyperbolic.

The differential equation along the characteristics are determined by specifying that one of the determinants D_j , obtained from D , by replacing its j th column by the column of the right members, is zero (requirement for a consistent solution). Taking, for example, D_3 (corresponding to $\partial \tilde{u}_x / \partial y'$):

$$D_3 = \begin{bmatrix} \cos 2\phi - \sin \phi^* & 0 & H_1(\rho, \phi) & \cos 2\phi + \sin \phi^* \\ -\sin 2\phi & \cos 2\phi & H_2(\rho, \phi) & \sin 2\phi \\ dx' & 0 & d\tilde{u}_x & 0 \\ 0 & dx' & d\tilde{u}_y & dy' \end{bmatrix} \quad (112)$$

or

$$\begin{aligned} D_3 = & H_1(\rho, \phi) dx' (\sin 2\phi dx - \cos 2\phi dy) \\ & - H_2(\rho, \phi) dx'^2 (\cos 2\phi + \sin \phi^*) \\ & + d\tilde{u}_x [-2 dx' \sin 2\phi \cos 2\phi \\ & + dy' \cos 2\phi (\cos 2\phi - \sin \phi^*)] \\ & + dx' d\tilde{u}_y \cos 2\phi (\cos 2\phi + \sin \phi^*) \end{aligned} \quad (113)$$

Imposing the vanishing of D_3 in the characteristics direction, yields for the α -characteristics:

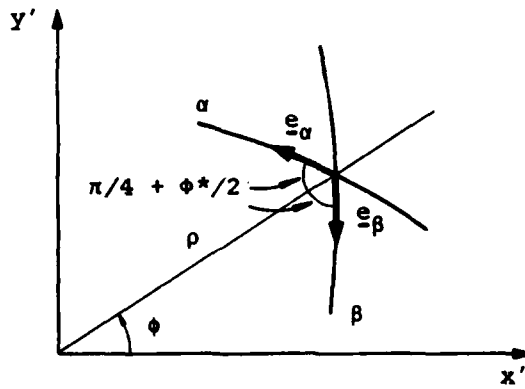


Figure 29. Displacement characteristics.

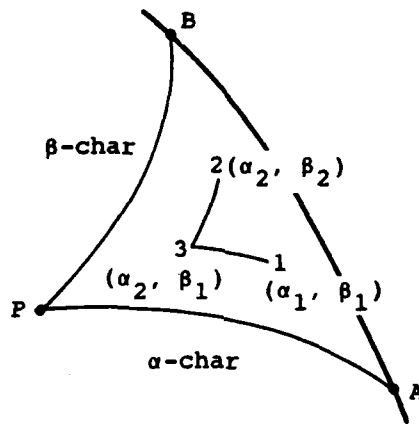
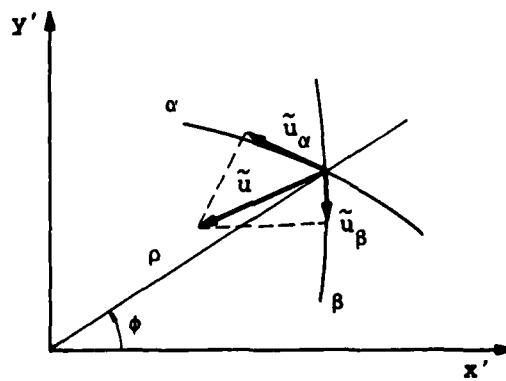


Figure 30. Method of characteristics.



AA923

Figure 31. Contravariant components of displacement.

$$\begin{aligned} d\tilde{u}_x + \tan(\phi - \varepsilon) d\tilde{u}_y &= dx' \frac{H_1(\rho, \phi)}{2 \cos^2(\phi - \varepsilon) \cos 2\phi} \\ &+ dx' H_2(\rho, \phi) \frac{\tan(\phi - \varepsilon)}{\cos 2\phi} \end{aligned} \quad (114)$$

for the β -characteristics:

$$\begin{aligned} d\tilde{u}_x + \tan(\phi + \varepsilon) d\tilde{u}_y &= dx' \frac{H_1(\rho, \phi)}{2 \cos^2(\phi + \varepsilon) \cos 2\phi} \\ &+ dx' H_2(\rho, \phi) \frac{\tan(\phi + \varepsilon)}{\cos 2\phi} \end{aligned} \quad (115)$$

The system of equations (114) and (115) represents the normal form of the system of partial differential equations (105); it gives the directional differential of \tilde{u}_x and \tilde{u}_y along the characteristics.

B-3.2.2 An Explicit Finite Difference Scheme. The normal form of the governing equations of the displacement field in the plastic zone lends itself naturally to an explicit finite difference scheme. If equations (114) and (115) are rewritten as

$$R_i d\tilde{u}_x + S_i d\tilde{u}_y = T_i dx' ; \quad i = 1, 2 \quad (116)$$

The finite difference discretization of equation (116) is then simply given by (see figure 30)

$$\begin{aligned} R_i (\tilde{u}_x^3 - \tilde{u}_x^i) + S_i (\tilde{u}_y^3 - \tilde{u}_y^i) \\ = T_i (x'_3 - x'_i); \quad i = 1, 2 \end{aligned} \quad (117)$$

The displacement $(\tilde{u}_x^3, \tilde{u}_y^3)$ at point 3 - whose coordinates (x'_3, y'_3) are computed by calculating the intersection point of the tangent to the characteristics at points 1 and 2 - is thus calculated by solving the linear systems of equations

$$\begin{bmatrix} R_1 & S_1 \\ R_2 & S_2 \end{bmatrix} \begin{bmatrix} \tilde{u}_x^3 \\ \tilde{u}_y^3 \end{bmatrix} = \begin{bmatrix} T_1(x'_3 - x'_1) + R_1 \tilde{u}_x^1 + S_1 \tilde{u}_y^1 \\ T_2(x'_3 - x'_2) + R_2 \tilde{u}_x^2 + S_2 \tilde{u}_y^2 \end{bmatrix} \quad (118)$$

where the coefficients R_i , S_i , T_i are evaluated at (x_i, y_i) .

Numerical tests, using an algorithm based on this scheme (Algorithm 392 of CACM) revealed poor accuracy of the solution (the test case was the hydrostatic problem), unless a high density characteristic mesh was used. The problem of accuracy was caused by (1) the curvature of the characteristics, which leads to an error in the evaluation of the intersection point of the two characteristics, and (2) the stiff nature of the differential equation. Because of this problem of accuracy, another scheme was implemented, that was based on expressing the components of the displacements in the curvilinear coordinate system of the characteristics.

B-3.2.3 The Characteristics Coordinates (α, β) . The displacement characteristics are logarithmic spirals, having the origin of the plane as an asymptotic point. The equation of the two characteristics intersecting at the point (ρ_0, ϕ_0) are given by

$$\rho = \rho_0 e^{\pm(\phi_0 - \phi) \tan(\pi/4 - \phi^*/2)} \quad (119)$$

(upper sign α -characteristics, lower sign β -characteristics).

It follows from equation (119), that the α - and β -characteristics can be identified as the coordinate-lines of a curvilinear coordinates system (α, β) . (Constant β and α coordinates, respectively) defined as:

$$\begin{aligned} \alpha &= - \sqrt{K_p^*} \ln \rho + \phi \\ \beta &= - \sqrt{K_p^*} \ln \rho - \phi \end{aligned} \quad (120)$$

The characteristic coordinates (α, β) have been defined in such a way that the base vectors \underline{e}_α and \underline{e}_β are pointing towards the asymptotic point (see figure 29). The contravariant components

\tilde{u}_α and \tilde{u}_β in the characteristic coordinate system (α, β) are given by (see figure 31).

$$\begin{aligned}\tilde{u}_\alpha &= -\cos(\phi - \varepsilon) \tilde{u}_x - \sin(\phi - \varepsilon) \tilde{u}_y \\ \tilde{u}_\beta &= -\cos(\phi + \varepsilon) \tilde{u}_x - \sin(\phi + \varepsilon) \tilde{u}_y\end{aligned}\quad (121)$$

B-3.2.4 Ordinary Differential Equations Along the Characteristics. The governing differential equations of the displacement field in the plastic zone can now be rewritten in terms of the contravariant components of the displacement. Inverting equation (121),

$$\begin{aligned}\cos \phi^* \tilde{u}_x &= -\sin(\phi + \varepsilon) \tilde{u}_\alpha + \sin(\phi - \varepsilon) \tilde{u}_\beta \\ \cos \phi^* \tilde{u}_y &= -\cos(\phi + \varepsilon) \tilde{u}_\alpha - \cos(\phi - \varepsilon) \tilde{u}_\beta\end{aligned}\quad (122)$$

and differentiating the above equations, we obtain

$$\begin{aligned}\cos \phi^* d\tilde{u}_x &= -\sin(\phi + \varepsilon) d\tilde{u}_\alpha - \cos(\phi + \varepsilon) \tilde{u}_\alpha d\phi \\ &\quad + \sin(\phi - \varepsilon) d\tilde{u}_\beta + \cos(\phi - \varepsilon) \tilde{u}_\beta d\phi \\ \cos \phi^* d\tilde{u}_y &= \cos(\phi + \varepsilon) d\tilde{u}_\alpha - \sin(\phi + \varepsilon) \tilde{u}_\alpha d\phi \\ &\quad + \cos(\phi - \varepsilon) d\tilde{u}_\beta + \sin(\phi - \varepsilon) \tilde{u}_\beta d\phi\end{aligned}\quad (123)$$

Substituting $d\tilde{u}_x$, and $d\tilde{u}_y$ as given by equation (123) in the differential equations (114) and (115), and expressing dx' as a function of $d\phi$ leads to:

$$\begin{aligned}d\tilde{u}_\alpha - (\tilde{u}_\alpha \tan \phi^* + \tilde{u}_\beta \sec \phi^*) d\phi &= \frac{\rho d\phi}{2 \sin \varepsilon \cos 2\phi} \\ &\quad \left[H_1(\rho, \phi) + 2 \sin(\phi - \varepsilon) \cos(\phi - \varepsilon) H_2(\rho, \phi) \right]\end{aligned}\quad (124)$$

AD-A166 101

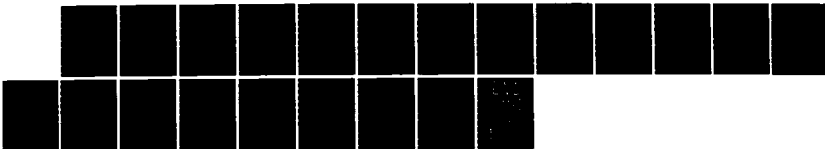
IMPROVED MODEL OF ROCK MASS DILATATION(U) ABBADIAN
ASSOCIATES EL SEGUNDO CA E DETOURNAY ET AL. 29 MAY 85
AA-R-8426-5882 DWA-TR-85-199 DWA001-84-C-0145

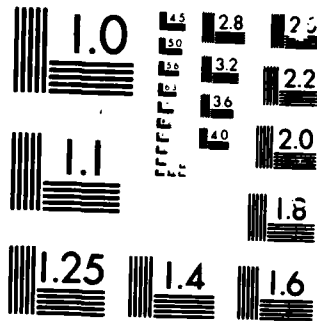
2/2

UNCLASSIFIED

F/G 8/7

NL





MICROCOPY RESOLUTION TEST CHART

$$d\tilde{u}_\beta + (\tilde{u}_\beta \tan \phi^* + \tilde{u}_\alpha \sec \phi^*) d\phi = - \frac{\rho d\phi}{2 \sin \varepsilon \cos 2\phi} [H_1(\rho, \phi) + 2 \sin(\phi + \varepsilon) \cos(\phi + \varepsilon) H_2(\rho, \phi)] \quad (125)$$

Since

$$dx' = - \frac{\cos(\phi - \varepsilon)}{\sin \varepsilon} \rho d\phi \quad \text{along } \alpha\text{-characteristics}$$

$$dx' = \frac{\cos(\phi + \varepsilon)}{\sin \varepsilon} \rho d\phi \quad \text{along } \beta\text{-characteristics}$$

and noting from equation (120) that

$$d\phi = \frac{d\alpha}{2} \quad \text{along } \beta = \text{constant}$$

$$d\phi = - \frac{d\beta}{2} \quad \text{along } \alpha = \text{constant}$$

the differential equations (124) and (125) can finally be rewritten as

$$2 \frac{d\tilde{u}_\alpha}{d\alpha} - (\tilde{u}_\alpha \tan \phi^* + \tilde{u}_\beta \sec \phi^*) = t_\alpha \quad (126)$$

$$2 \frac{d\tilde{u}_\beta}{d\beta} - (\tilde{u}_\beta \tan \phi^* + \tilde{u}_\alpha \sec \phi^*) = t_\beta \quad (127)$$

where, after simplification, t_α and t_β are given by

$$t_\alpha = \sin \varepsilon \rho \left[- \frac{\lambda_*}{(K_p - 1)(K_p^* + 1)} \rho^{K_p - 1} + (1 - 2\nu) \frac{K_p + 1}{K_p - 1} - m \cos 2(\phi - \varepsilon) \right] \quad (128)$$

$$t_\beta = \sin \varepsilon \rho \left[- \frac{\lambda_*}{(K_p - 1)(K_p^* + 1)} \rho^{K_p - 1} + (1 - 2\nu) \frac{K_p + 1}{K_p - 1} - m \cos 2(\phi + \varepsilon) \right] \quad (129)$$

The cylindrical coordinates (ρ, ϕ) in the above equations can simply be expressed in terms of α and β by

$$\phi = \frac{\alpha - \beta}{2} ; \quad (130)$$

$$\rho = \exp \left(- \frac{\alpha + \beta}{2 \sqrt{K_p^*}} \right) \quad (131)$$

B-3.3 Numerical Calculation of the Displacement Field in the Plastic Zone.

The numerical determination of the displacement field in the plastic zone is carried out by the method of characteristics (Masseau, 1899), which is based on the discretization of the differential equations (126) and (127).

Consider the point P, inside the plastic zone (see figure 30). The displacement at P is controlled by the values of the elastic displacement along the arc AB of Γ , which is intercepted by the two characteristics intersecting at P. (In other words, the domain of determinacy of the arc AB is the curvilinear triangle ABP bounded by the two characteristics α and β .) In the method of characteristics, the displacement at P is approximately solved by first defining N nodes along the noncharacteristic arc AB, then progressively computing the displacement at all the nodes of the characteristic mesh (located at the intersection of the characteristics emerging from the initial nodes), using a discretized form of the differential equations (126) and (127).

In the following, we derive the equations needed to calculate the displacement at any node (α_3, β_3) , assuming the displacements known at the two "parent" nodes (α_1, β_1) and (α_2, β_2) . ($\alpha_3 = \alpha_2$; $\beta_3 = \beta_1$.)

A class of numerical algorithms to calculate the displacement at the node (α_2, β_1) is based on the so-called ξ -method. The ξ -method relies on two assumptions:

1. The contravariant components $(\tilde{u}_\alpha, \tilde{u}_\beta)$ vary linearly with the characteristic coordinate between two adjacent nodes located on the same characteristics.

2. The differential equations (126) or (127) hold at a certain point " ξ " of the characteristic arc defined by two adjacent nodes.

For example, consider the point " ξ " of coordinates (α, β_1) located on the characteristic arc defined by the two end nodes (α_1, β_1) and (α_2, β_1) . The value of ξ , which must be in the range $(0,1)$ is given by

$$\xi = \frac{\alpha - \alpha_1}{\alpha_2 - \alpha_1} \quad (132)$$

The displacement at point ξ is given by

$$\begin{aligned} \tilde{u}_\alpha &= (1 - \xi) \tilde{u}_\alpha^1 + \xi \tilde{u}_\alpha^3 \\ \tilde{u}_\beta &= (1 - \xi) \tilde{u}_\beta^1 + \xi \tilde{u}_\alpha^3 \end{aligned} \quad (133)$$

On the basis of equation (133), the differential equation 126, which is assumed to hold at point " ξ ", becomes:

$$\begin{aligned} 2 \left[\tilde{u}_\alpha^3 - \tilde{u}_\alpha^1 \right] - (\alpha_2 - \alpha_1) \left\{ \tan \phi^* \left[\xi \tilde{u}_\alpha^3 + (1-\xi) \tilde{u}_\alpha^1 \right] \right. \\ \left. + \sec \phi^* \left[\xi \tilde{u}_\beta^3 + (1-\xi) \tilde{u}_\beta^1 \right] + \bar{t}_\alpha \right\} = 0 \end{aligned} \quad (134)$$

where \bar{t}_α is used to denote the value of t_α at point " ξ ". The discretization of equation 127 can be carried out in a similar way:

$$\begin{aligned} 2 \left[\tilde{u}_\beta^3 - \tilde{u}_\beta^2 \right] - (\beta_1 - \beta_2) \left\{ \tan \phi^* \left[\xi \tilde{u}_\alpha^3 + (1-\xi) \tilde{u}_\beta^2 \right] \right. \\ \left. + \sec \phi^* \left[\xi \tilde{u}_\alpha^3 + (1-\xi) \tilde{u}_\alpha^2 \right] + \bar{t}_\beta \right\} = 0 \end{aligned} \quad (135)$$

The above two equations can be written in matricial form as:

$$\begin{bmatrix} D_{\alpha\alpha} & D_{\alpha\beta} \\ D_{\beta\alpha} & D_{\beta\beta} \end{bmatrix} \begin{Bmatrix} \tilde{u}_\alpha^3 \\ \tilde{u}_\beta^3 \end{Bmatrix} = \begin{Bmatrix} P_\alpha \\ P_\beta \end{Bmatrix} \quad (136)$$

where

$$D_{\alpha\alpha} = 2/\Delta\alpha - \xi \tan \phi^*$$

$$D_{\alpha\beta} = -\xi \sec \phi^*$$

$$D_{\beta\alpha} = -\xi \sec \phi^*$$

$$D_{\beta\beta} = 2/\Delta\beta - \xi \tan \phi^*$$

$$P_{\alpha} = (D_{\alpha\alpha} + \tan \phi^*) \tilde{u}_{\alpha}^1 + (D_{\alpha\beta} + \sec \phi^*) \tilde{u}_{\beta}^1 + \bar{\tau}_{\alpha}$$

$$P_{\beta} = (D_{\beta\beta} + \tan \phi^*) \tilde{u}_{\beta}^2 + (D_{\beta\alpha} + \sec \phi^*) \tilde{u}_{\alpha}^2 + \bar{\tau}_{\beta}$$

with

$$\Delta\alpha = \alpha_2 - \alpha_1$$

$$\Delta\beta = \beta_1 - \beta_2$$

A class of algorithms can thus be generated depending on the value of ξ , from full explicit ($\xi = 0$) to fully implicit ($\xi = 1$). Some parametric investigations confirmed that the central-difference method ($\xi = 0.5$) provides the most accurate scheme.

For the central-difference method, the components (\tilde{u}_{α}^3 , \tilde{u}_{β}^3) of the displacement at node k are given explicitly by

$$\begin{aligned} \tilde{u}_{\alpha}^3 &= -\tilde{u}_{\alpha}^2 + \left(1 - \tan \phi^* \frac{\Delta\beta}{4}\right) \frac{D_{\alpha}}{D} + \sec \phi^* \frac{\Delta\alpha}{4} \frac{D_{\beta}}{D} \\ \tilde{u}_{\beta}^3 &= -\tilde{u}_{\beta}^1 + \left(1 - \tan \phi^* \frac{\Delta\alpha}{4}\right) \frac{D_{\beta}}{D} + \sec \phi^* \frac{\Delta\beta}{4} \frac{D_{\alpha}}{D} \end{aligned} \quad (137)$$

where

$$D_{\alpha} = \left(\tilde{u}_{\alpha}^1 + \tilde{u}_{\alpha}^2\right) + \tan \phi^* \frac{\Delta\alpha}{4} \left(\tilde{u}_{\alpha}^1 - \tilde{u}_{\alpha}^2\right) + \bar{\tau}_{\alpha} \frac{\Delta\alpha}{2}$$

$$D_{\beta} = \left(\tilde{u}_{\beta}^1 + \tilde{u}_{\beta}^2\right) + \tan \phi^* \frac{\Delta\beta}{4} \left(\tilde{u}_{\beta}^2 - \tilde{u}_{\beta}^1\right) + \bar{\tau}_{\beta} \frac{\Delta\beta}{2}$$

$$\begin{aligned} D &= \left(1 - \tan \phi^* \frac{\Delta\alpha}{4}\right) \left(1 - \tan \phi^* \frac{\Delta\beta}{4}\right) \\ &\quad - \frac{\Delta\alpha \Delta\beta}{16} (\sec^2 \phi^* - \tan^2 \phi^*) \end{aligned}$$

APPENDIX C

DISPLACEMENT FIELD IN THE PLASTIC ZONE-VARIABLE DILATANCY

C-1 INTRODUCTION.

In this appendix, we develop the theoretical basis of a numerical algorithm to calculate closure of a circular tunnel subject to a nonhydrostatic far-field stress, for a class of materials characterized by a variable dilatancy. The following analysis closely parallels the one outlined in Appendix B, for a material with a constant dilatancy.

C-2 VARIABLE DILATANCY FACTOR.

The dilatancy factor K_p^* , which is defined as

$$\frac{d\varepsilon_1^p}{d\varepsilon_3^p} = - K_p^* \quad (138)$$

is assumed to decay exponentially with the accumulated plastic shear strain γ , from an initial value K_p :

$$K_p^* = 1 + (K_p - 1) e^{-\gamma/\gamma_*} \quad (139)$$

The flow rule (equation 139) is associated at the elastic limit ($K_p^* = K_p$ if $\gamma = 0$); but as the material is yielding, the rate of increase of the inelastic dilatation Δ with γ progressively decreases so as to eventually vanish, when the maximum dilatation Δ_* is reached. The parameter γ_* in equation (139) can be related to Δ_* by integrating

$$\frac{d\Delta}{d\gamma} = \frac{K_p^* - 1}{K_p^* + 1} \quad (140)$$

to yield

$$\Delta_* = \gamma_* \ln \left(\frac{K_p + 1}{2} \right) \quad (141)$$

C-3 GOVERNING EQUATIONS.

C-3.1 Partial Differential Equations.

As for a constant dilatancy angle, the flow rule (equation 138) can be integrated, since there is no rotation of the principal direction of the incremental plastic strain tensor $\underline{\varepsilon}^p$ during loading; i.e.,

$$\frac{\varepsilon_r^p}{\varepsilon_\phi^p} = - \bar{K}_p^* (\gamma) \quad (142)$$

where \bar{K}_p^* is defined as the secant dilatancy factor. From \bar{K}_p^* , we can also define a "secant" dilatancy angle $\bar{\phi}_*$

$$\bar{\phi}_* = \arcsin \left(\frac{\bar{K}_p^* - 1}{\bar{K}_p^* + 1} \right) \quad (143)$$

Derivation of the differential equations governing the displacement field in the plastic zone follows step-by-step the approach detailed in Appendix B, except that all the constants depending upon the dilatancy angle ϕ_* must now be understood as functions of the (variable) secant dilatancy angle $\bar{\phi}_*$. In particular, the concept of the unit-plane still holds; in the unit-plane, the governing equation of the normalized plastic displacements \tilde{u} , which is defined as

$$\underline{u} = \frac{a s_0^0}{2G} R_0 \tilde{u} \quad (144)$$

are given by

$$\begin{aligned} \left(\frac{\partial \tilde{u}_x}{\partial x'} + \frac{\partial \tilde{u}_y}{\partial y'} \right) \cos 2\phi - \left(\frac{\partial \tilde{u}_x}{\partial x'} - \frac{\partial \tilde{u}_y}{\partial y'} \right) \sin \bar{\phi}_* &= H_1 (\rho, \phi) \\ \left(\frac{\partial \tilde{u}_y}{\partial y'} + \frac{\partial \tilde{u}_x}{\partial x'} \right) \cos 2\phi - \left(\frac{\partial \tilde{u}_x}{\partial x'} - \frac{\partial \tilde{u}_y}{\partial y'} \right) \sin 2\phi &= H_2 (\rho, \phi) \end{aligned} \quad (145)$$

where

$$\begin{aligned}
 H_1(\rho, \phi) = & - \frac{2\bar{\lambda}_*}{(K_p - 1)(\bar{K}_p^* + 1)} \rho^{K_p - 1} \cos 2\phi \\
 & + 2(1-2\nu) \frac{K_p + 1}{K_p - 1} \cos 2\phi + 2m \frac{\bar{K}_p^* - 1}{\bar{K}_p^* + 1} \\
 H_2(\rho, \phi) = & 2m \sin 2\phi
 \end{aligned} \tag{146}$$

with

$$\bar{\lambda}_* = (K_p - 1)(\bar{K}_p^* - 1) + (1 - 2\nu)(K_p + 1)(\bar{K}_p^* + 1) \tag{147}$$

Despite their similarity, an important difference exists between the two sets of equations (99) and (145). In the case of a constant dilatancy, the normalized displacement field \tilde{u} in the plastic domain of the unit-plane depends on the material parameters K_p , K_p^* , ν , and the stress obliquity m ; hence the same normalized displacement field holds for any shear elastic modulus and/or any stress at infinity characterized by the same obliquity m . In the case of a variable dilatancy angle, however, the governing equations for \tilde{u} depend on the ratio γ/Δ_* (by virtue of the law of variation of K_p^*) besides the parameters K_p , ν , m . Since

$$\gamma = \frac{S_\ell^0}{2G} \tilde{\gamma} \tag{148}$$

where

$$\tilde{\gamma} = \frac{\partial \tilde{u}}{\partial \rho} - \frac{\tilde{u}}{\rho} - \frac{1}{\rho} \frac{\partial \tilde{u}}{\partial \phi} - 2\rho^{K_p - 1} \tag{149}$$

the coefficients of the system of equation (145) are actually functions of the ratio $\tilde{\gamma}/\tilde{\Delta}_*$, where $\tilde{\Delta}_*$ is given by

$$\tilde{\Delta}_* = \frac{2G}{S_\ell^0} \Delta_* \tag{150}$$

Consequently, the normalized plastic displacement field \tilde{u} depends now on the dimensionless parameters m , K_p , ν , and $\tilde{\Delta}_*$. (The same conclusions would hold for other forms of variation of K_p^* .) Hence, some of the properties of the solution for a constant dilatancy angle (e.g., independence of \tilde{u} on S_2^0 , G) do not hold anymore.

C-3.2 Differential Equations along the Characteristics.

Derivation of the differential equations along the characteristics is identical to the procedure detailed in Section B-3 of Appendix B, but for the substitution of ϕ_* by $\bar{\phi}_*$. The normal form of the differential equations is

$$\begin{aligned} d\tilde{u}_x + \tan(\phi - \bar{\varepsilon}) d\tilde{u}_y &= dx \frac{H_1(\rho, \phi)}{2 \cos^2(\phi - \bar{\varepsilon}) \cos 2\phi} \\ &+ dx H_2(\rho, \phi) \frac{\tan(\phi - \bar{\varepsilon})}{\cos 2\phi} \\ &\text{along the } \alpha\text{-characteristics} \end{aligned} \quad (151)$$

$$\begin{aligned} d\tilde{u}_x + \tan(\phi + \bar{\varepsilon}) d\tilde{u}_y &= dx \frac{H_1(\rho, \phi)}{2 \cos^2(\phi + \bar{\varepsilon}) \cos 2\phi} \\ &+ dx H_2(\rho, \phi) \frac{\tan(\phi + \bar{\varepsilon})}{\cos 2\phi} \\ &\text{along the } \beta\text{-characteristics} \end{aligned}$$

and the characteristic directions are given by

$$\frac{dy}{dx} = \tan(\phi \mp \bar{\varepsilon}) \quad (152)$$

(upper sign for α -, lower sign for β -characteristics). In equations (151) and (152), the symbol $\bar{\varepsilon}$ denotes the inclination of the characteristics on the radial direction:

$$\bar{\varepsilon} = \frac{\pi}{4} + \frac{\bar{\phi}_*}{2} \quad (153)$$

Since the inclination $\bar{\varepsilon}$ is a function of the solution (i.e., the displacement \tilde{u}), it is not anymore possible to define explicitly the characteristic coordinates (α, β) . However, the formal form of the differential equations (126) and (127) still holds; i.e.,

$$2 \frac{d\tilde{u}_\alpha}{d\alpha} - (\tilde{u}_\alpha \tan \bar{\phi}_* + \tilde{u}_\beta \sec \bar{\phi}_*) = t_\alpha \quad (154a)$$

$$2 \frac{d\tilde{u}_\beta}{d\beta} - (\tilde{u}_\beta \tan \bar{\phi}_* + \tilde{u}_\alpha \sec \bar{\phi}_*) = t_\beta \quad (154b)$$

Provided that $d\alpha$ and $d\beta$ are defined by

$$d\alpha = \frac{d\rho}{\rho} - \frac{d\phi}{\sqrt{\bar{K}_p^*}} ; \quad d\beta = \frac{d\rho}{\rho} + \frac{d\phi}{\sqrt{\bar{K}_p^*}} \quad (155)$$

Indeed, the relationship between the increments $d\rho$ and $d\phi$ - characterizing the variation of the cylindrical coordinates between 2 points infinitesimally close on the same characteristics (see figure 32) - is given by $d\alpha = 0$ for the β -characteristic, and by $d\beta = 0$ for the α -characteristic. Note that in equations (154) the curvilinear components \tilde{u}_α and \tilde{u}_β are given in terms of \tilde{u}_x , \tilde{u}_y , by equation (121), with ε replaced by $\bar{\varepsilon}$, and the values of t_α and t_β are obtained from equations (128) and (129) respectively with ε , K_p^* , λ_* replaced by $\bar{\varepsilon}$, \bar{K}_p^* , $\bar{\lambda}_*$.

C-4 NUMERICAL SOLUTION OF THE DISPLACEMENT FIELD.

C-4.1 Preamble.

The system of differential equations (154) will be solved by the method of characteristics. A sequence of N nodes is selected along the elastoplastic interface, that defines a fan of characteristics in the plastic domain. The displacement at the initial nodes on Γ are calculated from the solution of the displacement field in the elastic domain, while the displacement at the nodes of the characteristic mesh is progressively computed by moving away from Γ , using the discretized form of the differential equations. These discretized equations will be derived for a class of methods (the ξ -method), which

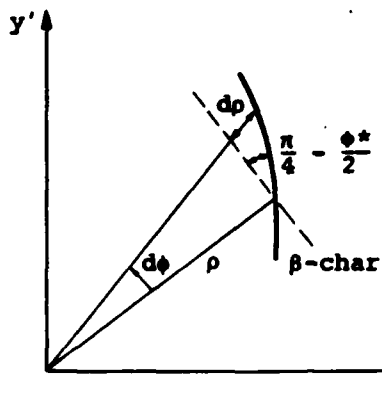


Figure 32. Geometrical relation between ρ , $d\rho$, and $d\phi$ for two points infinitesimally close on the same characteristic.

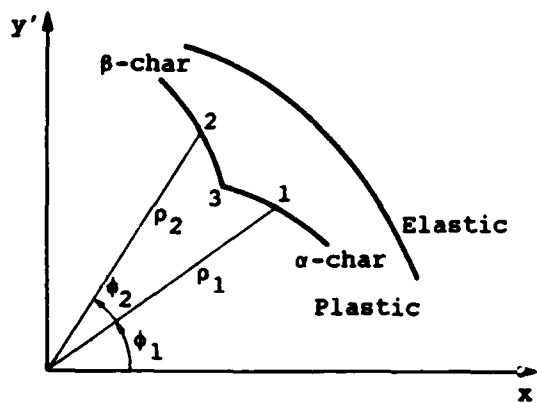
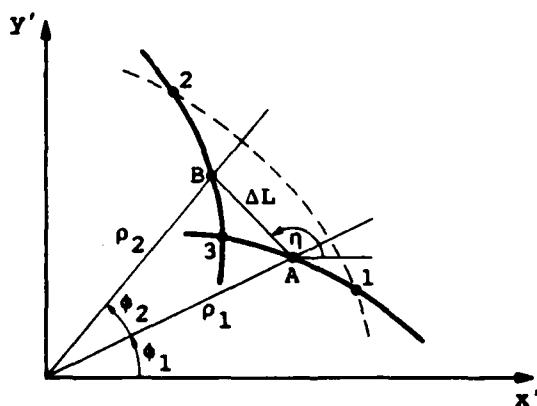


Figure 33. Calculation of displacement by the method of characteristics.



AA922

Figure 34. Calculation of average extension between A and B.

provides a full spectrum between fully explicit to fully implicit.

Several complications arise in the calculation of the plastic displacement field, that are introduced by the variable character of the material dilatancy. First, the position of the nodes of the characteristic mesh cannot, as previously, be calculated prior to the displacement of these nodes. Instead, they are an integral part of the solution and must be calculated concurrently to the displacement at the nodes. Second, the differential equations are nonlinear, and so are their discretized form (except for the fully explicit case). As a consequence, the calculation of the displacement at a new node, and the position of this node requires an iterative computational procedure. The following sections detail the basis of a numerical algorithm to calculate the displacement field in the plastic zone.

C-4.2 Discretized Equations.

Consider two close points 1 and 2 of the plastic zone, at which the displacement is known (see figure 33). Let ρ_i, ϕ_i denote the cylindrical coordinates of point i ($i = 1, 2$) and $\tilde{u}_\rho^i, \tilde{u}_\phi^i$ the cylindrical components of the known displacement at those points. For the sake of definiteness, it is assumed that $\phi_2 > \phi_1$. We need to calculate the coordinates (ρ_3, ϕ_3) of point 3, the intersection of the α -characteristic through point 1 and the β -characteristic through point 2, and the displacement $(\tilde{u}_\rho^3, \tilde{u}_\phi^3)$ at that point.

First introduce the characteristic "coordinates" α, β which are only valid on the two arc segments 13 and 23

on 13:

$$\begin{aligned} \alpha' &= - \sqrt{\left(\bar{K}_p^*\right)_\alpha} \ln \rho + \phi \\ \beta' &= - \sqrt{\left(\bar{K}_p^*\right)_\alpha} \ln \rho - \phi \end{aligned} \quad (156)$$

on 23:

$$\begin{aligned}\alpha'' &= -\sqrt{\left(\bar{K}_p^*\right)_\beta} \ln \rho + \phi \\ \beta'' &= -\sqrt{\left(\bar{K}_p^*\right)_\beta} \ln \rho - \phi\end{aligned}\quad (157)$$

where $\left(\bar{K}_p^*\right)_\alpha$ and $\left(\bar{K}_p^*\right)_\beta$ represent an "average" value of the secant dilatancy factor along segments 13 and 23, respectively (actually the value of \bar{K}_p^* at point " ξ ").

The characteristic "coordinates" (α'_1, β'_1) of point 1 are given by equation (156), with ρ and ϕ substituted by ρ_1 and ϕ_1 . Similarly, the "coordinates" (α''_2, β''_2) of point 2 are obtained from equation 157.

The segment of characteristic 13 is characterized by

$$\beta' = \beta'_1 \quad (158)$$

and 12 by

$$\alpha'' = \alpha''_2 \quad (159)$$

As for the case of a constant dilatancy angle, we can define the curvilinear components \tilde{u}_α and \tilde{u}_β of the displacement, which are related to the cylindrical components $\tilde{u}_\rho, \tilde{u}_\phi$ by

$$\begin{aligned}\tilde{u}_\alpha &= -\frac{1}{\sqrt{\bar{K}_p^* + 1}} \tilde{u}_\rho - \frac{\sqrt{\bar{K}_p^*}}{\sqrt{\bar{K}_p^* + 1}} \tilde{u}_\phi \\ \tilde{u}_\beta &= -\frac{1}{\sqrt{\bar{K}_p^* + 1}} \tilde{u}_\rho + \frac{\sqrt{\bar{K}_p^*}}{\sqrt{\bar{K}_p^* + 1}} \tilde{u}_\phi\end{aligned}\quad (160)$$

where \bar{K}_p^* is either $\left(\bar{K}_p^*\right)_\alpha$ or $\left(\bar{K}_p^*\right)_\beta$, depending on whether the point is on the 13 or 23 arc segments.

The numerical procedure to calculate $\rho_3, \phi_3, \tilde{u}_\rho^3, \tilde{u}_\phi^3$ relies on the following assumptions:

1. The curvilinear components \tilde{u}_α and \tilde{u}_β vary linearly with α' on the arc 13, and with β'' on the arc 23.

2. The differential equation (154a) applies at point "ξ" ($0 \leq \xi \leq 1$) of segment 13, with coordinates $(\xi \alpha'_1 + (1 - \xi) \alpha''_2, \beta'_1)$, and equation (154b) at the coordinates $(\alpha''_2, \xi \beta''_2 + (1 - \xi) \beta'_1)$ on the arc 23.
3. At point 3, $\alpha_3 = \alpha'_3 \cong \alpha''_3$ and $\beta_3 = \beta'_3 \cong \beta''_3$, which is only correct if $(\bar{K}_p^*)_\alpha$ and $(\bar{K}_p^*)_\beta$ correspond to the value of the secant dilatancy factor at point 3, and if u_α^3 (and u_β^3) is equal in both characteristic systems (α', β') and (α'', β'') .
4. The "average" secant dilatancy factor $(\bar{K}_p^*)_\alpha$ is equal to the value of \bar{K}_p^* at point "ξ" on segment 13; similarly $(\bar{K}_p^*)_\beta$ is the value of \bar{K}_p^* at point "ξ" on segment 23.

It follows from the assumptions that the discretized form of the two differential equations (154) are

$$\begin{aligned}
 & \left(\frac{2}{\Delta\alpha} - \xi \tan \bar{\phi}_\alpha^* \right) \tilde{u}_\alpha^3 - \xi \sec \bar{\phi}_\alpha^* \tilde{u}_\beta^3 \\
 & = \left(\frac{2}{\Delta\alpha} + (1 - \xi) \tan \bar{\phi}_\alpha^* \right) \tilde{u}_\alpha^1 + (1 - \xi) \sec \bar{\phi}_\alpha^* \tilde{u}_\beta^1 + \bar{t}_\alpha \\
 & - \xi \sec \bar{\phi}_\beta^* \tilde{u}_\alpha^3 + \left(\frac{2}{\Delta\beta} - \xi \tan \bar{\phi}_\beta^* \right) \tilde{u}_\beta^3 \\
 & = \left(\frac{2}{\Delta\beta} + (1 - \xi) \tan \bar{\phi}_\beta^* \right) \tilde{u}_\beta^2 + (1 - \xi) \sec \bar{\phi}_\beta^* \tilde{u}_\alpha^2 + \bar{t}_\beta
 \end{aligned} \tag{161}$$

where

\bar{t}_α and $\bar{t}_\beta = t_\alpha$ and t_β calculated at point "ξ" on segments 13 and 23, respectively

$\bar{\phi}_\alpha^*$ and $\bar{\phi}_\beta^* =$ the secant dilatancy angle at point "ξ" on segments 13 and 23, respectively

$$\Delta\alpha = \alpha''_2 - \alpha'_1$$

$$\Delta\beta = \beta'_1 - \beta'_2$$

the discretized equations (163) can be rewritten in matricial form:

$$\begin{bmatrix} D_{\alpha\alpha} & D_{\alpha\beta} \\ D_{\beta\alpha} & D_{\beta\beta} \end{bmatrix} \begin{Bmatrix} \tilde{u}_\alpha^3 \\ \tilde{u}_\beta^3 \end{Bmatrix} = \begin{Bmatrix} P_\alpha \\ P_\beta \end{Bmatrix} \quad (162)$$

with

$$D_{\alpha\alpha} = 2/\Delta\alpha - \xi \tan \bar{\phi}_\alpha^*$$

$$D_{\alpha\beta} = -\xi \sec \bar{\phi}_\alpha^*$$

$$D_{\beta\alpha} = -\xi \sec \bar{\phi}_\beta^*$$

$$D_{\beta\beta} = 2/\Delta\beta - \xi \tan \bar{\phi}_\beta^*$$

$$P_\alpha = (D_{\alpha\alpha} + \tan \bar{\phi}_\alpha^*) \tilde{u}_\alpha^1 + (D_{\alpha\beta} + \sec \bar{\phi}_\alpha^*) \tilde{u}_\beta^1 + \bar{t}_\alpha$$

$$P_\beta = (D_{\beta\beta} + \tan \bar{\phi}_\beta^*) \tilde{u}_\beta^2 + (D_{\beta\alpha} + \sec \bar{\phi}_\beta^*) \tilde{u}_\alpha^2 + \bar{t}_\beta$$

The components \tilde{u}_α^3 and \tilde{u}_β^3 of the displacement at point 3 are then given by

$$\begin{aligned} \tilde{u}_\alpha^3 &= \left(\frac{P_\alpha D_{\beta\beta} - P_\beta D_{\alpha\beta}}{D} \right) \\ \tilde{u}_\beta^3 &= \left(\frac{P_\beta D_{\alpha\alpha} - P_\alpha D_{\beta\alpha}}{D} \right) \end{aligned} \quad (163)$$

with

$$D = D_{\alpha\alpha} D_{\beta\beta} - D_{\alpha\beta} D_{\beta\alpha}$$

Finally, the cylindrical components $(\tilde{u}_\rho^3, \tilde{u}_\phi^3)$ of the displacement at point 3 read

$$\begin{aligned} \tilde{u}_r^3 &= -\frac{1}{4} \left(\sqrt{(\bar{K}_p^*)_\alpha + 1} + \sqrt{(\bar{K}_p^*)_\beta + 1} \right) (\tilde{u}_\alpha^3 + \tilde{u}_\beta^3) \\ u_\phi^3 &= \frac{1}{4} \frac{\sqrt{(\bar{K}_p^*)_\alpha + 1}}{\sqrt{(\bar{K}_p^*)_\alpha}} + \frac{\sqrt{(\bar{K}_p^*)_\beta + 1}}{\sqrt{(\bar{K}_p^*)_\beta}} \end{aligned} \quad (164)$$

while the position of point 3 is given by

$$\rho_3 = \exp \left(- \frac{\alpha_2 + \beta_1}{\sqrt{(\bar{K}_p^*)_\alpha} + \sqrt{(\bar{K}_p^*)_\beta}} \right)$$

$$\phi_3 = \frac{\sqrt{(\bar{K}_p^*)_\alpha} \alpha_2 + \sqrt{(\bar{K}_p^*)_\beta} \beta_1}{\sqrt{(\bar{K}_p^*)_\alpha} + \sqrt{(\bar{K}_p^*)_\beta}} \quad (165)$$

C-4.3 Iterative Procedure.

The quantities $(\bar{K}_p^*)_\alpha$ and $(\bar{K}_p^*)_\beta$, and the related constants which appear in the systems of equations (162), are not known beforehand since they are functions of the plastic shear distortion $\tilde{\gamma}$ at point " ξ ". An exception, however, is the fully explicit case for which point " ξ " on segments 13 and 23 corresponds to the known points 1 and 2, respectively. Thus, but for the case $\xi = 0$, the system of equations 162 is nonlinear and has to be solved iteratively. The iterative procedure consists of taking as a first approximation of $(\bar{K}_p^*)_\alpha$ and $(\bar{K}_p^*)_\beta$, the values of \bar{K}_p^* at 1 and 2, solving the systems of equations 162, calculating the positions and displacements of points " ξ " to determine new approximations for $(\bar{K}_p^*)_\alpha$ and $(\bar{K}_p^*)_\beta$, and iterating until satisfactory convergence is achieved.

C-4.4 Calculation of the Plastic Distortion $\tilde{\gamma}$.

The plastic distortion $\tilde{\gamma}$ can be calculated from the flow rule

$$\tilde{\Delta} = \sin \bar{\phi}^* \tilde{\gamma} \quad (166)$$

and the knowledge of the plastic normal strain $\tilde{\varepsilon}^P$ in a non-characteristic direction. Indeed, assume that $\tilde{\varepsilon}^P$ is known in a direction which is inclined by an angle η on the x-axis; thus

$$\tilde{\varepsilon}^P = \frac{1}{2} \left(\tilde{\varepsilon}_\rho^P + \tilde{\varepsilon}_\phi^P \right) + \frac{1}{2} \cos 2 (\eta - \phi) \tilde{\varepsilon}_\rho^P - \tilde{\varepsilon}_\phi^P \quad (167)$$

Using equations (166) and (167), we obtain for $\tilde{\gamma}$

$$\tilde{\gamma} = \frac{2 \tilde{\varepsilon}^p}{\sin \bar{\phi}^* + \cos 2(\eta - \phi)} \quad (168)$$

If η defines a characteristic direction, $\cos 2(\eta - \phi) = -\sin \phi^*$ and $\tilde{\gamma}$ is undefined from equation (168) (ε^p vanishes in the characteristic direction).

Let us now calculate the approximate normal strain ε between two adjacent points A and B at which the displacement is known (see figure 34). The angle η , which gives the inclination of the segment AB on the x-axis, and the distance ΔL between A and B are given by

$$\eta = \arctan \frac{y_B - y_A}{x_B - x_A} ;$$

$$\Delta L = \sqrt{(x_B - x_A)^2 + (y_B - y_A)^2} \quad (169)$$

Let u_{AB}^A denote the displacement at point A in the η -direction and u_{AB}^B the displacement at B, also in the η -direction. u_{AB}^A and u_{AB}^B are related to the cylindrical components of the displacement at A and B by

$$u_{AB} = \cos(\eta - \phi) u_\rho + \sin(\eta - \phi) u_\phi \quad (170)$$

The average extension $\bar{\varepsilon}$ between A and B is thus given by

$$\bar{\varepsilon} = \frac{u_{AB}^B - u_{AB}^A}{\Delta L} \quad (171)$$

The average strain $\bar{\varepsilon}$, represents an approximation of the normal strain ε in the η -direction at both points A and B.

The elastic part $\tilde{\varepsilon}^e$ of the normal strain in the direction η is given in terms of the Cartesian components of the elastic strain tensor by

$$\tilde{\varepsilon}^e = \frac{1}{2} \left(\tilde{\varepsilon}_x^e + \tilde{\varepsilon}_y^e \right) + \frac{1}{2} \left(\tilde{\varepsilon}_x^e - \tilde{\varepsilon}_y^e \right) \cos 2\alpha + \tilde{\varepsilon}_{xy}^e \sin 2\alpha \quad (172)$$

Since

$$\begin{aligned}\frac{1}{2} (\tilde{\varepsilon}_x^e + \tilde{\varepsilon}_y^e) &= (1 - 2\nu) \frac{K_p + 1}{K_p - 1} (1 - \rho^{K_p - 1}) \\ \frac{1}{2} (\tilde{\varepsilon}_x^e - \tilde{\varepsilon}_y^e) &= \rho^{K_p - 1} \cos 2\phi - m \\ \tilde{\varepsilon}_{xy}^e &= \rho^{K_p - 1} \sin 2\phi\end{aligned}\quad (173)$$

the expression for $\tilde{\varepsilon}^e$ becomes

$$\begin{aligned}\tilde{\varepsilon}^e &= (1 - 2\nu) \frac{K_p + 1}{K_p - 1} (1 - \rho^{K_p - 1}) \\ &\quad + \cos 2(\eta - \phi) \rho^{K_p - 1} - m \cos 2\eta\end{aligned}$$

The plastic part $\tilde{\varepsilon}^P$ is then determined by the difference $\tilde{\varepsilon} - \tilde{\varepsilon}^e$.

DISTRIBUTION LIST

DEPARTMENT OF DEFENSE

DEFENSE ADVANCED RSCH PROJ AGENCY
ATTN: DEFENSE SCIENCES OFFICE

DEFENSE INTELLIGENCE AGENCY
ATTN: RTS-2A (TECH LIB)
ATTN: RTS-2B

DEFENSE NUCLEAR AGENCY
4 CYS ATTN: SPSS
ATTN: STSP
4 CYS ATTN: STTI-CA

DEFENSE TECHNICAL INFORMATION CENTER
12 CYS ATTN: DD

FIELD COMMAND, DNA, DET 2
LAWRENCE LIVERMORE NATIONAL LABORATORY
ATTN: FC-1

FIELD COMMAND
ATTN: FCPR
ATTN: FCTO
ATTN: FCTT
ATTN: FCTT W SUMMA
ATTN: FCTXE

FIELD COMMAND TEST DIRECTORATE
ATTN: FCTBE/ L ASHBAUGH

DEPARTMENT OF THE ARMY

U S ARMY ENGR WATERWAYS EXPR STATION
ATTN: LIBRARY
ATTN: W MILLER
ATTN: WESSD J JACKSON
ATTN: WESS J BALSARA

DEPARTMENT OF THE AIR FORCE

AIR FORCE INSTITUTE OF TECHNOLOGY
ATTN: LIBRARY

AIR FORCE OFFICE OF SCIENTIFIC RSCH
ATTN: L HOKANSON

AIR FORCE WEAPONS LABORATORY, AFSC
ATTN: NTE M PLAMONDON
ATTN: SUL

BALLISTIC MISSILE OFFICE/DAA
ATTN: SYBU LT MICHAEL

DEPARTMENT OF ENERGY

UNIVERSITY OF CALIFORNIA
LAWRENCE LIVERMORE NATIONAL LAB
ATTN: L-122 S SACKETT
ATTN: L-658 TECH INFO DEPT. LIBRARY

LOS ALAMOS NATIONAL LABORATORY
ATTN: MS P364 REPORTS LIBRARY

SANDIA NATIONAL LABORATORIES
ATTN: LIBRARY & SECURITY CLASSIFICATION DIV.

SANDIA NATIONAL LABORATORIES
ATTN: TECH LIB 3141

OTHER GOVERNMENT

CENTRAL INTELLIGENCE AGENCY
ATTN: OSWR/NED

DEPARTMENT OF THE INTERIOR
ATTN: TECH LIB (UNCL ONLY)

DEPARTMENT OF DEFENSE CONTRACTORS

AGBABIAN ASSOCIATES, INC
ATTN: C BAGGE
2 CYS ATTN: C ST JOHN
ATTN: D VANDILLEN
2 CYS ATTN: E DETOURNAY
ATTN: M AGBABIAN

APPLIED RESEARCH ASSOCIATES, INC
ATTN: N HIGGINS

APPLIED RESEARCH ASSOCIATES, INC
ATTN: S BLOUIN

APPLIED RESEARCH ASSOCIATES, INC
ATTN: D PIEPENBURG

AVCO SYSTEMS DIVISION
ATTN: LIBRARY A830

BDM CORP
ATTN: F LEECH

BOEING CO
ATTN: AEROSPACE LIBRARY
ATTN: H LEISTNER
ATTN: M/S 42/37 K FRIDDELL
ATTN: T BERG

CALIFORNIA INSTITUTE OF TECHNOLOGY
ATTN: DANIELSON

CALIFORNIA RESEARCH & TECHNOLOGY, INC
ATTN: K KREYENHAGEN
ATTN: LIBRARY
ATTN: S SCHUSTER

CALIFORNIA RESEARCH & TECHNOLOGY, INC
ATTN: F SAUER

UNIVERSITY OF DENVER
ATTN: SEC OFFICER FOR J WISOTSKI

H & H CONSULTANTS, INC
ATTN: E CORDING
ATTN: J HALTIWANGER
ATTN: J HENDRON
ATTN: S PAUL

DEPARTMENT OF DEFENSE CONTRACTORS (CONTINUED)

FOSTER-MILLER INC

ATTN: WILLIAM A. RIBICH/VICE PRESIDENT

IIT RESEARCH INSTITUTE

ATTN: DOCUMENTS LIBRARY
ATTN: M JOHNSON

KAMAN TEMPO

ATTN: DASIAC

KAMAN TEMPO

ATTN: DASIAC

MERRITT CASES, INC

ATTN: D BURGESS
ATTN: J MERRITT

NEW MEXICO ENGINEERING RESEARCH INSTITUTE

ATTN: N BAUM

CITY COLLEGE OF NEW YORK

ATTN: C MILLER

PACIFIC-SIERRA RESEARCH CORP

ATTN: A LAUPA
ATTN: D WILSON
ATTN: H BRODE, CHAIRMAN SAGE

PACIFIC-SIERRA RESEARCH CORP

ATTN: D GORMLEY

R & D ASSOCIATES

ATTN: C KNOWLES
ATTN: J LEWIS
ATTN: P HAAS
ATTN: TECH INFO CTR

S-CUBED

ATTN: K PYATT
ATTN: LIBRARY
ATTN: R DUFF

SCIENCE APPLICATIONS INTL CORP

ATTN: H PRATT
ATTN: M MCKAY
ATTN: TECHNICAL LIBRARY

SCIENCE APPLICATIONS INTL CORP

ATTN: TECHNICAL LIBRARY

SOUTHWEST RESEARCH INSTITUTE

ATTN: A WENZEL

SRI INTERNATIONAL

ATTN: B HOLMES

STRUCTURAL MECHANICS ASSOC., INC

ATTN: R KENNEDY

TERRA TEK, INC

ATTN: S GREEN

TRW ELECTRONICS & DEFENSE SECTOR

ATTN: TECHNICAL INFORMATION CENTER

TRW ELECTRONICS & DEFENSE SECTOR

ATTN: B KELTNER
ATTN: D RANDELL
ATTN: E WONG, BLDG SB1
ATTN: L WOODRUFF
ATTN: O LEV
ATTN: P DAI
ATTN: R STCLAIR
ATTN: S RINDSKOPF

WEIDLINGER ASSOC, CONSULTING ENGRG

ATTN: I SANDLER
ATTN: M BARON

WEIDLINGER ASSOC, CONSULTING ENGRG

ATTN: J ISENBERG

END
FILMED

5-86

DTIC